CONSTRAINTS ON PHYSICAL AND OPTICAL PROPERTIES OF MARTIAN DUST AEROSOLS USING MER, PHOENIX, AND CURIOSITY OBSERVATIONS

A Dissertation

by

EMILY LEE MASON

Submitted to the Office of Graduate and Professional Studies of
Texas A&M University
in partial fulfillment of the requirements for the degree of

DOCTOR OF PHILOSOPHY

Chair of Committee,	Mark Lemmon
Co-Chair of Committee,	Istvan Szunyogh
Committee Members,	Anita Rapp
	Jennifer Marshall
Head of Department,	Ping Yang

August 2018

Major Subject: Atmospheric Sciences

ABSTRACT

The Martian atmosphere is dominated by the presence of irregularly shaped dust aerosols. These aerosols affect the vertical temperature profile and initiate dynamical responses on local, regional, and global scales. In order to quantify the effects of dust in dynamic and radiative transfer modeling, it is necessary to determine its physical and optical properties.

This dissertation focuses on physical property retrievals of dust pertaining to particle size and shape distribution. Sky brightness observations taken at the Phoenix landing site and the Mars Exploration Rovers (MER) Opportunity and Spirit locations can be modeled using select phase functions within a Discrete Ordinate Radiative Transfer code. Each phase function is dependent on the physical properties of dust, including effective size and variance of the distribution and shape.

Retrievals return values near 1.5 μm for particle size for Phoenix data sets using two different phase function models. This is consistent with previous work. Shape can be constrained using surveys with large scattering angle range. The particle sizes are consistent between models. The benefit of using an ellipsoidal shape is that the corresponding phase function model is physical, self-consistent, and available over a wider range of wavelengths. Fits to MER data return some variation in particle size, which is more evident at Opportunity sites than for Spirit sites. The methodology for retrieving particle size is unique and does not depend on the assumption of particle shape.

In addition to particle size information, we present a quicklook method for retrieving optical depth from the newest rover, Mars Science Laboratory (MSL) Curiosity, in Gale crater. This method shows promise in filling in the gaps for past optical depth observation as well as providing information for operational use.

DEDICATION

To my sister, my mom, my dad, and my husband. Thanks for the support.

ACKNOWLEDGMENTS

I would like to thank my advisor, Dr. Mark Lemmon, and my committee members, Dr. Istvan Szunyogh, Dr. Anita Rapp, and Dr. Jennifer Marshall, for providing me with information on atmospheric sciences and for being available to answer all of my questions. I would also like to express appreciation to my whole committee for helping me apply for career opportunities. I would like to thank the Texas A&M University Department of Atmospheric Sciences for accepting my application. I would like to additionally thank the staff and IT crew.

I would like to thank NASA for providing this grant and JPL for allowing me to participate in MSL operations. Specifically, I would like to thank my advisors and peers in the Martian community for their invaluable advice moving forward. I would like to thank my JPL advisor, Manuel de la Torre Juárez, for helping me advance my research skills. I would also like to thank Dr. Claire Newman and Dr. Mike Smith for both advising me in and helping me with my future endeavors.

To my family, thank you for supporting me during a very stressful time in my life. Your encouragement means the world. To my mom and dad, Richard and Penny Mason, thanks for keeping me positive while listening to me complain constantly. To my husband, thanks for stepping up on positive support while I navigated home and work life. Thanks to my peers for serving as points of information not available from faculty, staff, or advisors.

CONTRIBUTORS AND FUNDING SOURCES

Contributors

This work was supported by a dissertation committee consisting of Associate Professor Mark Lemmon, Professor Istvan Szunyogh, and Assistant Professor Anita Rapp of the Department of Atmospheric Sciences and Professor Jennifer Marshall of the Department of Physics and Astronomy.

The data analyzed for Chapters 3,4 and 5 were downloaded through the NASA Planetary Data System (PDS) (http://pds-geosciences.wustl.edu) and by Dr. Mark Lemmon.

All other work conducted for the dissertation was completed by the student independently.

Funding Sources

Graduate study was supported by a fellowship from Texas A&M University and a dissertation research fellowship from NASA Mars Data Analysis Program award NNX11AI88G. NASA Mars Exploration Program via sub-award from MSSS. Texas A&M University.

NOMENCLATURE

OGAPS	Office of Graduate and Professional Studies at Texas A&M University
B/CS	Bryan and College Station
TAMU	Texas A&M University
MER	Mars Exploration Rovers
DISORT	Discrete Ordinate Radiative Transfer
MSL	Mars Science Laboratory
REMS	Rover Environmental Monitoring Station
Mastcam	Mast Camera
NASA	National Aeronautics and Space Agency
ESA	European Space Agency
MEP	Mars Exploration Program
PSD	Particle Size Distribution
L_s	Areocentric longitude
IRIS	infrared interferometer spectrometer
EPF	Emission Phase Function
IRTM	Infrared Thermal Mapper
MGS	Mars Global Surveyor
TES	Thermal Emission Spectrometer
MERA	Mars Exploration Rover A (Spirit)
MERB	Mars Exploration Rover B (Opportunity)

Navcam	Navigational Camera
Pancam	Panoramic Camera
VIS	Visible wavelength
IR	Infrared wavelength
TOA	Top of atmosphere
MRO	Mars Reconnaissance Orbiter
SSI	Surface Stereo Imager
Mini-TES	Mini-Thermal Emission Spectrometer
MPFIT	IDL least-squares fitting algorithm
PDS	Planetary Data System
RTL	Telemetry data records
RNV	Environmental data records
Sol	One day on Mars beginning at the start of a mission
MY	Mars Year

TABLE OF CONTENTS

Page

LIST OF FIGURES

FIGURE Page

LIST OF TABLES

1. INTRODUCTION AND LITERATURE REVIEW

Several decades of missions through the National Aeronautics and Space Agency (NASA), European Space Agency (ESA), and other countries have created a large network of collaboration to examine and investigate the physical and historical conditions of Mars through observations of the surface and atmosphere. The goal of the Mars Exploration Program (MEP) defined by NASA is to "explore Mars and to provide a continuous flow of scientific information and discovery through a carefully selected series of robotic orbiters, landers and mobile laboratories interconnected by a high-bandwidth Mars/Earth communications network." This prominently includes the search for life, the study of past climates, and the study of current atmospheric conditions.

The work presented in this dissertation focuses broadly on the impact of Martian atmospheric dust aerosols. This encompasses retrievals of physical and optical properties for various locations, seasons, and years on Mars. The observations used in this study are limited to ground-based data collected at four locations through three missions, but are connected though a study of the dust itself. Dust aerosols are important due to their impact on the Martian atmosphere. In general, aerosols absorb and scatter incoming solar radiation, which redistributes energy within the atmosphere. This in turn drives atmospheric dynamics.

This section provides a brief introduction into past observations made on Mars and physical information about the planet. Dust and its effects on the atmosphere are discussed in context with observations. The bulk of this work tests phase function models, which describe the scattering pattern of light due to atmospheric constituents such as dust. Two models are presented in this work and tested for accuracy across 3 sites. Throughout this modeling, two particle size distributions (PSD) will be tested. In addition to this

phase function model, a simplified model for optical depth retrieval, which describes direct extinction of light as it enters the atmosphere of Mars, will be presented.

1.1 General information about Mars

Mars orbits 142 million miles away from the sun on average, or $\sim$ 1.5 AU, where AU is an astronomical unit defined as 1.0 at Earth distance. Its average speed is 14.5 miles per second, which is faster than that of Earth, but the differences between maximum and minimum speed of Mars are more extreme due to a greater eccentricity. Mars is a smaller planet, with a 3,390 km mean radius and gravitational pull only 0.375 of that experienced on Earth. The axial tilt of Mars is similar to Earth's tilt at 25°, but its orbit is much more ellipsoidal, which creates large changes in season due to its proximity to the sun at perihelion (closest approach to sun) compared to aphelion (farthest approach from sun). The position of Mars in its orbit around the sun, which is roughly 687 Earth days or almost 2 Earth years, is defined by solar longitude, L_s, shown in figure 1.1.

A day on Mars lasts 24 hours and 37 minutes in standard Earth time. Sols are defined as Martian days starting at the beginning of each mission. They are unique to each mission so that the MERB mission is operational past 5000 sols, while the Phoenix mission only lasted to 151 sols. The dusty season is during perihelion, and most of CO_2 is released from the larger southern pole. The aphelion cloud belt forms during southern winter and is a prominent atmospheric feature at low latitudes. The northern summer represents the non-dusty season, as the planet passes aphelion. During this time, however, frontal dust lifting occurs at the edge of the receding northern cap. Perihelion shows a high degree of interannual variability in atmospheric properties, whereas aphelion shows low interannual variability (Smith 2004) due to the large number of dust storms.

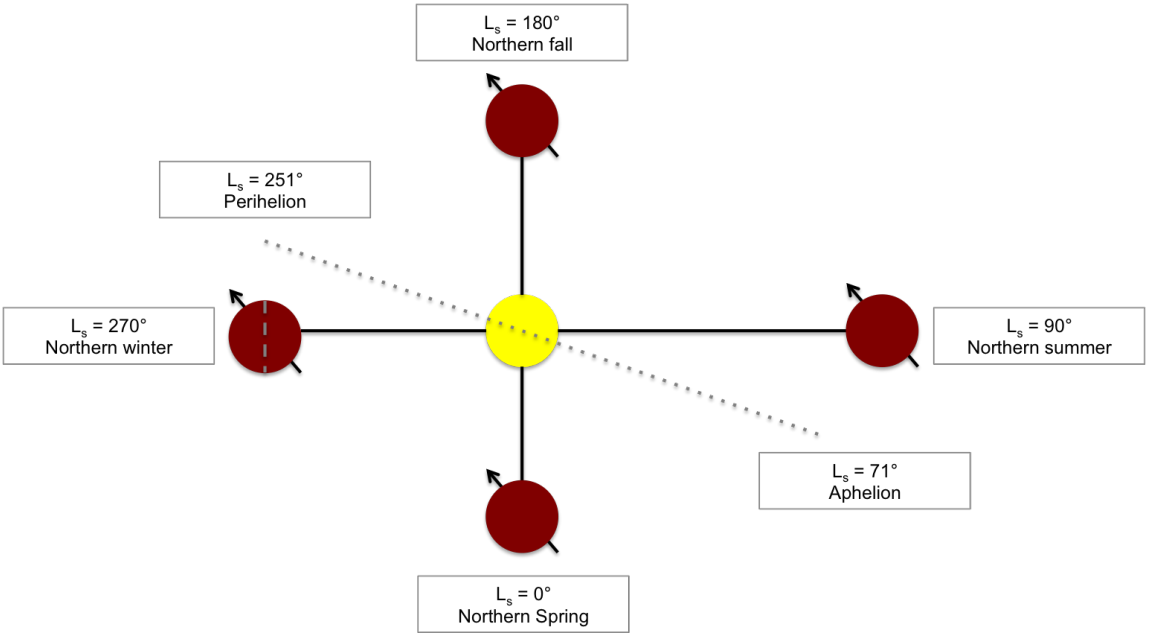

Figure 1.1: Full Martian orbit around sun; Northern summer is defined as $L_s = 90°$ and is marked by little atmospheric activity near aphelion; Northern winter is defined at $L_s = 270°$ and is marked by high atmospheric activity.

1.1.1 Surface and atmosphere

Mars, like Earth, is a terrestrial planet. The majority of the surface is igneous, and is generally covered in a layer of dust formed from mechanical weathering of the planet's surface. The atmosphere is 95% CO_2 with trace amounts of water vapor, CO, and methane. The temperature on average at the surface is $-81°$ F but can reach up to $86°$ F in some locations. Unlike Earth, Mars has a lower surface pressure, which is similar to that of Earth's stratosphere. This pressure changes up to 30% seasonally as the CO_2 and H_2O caps at either poles in turn sublimate and reform in summer and winter, respectively. Large, annual variations in pressure are dominated by this sublimation, where a minimum is reached just before equinox, $L_s = 180$, between northern summer and fall. A maximum in pressure occurs after perihelion, when the larger southern cap has sublimated.

The atmosphere undergoes considerable bombardment from solar winds due to lack of a protective planetary magnetosphere. Heating in the atmosphere is controlled by the surface, and the atmosphere does not retain much solar heat. It is an excellent absorber, and therefore also an excellent emitter. Thermal tides exist due to heating differences between day and night sides of planet. This tidal heating contributes to dynamic motions that are present in recorded pressure signals.

The globally averaged temperature can reach as high as 200 K (Smith 2008) during the day. Temperature is retrieved in 15 μm CO_2 band through orbital observations or from direct observations on the surface. The Thermal Emission Spectrometer (TES) provides up to three Mars Years (MY) of temperature profile records (Smith 2004). The atmosphere is cool and stable before dawn. Sunrise warms the surface quickly and creates steep, superadiabatic vertical temperature gradient through lowest 100m by mid morning.

1.1.2 Atmospheric dust aerosols

Gierasch & Goody (1971) showed through careful calculation the effects of dust aerosols by comparing the vertical temperature profile to profiles observed by Mariner 9. What they discovered was a better fit to a superadiabatic lapse rate. It is now well-known that dust not only absorbs and redistributes radiative energy but also plays a role in cloud formation and chemical reactions. Dust serves as cloud condensation nuclei helping to regulate transport of water between hemispheres (Fedorova et al. 2014) and alters the intrinsic signature of surface and middle atmospheric temperature through absorption (Wolff et al. 2010). Dust heats the atmosphere, creating a solar escalator that lifts more dust near the edge of the polar cap (Daerden et al. 2015). This is similar to dust on earth creating local hot spots and giving rise to gravity waves in upper atmospheric layers (Das et al. 2011).

The investigation of Martian dust centers on physical properties such as effective particle size and variance, which are both used to describe the particle size distribution, and

optical properties inherent to the type of dust of Mars. Earth dust is highly variable in space and time (e.g. Mahowald et al. 2014) and has significant impact on both climate and humans. Dust is the most abundant aerosol species in Earth's atmosphere by mass (Bangalath & Stenchikov 2015), and significantly influences energy balance of the climate through strengthening of local Hadley circulation and regional circulation features.

Dust aerosols are usually large and interact well with water vapor but are typically insoluble. They indirectly impact radiative forcing by acting as cloud condensation nuclei. Smaller particles dominate scattering in short wavelength while large particles dominate absorption at longer wavelengths. On Earth, the imaginary index of refraction for dust is indirectly linked to distribution because composition of a mixture of aerosols often depends on the aerosol population (Mahowald et al. 2014). On Mars, dust is generally uniform and is modeled using a wavelength dependent imaginary index only. Deposition of dust is an important factor that changes the distribution over time. Eddie mixing and boundary layer dynamics are efficient sources for smaller particles and sinks for larger particles (Toon et al. 1977). Tegan & Miller (1998) also notes that dust reflects and absorbs solar radiation and emits thermal radiation due to its large sizes of effective radii ($\sim 1 - 2\mu$m), causing cooling at surface levels with high optical depth.

1.2 Previous work on Mars dust

Optical depth has been collected through Viking landers (D.S. et al. 1988), Pathfinder (Smith & Lemmon 1999), MER (Lemmon et al. 2004), and Mini-TES (Smith et al. 2006). This provides over 5 years of record for total column extinction. With this record, many studies have focused on constraining particle size and variance using a variety of distributions. A number of missions dating back to the 1970's have investigated dust optical and physical properties. Since realization of the role that dust plays on Mars, characterization has been a prioritized goal in atmospheric studies. Early work is consistent in the returned

particle size, generally falling within a range of 1.5-2.0 μm (Smith 2008). More recent work has suggested a variation in particle size and distribution with height, latitude, and longitude. This is correlated with the variation in seasonal activity and several global dust storms (e.g. Wolff et al. 2006).

Toon et al. (1977) fit brightness temperature models to Mariner 9 infrared interferometer spectrometer (IRIS) to obtain dust size finding montmorillonite to be best and extracting properties from there. This work assumed a modified gamma distribution with γ = 0.5. Clancy & Lee (1991) analyzed Emission Phase Function (EPF) sequences from the Infrared Thermal Mapper (IRTM) onboard Viking Orbiter. This resulted in an effective particle sizes smaller than previously suggested ($r_{eff} = 2.5\mu m$), but noted that EPF sequences did not capture the forward scattering peak and were less sensitive to particle size. Along with this investigation, a constant single scattering albedo of 0.92 was found to produce good fits across wavelength. Clancy et al. (1995) used Viking data to model EPF sequences by assuming a palagonite dust composition. The resulting fits were R_{eff} = 1.2, v_{eff} = 0.4 for high dust loading events at the VL2 site and R_{eff} = 1.8, v_{eff} =0.8 for low dust loading events.

Using the Mars Global Surveyor (MGS) Thermal Emission Spectrometer (TES), Wolff & Clancy (2003) retrieved particle sizes consistent with an average R_{eff} = 1.6 - 1.8 μm. For an assumed value of v_{eff}, temporal and spatial variations were shown to exist within the model. Clancy & Wolff (2003) derived a smaller particle size in northern hemisphere using MGS TES EPF sequences during $L_s = 50 - 200^{\circ}$, consistent with smaller dust sizes 1.0 $\pm$ 0.2 and larger particles over southern hemisphere during global dust storm (2001) 1.8-2.5 μm. This work derived single scattering albedos of 0.92 - 094 overall, much lower than that of Wolff et al. (2006). Only small variation in R_{eff} were found during planet encircling dust storm and with mini-TES with season (Wolff et al. 2006). Wolff et al. (2010) shows variation of R_{eff} with season in MER sites.

Best-fit R_{eff} values of 1.85 $\pm$ 0.3 μm were found for low dust optical depth while for high dust loading, R_{eff} = 1.52 $\pm$ 0.3 μm. Eddy mixing was suggested as a possible removal mechanism within the boundary layer of universal dust. Tomasko et al. (1999) reported a mean weighted geometric cross section of 1.6 $\pm$ 0.15 μm with variance between 0.2 and 0.5, similar to values retrieved at the VIking Lander sites. The single scattering phase function was calculated using the parameterized model of Pollack & Cuzzi (1980) with an adjustment to the slope of the curve described in Showalter et al. (1992) but noted that comparisons of this phase function to laboratory measurements of different soil types showed little agreement to complex shapes or shapes with sharp edges.

More recent work for particle size distribution has come from two of the most successful ground missions on Mars. Both the Panoramic Cameras (Pancam) and Navigation Cameras (Navcam) onboard the Mars Exploration Rovers (MER) Spirit (MERA) and Opportunity (MERB) show consistent results despite variations in modeling structure. Particle sizes derived from Navcam fall within the range of 1.3-1.8 μm (Soderblom et al. 2008), but are derived using a spherical particle shape to model dust aerosols.

1.3 Intended progress for this dissertation

This work seeks to add to the general knowledge of Martian dust aerosol physical parameters as well as verify these physical parameters with past results. The information contained here is beneficial to the base of existing knowledge in that it provides comparison to scattering observations of the atmosphere from ground-based locations across the surface and tests both PSD and particle shape models.

This dissertation is organized to outline different models and site locations. Section 2 gives a brief introduction to some of the theory used in this work. Section 3 discusses a parameterized phase function model to describe how dust scatters light. This parameterized model is tested against observations taken at the Phoenix landing site. Section 4 provides

information on an updated model in an attempt to quantify dust aerosol shape. This work is also compared to observations at the Phoenix landing site, and shows the change in results from the parameterized phase function model. Section 5 applies both models to the Mars Exploration Rover (MER) pair of Spirit and Opportunity. Section 6 covers the work done to model optical depth at a fourth site on Mars. Finally, Section 7 provides a brief summary of the work presented in this dissertation.

2. RADIATIVE TRANSFER THEORY APPLIED TO THE MARTIAN ATMOSPHERE

This section presents the necessary background in Mars-focused radiative transfer theory to understand sections that follow. The focus of this research is scattering, but a review of both absorption and scattering will be presented in order to describe light interaction in the Martian atmosphere.

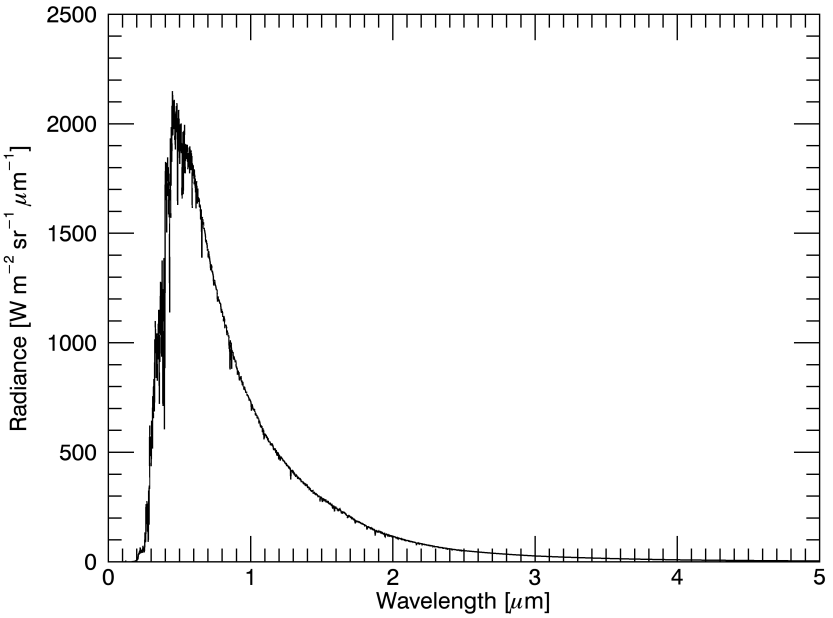

Figure 2.1: Spectral radiance of the sun.

In any planetary atmosphere, light undergoes either absorption and/or scattering to form the full extinction process, where scattering refers to the redirection of light from the direction of propagation. Light that is not absorbed or scattered is transmitted through the

atmospheric medium. The sun produces a radiance curve shown in 2.1 with peak radiance in the visible corresponding to an emitting temperature of 5800 K. For the purposes of this research, only visible (VIS) and near infrared (IR) wavelengths are considered. The solar spectrum in 2.1 does not account for variations in solar cycle or sunspot activity.

$$\tilde{n}(\lambda) = n_r + in_i \tag{2.1}$$

Absorption and scattering are dependent on the optical and physical properties of the particle. Optical properties in turn are dependent on both wavelength and the refractive index, which is comprised of a real and imaginary part and is given in equation 2.1. This is inherent on the particle's composition and can be determined through careful laboratory experiments or through retrievals. Both the real refractive index, n_r, and the imaginary refractive index, n_i, are wavelength dependent. Generally, n_r describes scattering, or more precisely the ratio of medium phase speed to that of a vacuum. Similarly, n_i is representative of absorption. The higher n_i the greater absorption of a medium or aerosol. Typically, for dominantly scattering regimes, even the slightest increase in n_i will produce a large change in extinction.

$$C_{ext} = C_{abs} + C_{sca} \tag{2.2}$$

Scattering and absorption for individual particles are represented through their scattering and absorption cross-sections, C_{sca} and C_{abs}, and the total extinction is the sum of both absorption and scattering (equation 2.2). The scattering (or absorption) cross section measures the efficiency of a particle to scatter (or absorb) when interacting with radiation. This quantity is wavelength dependent. The optical cross-section is related to the actual geometric cross-sections through extinction, scattering, and absorption efficiency shown in equation 2.3.

$$Q_{ext} = \frac{C_{ext}}{A_{proj}}, Q_{sca} = \frac{C_{sca}}{A_{proj}}, Q_{abs} = \frac{C_{abs}}{A_{proj}} \tag{2.3}$$

The single-scattering albedo, ω_0, is defined according to equation 2.4. It represents the probability of light being scattered once out of the direction of propagation. Whatever light is not scattered is either absorbed or transmitted based on the absorption efficiency.

$$\tilde{\omega}_0 = \frac{C_{sca}}{C_{ext}} = \frac{Q_{sca}}{Q_{ext}} \tag{2.4}$$

2.1 Particle size distribution

The particle size distribution (PSD) for dust describes the distribution of sizes in the atmosphere at any particular time. This is represented in equation 2.5 for any general distribution, n(r). For a homogenous or well-mixed aerosol type, this function is independent of wavelength and affects the optical depth as well as the relative strengths of absorption and scattering. Small particles tend to absorb proportionally with volume, whereas larger particles tend to scatter proportionally with particle surface area. The particle size distribution is unique to the time and location of observations taken, and so it can be used to view the progression of dust aerosol loading spatially and temporally.

$$n(r) = \frac{dN}{dr} = \frac{dN}{rdlog(r)} \tag{2.5}$$

A common distribution used in Martian calculations is that described by Hansen & Travis (1974) is shown in equation 2.6. This is known as the standard gamma distribution. In the equation, N_0 represents the number of particles in the distribution, a is the effective radius, or r_{eff}, and b is the effective variance, v_{eff}. Multiple notations are used across radiative transfer fields, but for the purposes of this work, a and b will be used to describe r_{eff} and v_{eff}, respectively.

$$n(r) = N_0 r^{(1-3b)/b} e^{-r/ab} \tag{2.6}$$

On Earth, multiple forms of distributions are used across varying fields. Dust in itself is often described with different distributions because the sources and composition vary in time and location. Mars is dissimilar to Earth in that its surface has long been weathered so that the same dust exists across the entire planet. Besides the standard gamma distribution, the bimodal size distribution given in equation 2.10 will be tested. Multiple equations are referenced from Hansen & Travis (1974) and described in depth by Petty & Huang (2011). The lognormal distribution is related to the effective size and variance through equations 2.8 and 2.9. These equations relate effective particle size to the distribution mean and variance. In addition the bimodal size distribution (equation 2.10) assumes that half the particles are in each domain. We allow for fitting of both particle size domains, a_1 and a_2. All four distributions are shown in 2.2.

$$n(r) = \frac{1}{(2\pi)^{1/2}\sigma_g}\frac{1}{r} exp[\frac{-(lnr - lnr_g)^2}{(2\sigma_g^2)}] \tag{2.7}$$

$$r_g = \frac{r_{eff}}{(1 + v_{eff})^{5/2}} \tag{2.8}$$

$$\sigma_g^2 = ln(1 + v_{eff}) \tag{2.9}$$

$$n(r) = \frac{1}{2}\frac{r^{(1-3b)/b} e^{-r/a_1 b}}{(a_1 b)^{(1-2b)/b}\Gamma[(1-2b)/b]} + \frac{1}{2}\frac{r^{(1-3b)/b} e^{-r/a_2 b}}{(a_2 b)^{(1-2b)/b}\Gamma[(1-2b)/b]} \tag{2.10}$$

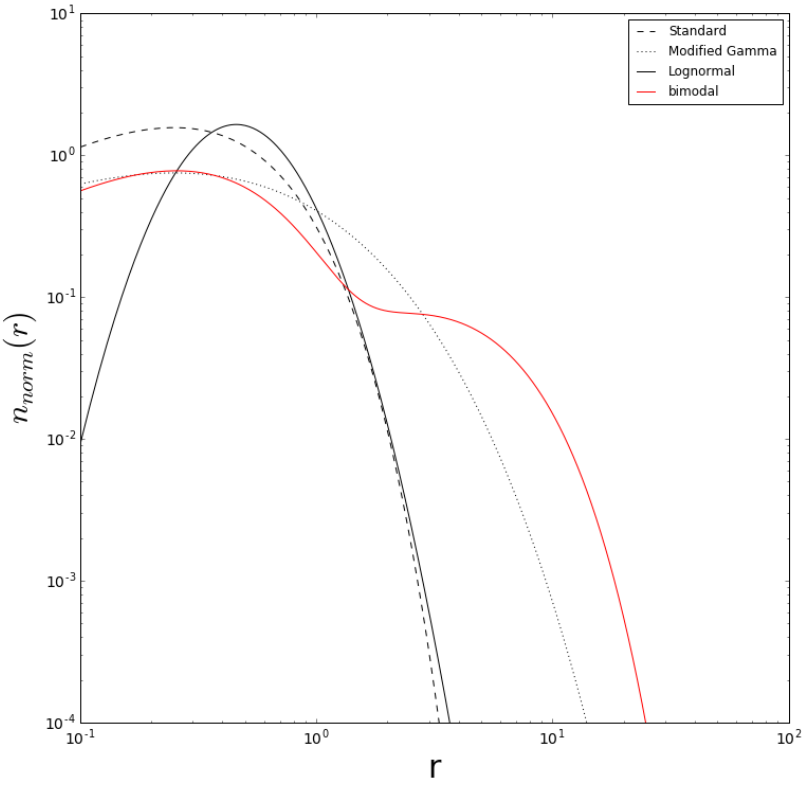

Figure 2.2: Plot of four distributions used in this study.

2.2 Volumetric phase function

Light that is scattered within an atmosphere has a preferential direction, which is defined using a 4x4 scattering matrix. The first element in the scattering matrix, P_{11}, represents the single scattering phase function. $P(\theta)$ describes the angular scattering pattern of an infinitesimal volume and albedo is fraction of incident beam which is scattered by volume. The remainder is absorbed or transmitted. This describes the probability of light being scattered in a particular direction. Backward scattering is defined as a change of direction of 180° from the direction of propagation. Forward scattering is defined as no

change in direction (0°). For an ensemble of particles, scattering is determined by the volumetric phase function. The volumetric phase function is a weighted phase function calculated using the particle size distribution, known particle shape, and composition. The properties of interest for Martian dust are particle size distribution, the refractive indices, and single scattering albedo. Once determined, these properties can be used to formulate the single scattering phase function, which determines how radiance is distributed in the atmosphere. Optical properties are wavelength dependent and therefore must be determined over a range of wavelengths. Scattering by dust dominates extinction for visible wavelengths in the Martian atmosphere, and determination of the single scattering phase function is a limiting factor for modeling this extinction. Calculation of the volumetric phase function is done using equations 2.11 through 2.15, where $\langle b_{ext}(\lambda)\rangle_j$ represents the PSD-weighted volumetric extinction cross section for the j^{th} shape. This is calculated using the extinction cross section, C_{ext}. Similarly, the volumetric scattering cross section is calculated using the scattering cross section, C_{sca}, which is dependent on shape, size, and wavelength. Using the volumetric scattering cross section and assumed shape distribution, the weighted single scattering phase function, $\langle P_{total}(\theta,\lambda)\rangle$, can be calculated using equations 2.13 through 2.15.

$$\langle b_{ext}(\lambda)\rangle_j = \int_0^\infty C_{ext}(\lambda, r)n(r)dr \tag{2.11}$$

$$\langle b_{sca}(\lambda)\rangle_j = \int_0^\infty C_{sca}(\lambda, r)n(r)dr \tag{2.12}$$

$$\langle P(\theta,\lambda)\rangle_j = \frac{\int_0^\infty p(\lambda,\theta,r)C_{sca}(\lambda,r)n(r)dr}{\langle b_{ext}(\lambda)\rangle} \tag{2.13}$$

$$\langle b_{total} \rangle = \sum \langle b_{sca}(\lambda) \rangle_j w_j \tag{2.14}$$

$$\langle P_{total}(\theta, \lambda) \rangle = \frac{\sum \langle P(\theta, \lambda) \rangle_j \langle b_{sca}(\lambda) \rangle_j w_j}{\langle b_{total} \rangle} \tag{2.15}$$

An ensemble of shapes is calculated by assuming that each particle shape exists in a distribution of sizes. Often shapes are parameterized by axis ratios. For cylinders, this is the length of the particle to the diameter of its cross section. For ellipsoids, parameterization of shape is done so using three axes, with two axis ratios.

2.3 DISORT

Radiative transfer is performed using a general Fortran-based Discrete Ordinate Radiative Transfer code (Stamnes et al. 1988, 2000), or DISORT, which computes the transfer of monochromatic, unpolarized radiation in a scattering, absorbing and emitting plane-parallel medium. This model accounts for atmospheric absorption, scattering, thermal emission, and bidiretional reflection and emission at a lower boundary. The algorithm is based on the equation describing atmospheric radiative transfer (equation 2.16), where S_λ is the source function. Sources of radiation include thermal emission and multiple scattering.

$$\mu \frac{dI_\lambda(\tau_\lambda, \mu, \phi)}{d\tau} = I_\lambda(\tau_\lambda, \mu, \phi) - S_\lambda(\tau_\lambda, \mu, \phi) \tag{2.16}$$

DISORT calculates multiple scattering and absorption for any number of discretized atmospheric layers specified by the user. Each layer is homogenous in properties. For example in a seven-layer model, the user specifies seven different τ and $P(\theta)$. For each layer, the user specifies τ, T, ω_0, and $P(\theta)$. The program returns I/F, for the user-specified angles and the provided incidence angle, where I/F represents observed brightness to brightness

of a perfectly reflecting Lambert surface illuminated at Mars distance, i.e. top of atmosphere (TOA) irradiance (Hapke 1981, Pollack et al. 1995).

Within the program, the phase function of each layer is first reconstructed from a user-input phase function using Legendre polynomials. Spherical harmonics is applied to create normalized assoicated legendre polynomials and to factor out azimuth dependence. LTE thermal emission is isotropic and scattering volumes behave isotropically so they cannot create any azimuth dependence. Intensity is expanded in a fourier cosine series to remove phi-dependence. This creates 2M independent integro-differential equations, each expanded using cosine functions calculated from Legendre polynomials one for each azimuthal intensity component.

For this work, thermal emission is negligible within the working wavelength range. Though Planck emission is an option, it was not necessary for scattering in the VIS and NIR wavelengths. Only a single layer was used for the purpose of this study. In this case, ground-based observations are insensitive to vertical distribution, and a single aerosol layer can be assumed. The atmospheric medium is forced by parallel beam at the upper boundary, and strong forward scattering is treated by δ - M method (Wiscombe 1977). In this case, we provide to DISORT the single scattering phase function, ω_0, incidence angle, lower boundary condition, and optical depth of the layer.

2.4 Least-squares minimization

The fitting algorithm used to find the best fit parameters for modeling is MPFIT (Markwardt 2009), a robust IDL program based on the Levenburg-Marquardt inversion method. This method is exact for a function that is linear in the parameters, convergence of the fit is then relatively insensitive to starting values that are linear. Non-linear values require sufficiently appropriate initial guesses, thus trial and error are important for this fit.

$$err_i = \frac{ln(y_i) - ln(F(x_i))}{\sigma_i} \tag{2.17}$$

Fitting the data seeks to minimize the natural log sum of deviation of some model, $F(x_i)$, to some data, y_i (equation 2.17). As a measure of the 'goodness of the fit', the best fit parameters returned through MPFIT are those that minimize the sum of weighted squared residuals of the model and the data. Thus, the parameters are measured for quality relative to the returned chi-square value, χ^2 (equation 2.18). This value is dependent on the weights of each datum, σ_i, which is an estimate of measurement uncertainty. We select the use of the reduced chi-square value, which is χ^2 divided by the degrees of freedom (DOF). This gives the error relative to the number of data points within an observation or model. This term is theoretically $\chi^2_v = 1$ for a perfect fit, but can be increased due to unidentified random and systematic errors in the data. We also employ the use of the reduced mean square error, RMSE in equation 2.20, which is a measure of how well the model fits the data. This must also be minimized, and represents a percentages of deviation. RMSE in combination with the reduced chi-square value provide a quantitative measure of the quality of fit.

$$\chi^2 = \sum (\frac{1}{\sigma_i^2}[y_i - y(x_i)]^2 \tag{2.18}$$

$$\chi^2_v = \frac{\sum err_i^2}{DOF} \tag{2.19}$$

$$RMSE = \sqrt{E(y_i - F(x_i))} \tag{2.20}$$

With non-linear fitting, propagation of error within the model is complex. It is therefore useful to estimate parameter uncertainty using the returned values from MPFIT's covari-

ance matrix. These values are highly dependent on the weighting uncertainty, however, and so it is important to perform error analysis to test the robustness of parameters.

$$F = \frac{\frac{\chi_c^2 - \chi_s^2}{DOF_c - DOF_s}}{\frac{\chi_c^2}{DOF_c}} \tag{2.21}$$

There is no way to know the true uncertainty of any data set. For measurements on Mars and for observational data presented in this dissertation, each data set contains uncertainties from random atmospheric fluctuations, instrument noise, and systematic errors. In addition, models can deviate from what is the true physical relationship, and so there is error introduced in both modeling and fitting.

To estimate this error for Phoenix and MER datasets, we employ the addition of random noise to each dataset, perform another fit to the data, and record the returned results. Variations in these results serve as an error estimate for parameters. As a secondary check, we also simulate datasets using our model to provide an estimate of standard deviation of the results. This standard deviation is then used to weight the actual model itself. With each section, we assess the potential errors in the model and data, citing references for previous work. We compare two models using the f-test standard given in equation 2.21. F$\sim$1 represents little improvement between simplified and complex models, and F>1 represents an improvement using a more complex model (denoted by subscript c in equation 2.21).

3. PARTICLE SIZE DISTRIBUTION AT THE PHOENIX LANDER SITE

The Phoenix Lander descended to the Martian surface on May 25, 2008 at 68.22°N, 234.25°E in Green Valley of Vastitas Borealis during the northern hemispheric spring season (L_s = 76°). The total length of the mission extended 151 sols, which surpassed the nominal 90-sol mission goal and provided data into late northern summer and early northern fall. During that time, the cap was active with frontal dust storms, ice clouds, and dust devils.

Atmospheric measurements are available throughout the mission and characterize the northern latitude region and polar cap. Total column extinction, shown in figure 3.1 for the Phoenix mission (Lemmon 2010), represents of both scattering and absorption of light by the atmosphere as well as atmospheric activity. In figure 3.1, optical depth is high at the beginning of the mission, decreases through sol 80, and increases in variability towards the end of the mission. High optical depths at the beginning of the mission are consistent with frontal dust lifting (Wang & Fisher 2009) caused by recession of the polar cap edge during northern spring. Frontal dust storms contribute to high optical depth towards the beginning of the mission and end of the mission, while ice is a dominate factor in later sols. Ice clouds are visible in some images, but the frequency of occurrence is low. Any observations with visible clouds are not included in this analysis.

Radiative transfer modeling for the Martian atmosphere requires knowledge of dust particle size distribution and refractive indices as well as optical depth and surface albedo as described in section 3. In particular, the selection of particle size distribution has an impact on multiple scattering, which is an important factor in radiative transfer modeling and in sky survey observations. Earth distributions vary from location to location (e.g. Sokolik et al. 2001). Distribution selection is also dictated by the type of aerosol, including

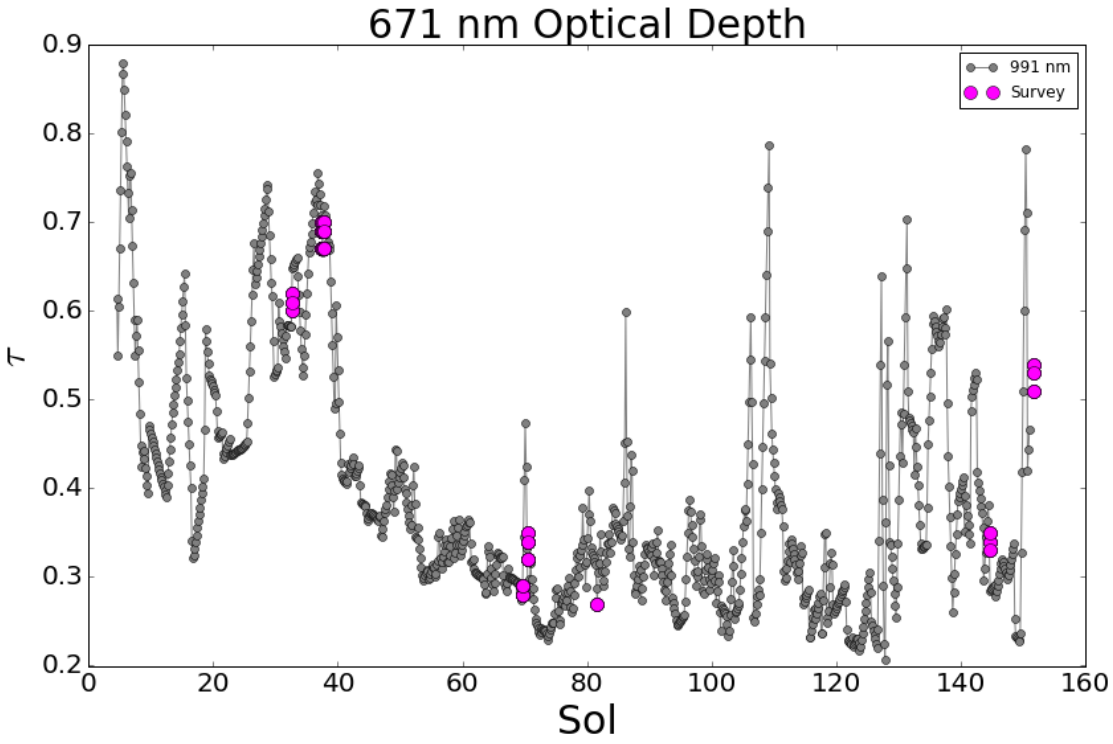

Figure 3.1: Total column extinction derived from direct solar imaging using the 671 nm filter for the entire Phoenix mission

desert sand, fine dust, or even ash. The ratio of visible optical depth to infrared optical depth dictates the ability of dust to cool/warm atmosphere and depends primarily on size distribution which in turn is governed by lifting and transport (Montmessin et al. 2004).

The use of particle size distribution is nonuniform across scientific work. In fact a wide range of models are used to retrieve atmospheric properties including different uses of vertical distribution, particle shape, and phase matrix. The dust on Mars is highly uniform (e.g. Lemmon et al. 2004), which does not necessarily require the use of more than one distribution. Hansen & Travis (1974) show that radiative transfer models can be insensitive to the distribution used. Essentially, multiple distributions could produce the same results, and therefore the distribution itself does not need to be unique.

Martian dust modelers have used the gamma distribution presented in Hansen & Travis (1974). Its ease and simplicity make it easily comparable across modeling studies. That being said, the choice of this distribution is somewhat arbitrary in most cases (e.g. Smith 2008). In that sense, it is worth testing several distributions within our own model to determine the sensitivity to different distributions and how they affect the retrievals of particle size and variance. Specifically, the use of bimodal distributions is used to explain small particle haze (e.g. Fedorova et al. 2014, Taylor et al. 2007). Taylor et al. (2007) uses the gamma distribution presented in Hansen & Travis (1974) to model dust distributions in the boundary layer of Mars, showing that smaller particles are rapidly mixed while larger particles greater than 10μm are concentrated near the ground.

This work focuses on applying an empirical phase function model within a DISORT radiative transfer algorithm to fit observations taken at the Phoenix landing site. These observations, along with a priori knowledge of optical depth, imaginary index of refraction, and ground reflectance, constrain particle size and variance in this region. In addition, it tests the assumption of insensitivity to size distribution by fitting both the gamma and bimodal distributions.

3.1 Data

The Surface Stereo Imager (SSI) onboard Phoenix houses 24 filters on two cameras and is capable of observing in 13 unique wavelengths (table 3.1). The instrument is part of the mast assembly and sits 2m off the ground. The images used in this study are taken as a sky survey sequence, which consists of 4 to 7 images of the sky taken at varying elevation and azimuthal angle with respect to the sun. Figure 3.3 shows an azimuthal and vertical scan from left to right. Dark current, bias, and standard calibrations were applied accordingly (Bell III et al. 2003). These calibrated images are available for download on the NASA PDS imaging node.

Left Eye	λ_{eff} [nm]	FWHM [nm]	Comment	Right Eye	λ_{eff} [nm]	FWHM [nm]	Comment
1	672.9	19.0	Red Stereo	1	672.9	19	Red Stereo
2	446.6	23.0	Blue Stereo	2	446.7	22.9	Blue Stereo
3	450.8	4.1	Solar/dust	3	671.1	4.9	Solar/dust
4	990.7	4.9	Solar/dust+water	1	935.5	5.2	Solar/water
5	887.0	5.8	Solar/dust+water	2	935.7	5.2	Solar/water
6	833.3	28.4	Surface	3	449.6	28.7	Diopter–Blue
7	801.5	21.6	Surface	1	753.1	20.1	Diopter–Infrared
8	864.3	36.8	Surface	2	753.5	20.6	Surface
9	899.5	44.8	Surface	3	603.8	16.9	Polarization
A	930.7	24.7	Surface	1	532.0	14.8	Surface–Red
B	1002.0	27.5	Surface	2	446.7	28.1	Surface–Green
C	968.5	29.7	Surface	3	485.3	20.8	Surface–Blue

Table 3.1: Filter values for SSI with descriptions, table credit: TAMU

Scattering surveys are used to retrieve I/F quantities for a given sol, where I/F is the ratio of radiometrically calibrated intensity to irradiance of a perfectly reflecting Lambertian surface (Pollack et al. 1995). In this case, F represents the flux at the top of the atmosphere (TOA) adjusted for Mars distance from the sun and divided by π. The images are taken near local noon to reduce the effects of multiple scattering and within a span of 15 to 40 minutes to reduce atmospheric variation. The returned images from telemetry are 256 x 256 pixel snapshots of the sky.

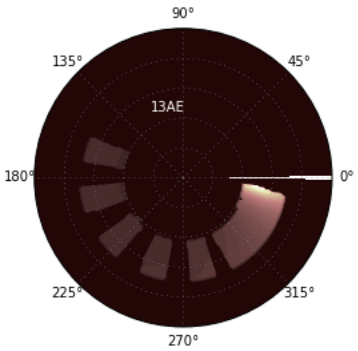

Figure 3.2: Example of survey 13AE post processing with transformation to local level coordinates and I/F

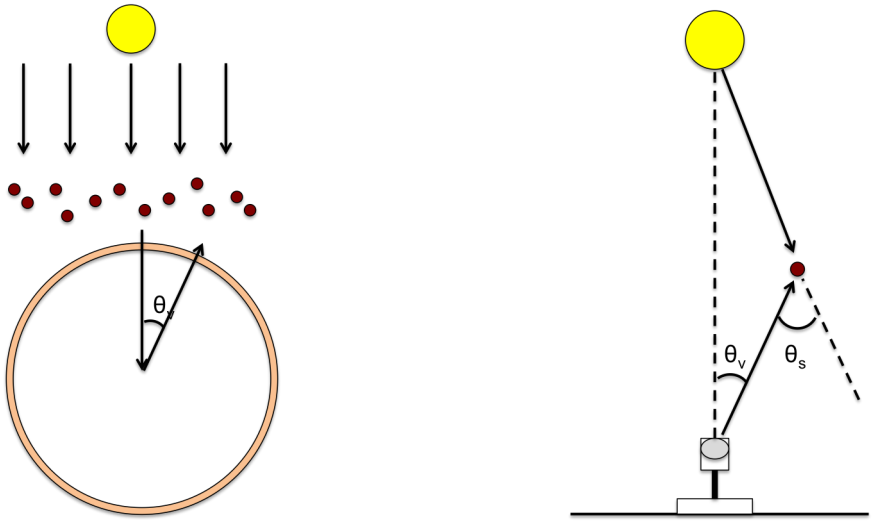

(a) (b)

Figure 3.3: Examples of (a) azimuthal sky survey geometry and (b) vertical sky survey geometry

To get a sky survey, the SSI first points as close to the sun as possible. It then images the sky by adjusting pointing in either a vertical or azimuthal direction away from the sun (figure 3.3). In the visible, this imaging sequence provides information on how light is scattered from the source beam. The angles available represent the scattering angle of a bulk medium of particles and are dependent on solar elevation. The major difference between each survey type is the angular coverage, where vertical scans are more likely limited towards higher scattering angles due to inability to image below the horizon. An I/F value relative to scattering angle is determined from this observation sequence. Figure 3.2 shows a full azimuthal survey consisting of 9 sky images. 'Mini' azimuthal sky surveys are also used, which consist of 4 images. The angular extent is generally between 50° and 60° compared to a full survey, which extends past 140° scattering angle. The images were converted to site coordinates and mapped to azimuth and elevation. All surveys are provided in table A2 in appendix A.

3.2 Radiative transfer

The model we discuss in this section and subsequent sections pertains only to the construction of the single scattering phase function, described in section 2. We use this phase function as an input to DISORT to calculate I/F or sky brightness as a function of scattering angle relative to the sun. MPFIT then iteratively minimizes the logarithmic deviates between the observations and I/F output from DISORT and returns the free parameters that describe size distribution. This includes the effective size, R_{eff}, and effective variance, v_{eff}. In the case of the bimodal size distribution, MPFIT also returns the course mode effective size, R_{2eff}.

3.3 Parameterized phase function

The single-scattering phase function for any radiative transfer calculation can be constructed in many ways. One method is to form the resulting function using a set of optical and physical parameters that describe dust aerosol scattering. The methodology for phase function formation is based on work presented in Pollack & Cuzzi (1980) and are explained in detail in Pollack et al. (1995). Updates to this method are also included in Tomasko et al. (1999) and Showalter et al. (1992). The phase function is constructed with seven parameters: n_i, G, θ_{min}, R_{eff}, v_{eff}, τ, and surface albedo. n_i, R_{eff}, v_{eff} control the shape of the phase function indirectly through the volumetric calculation of the phase function (equation 2.13). G and θ_{min} control the slope and minimum of the phase function. We adopt the adaptation for enhancement of scattering using a surface area ratio, SAR, of 1.3 (Tomasko et al. 1999). Values used for each survey are interpolated from Johnson et al. (2003) and are provided in appendix A. The radius used for construction of this phase function is a volume equivalent radius. We assume a Lambertian surface albedo using wavelength-dependent values.

This parameterized phase function sorts an ensemble of particles into two size pa-

rameter regimes, where size parameter is the ratio of spherical particle circumfrence to wavelength. Pollack et al. (1995) describes the single-scattering phase function, P(θ), by splitting the phase function into contributions from small and large particles. A single size parameter, X_{large} is defined as the split between small particle and large particle calculations. We adopt a fixed value of 5 based on the work of Tomasko et al. (1999). Extinction is calculated using Mie theory for particles with size parameters smaller than X_{large}. Particles with size parameters larger than X_{large} contribute to scattering through three different physical processes: diffraction, external reflection, and internal refraction and transmission. The transition between effects is linear. Thus, the full phase function is a combination of spherical Mie theory and nonspherical particle theory. This method is limited by the knowledge of parameters over multiple wavelengths and in the extent of extreme shapes such as an elongated cylinder. In addition, no parameterized phase function has been formulated for polarization.

The phase function at certain scattering angles is highly representative of its parameterized values. Pollack et al. (1995) provides a discussion of these sections, or zones. Generally, 10° - 30° is dominated by single scattering and can be used to retrieve particle size distribution information. This is especially true of effective size, to which the forward scattering peak is most sensitive. Scattering angles between 30° - 50° reflect the imaginary index of refraction, which in turn affects the single scattering albedo. A higher imaginary index increases particle absorption and decreases the single scattering albedo. Finally, scattering angles larger than 50° tend to be controlled by shape. This is evident when comparing phase functions of irregular particles with those of spheres (Kalashnikova & Sokolik 2004).

We use an updated Discrete Radiative Transfer code (Stamnes et al. 1988), to model I/F. DISORT loops through a layered atmosphere and calculates multiple scattering over 64 streams. The number of layers and streams are both specified by the user. The output

for DISORT is I/F radiance at user specified angles in the vertical relative to zenith and in the azimuthal relative to the source beam. For this study, DISORT returned I/F over a 90° x 180° degree sky using a single layer of randomly oriented dust particles.

In combination with this model, we provide DISORT with six inputs: optical depth, τ, solar position, μ_0, the imaginary index of refraction, n_i, single-scattering albedo, ω_0, the single-scattering phase function of the layer, P$\lambda(\theta)$, and a lower boundary condition representing the surface. The phase function is weighted with the particle size distribution and normalized accordingly so that particle size distribution parameters are the actual free parameters and not the phase function itself.

Optical depth is determined using the 671 nm filter, which is equipped with a solar filter for direct imaging of the sun. Optical depth does not vary significantly across visible wavelengths for dust (Lemmon et al. 2004) and therefore 671 nm is a good approximation to the optical depth at 754 nm. Solar zenith angle, μ_0, is provided in the image label. The lower boundary condition is assumed to be a Lambertian surface with a wavelength-dependent surface albedo given in the appendix.

Fitting is performed using the algorithm described in section 2 with modifications to fixed parameters. To constrain particle physical properties, the optical properties are held constant. This includes n_i, G, θ_{min}, and ground albedo (G_R). τ is first allowed to vary with R_{eff} and v_{eff} held constant. R_{eff} and v_{eff} are then allowed to vary while τ remains constant. This iteration is repeated twice before arriving at a result. Step size is specified within the fitting algorithm to allow for full variance of parameters over model space.

The architecture of input to the fitting algorithm is shown in figure 3.4, where input parameters are selected in order to construct the single scattering phase function. This phase function, along with optical depth, single scattering albedo, and solar incidence angle, are provided to DISORT as inputs. I/F is returned and masked to the size of the data. The logarithmic deviates are calculated within the program, and this process is repeated itera-

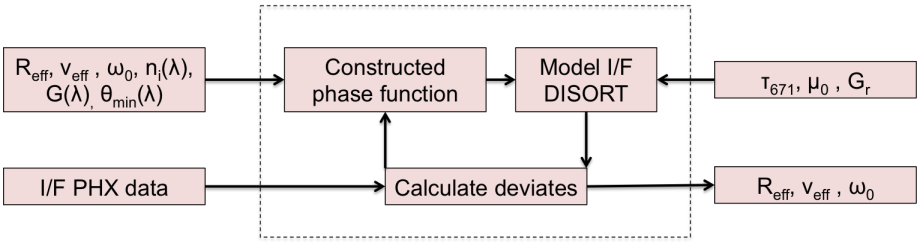

Figure 3.4: Fitting algorithm input structure

tively while varying input parameters until a default error condition within the program is achieved.

3.4 Results

Forty surveys of varying filter and scan-type (9 or 4 images) were modeled using a parameterized phase function. Each survey was tested using bimodal and gamma distributions (Hansen & Travis 1974). For each survey, we fitted modeled I/F as described previously with varying τ, a, and b while holding constant the other necessary parameters used to formulate the phase function and initiate DISORT (θ_{min}, G, n_i, and surface albedo).

We have selected three surveys to detail in our results, followed by particle size and variance results for all surveys. The three surveys selected span the mission in time and optical depth. We follow our results with a discussion of returned parameter results for all surveys and assess the accuracy of these results with respect to single scattering albedo, returned optical depth, and model error.

3.4.1 Sol 32

We show model fits for three surveys taken using the LC (969 nm), R8 (754 nm), and RC (485 nm) filters. These observations are all full-sky surveys and extend past $140°$. Figure 3.5 shows results with modeled I/F in figure 3.5a and relative deviations in figure

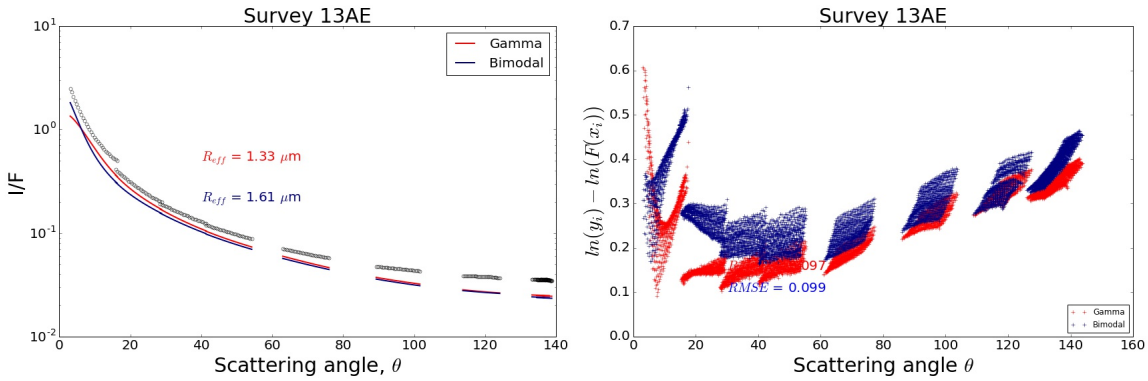

(a) (b)

Figure 3.5: Survey 13AE filter LC (a) I/F results and (b) natural log deviation

3.5b for the LC filter. The fits to I/F are moderately good at lower scattering angles, with larger error for all three filters at forward and backscattering angles. The images do not constrain forward scattering perfectly due to the nature of the observation (i.e. looking directly at the sun is prohibited). Behavior of the results next to unconstrained regions shows higher residual error. The LC filter was subject to inconsistencies in the observations due to the transparency of the CCD at this wavelength, and so deviations near 20° in figure 3.5 where this discrepancy occurs are large.

Bimodal and gamma distributions provide similar fits to the 13AE LC survey. Larger effective particle sizes cause the forward scattering peak to become steeper and multiple scattering to decrease. Both fits do not adequately model large scattering angles, which in part is due to the constraint on n_i, G, and θ_{min}. The gamma distribution produces better results between 40° and 60°, but performs worse in the forward scattering peak. The R8 filter in figure 3.6a shows again the best fits to the data using gamma and bimodal distributions and relative devation is shown in figure 3.6b. In both cases there is a decreased sensitivity in the model to scattering angles greater than 60°. For the R8 and RC filters, the gamma distribution returns the best fit within the first 20°.

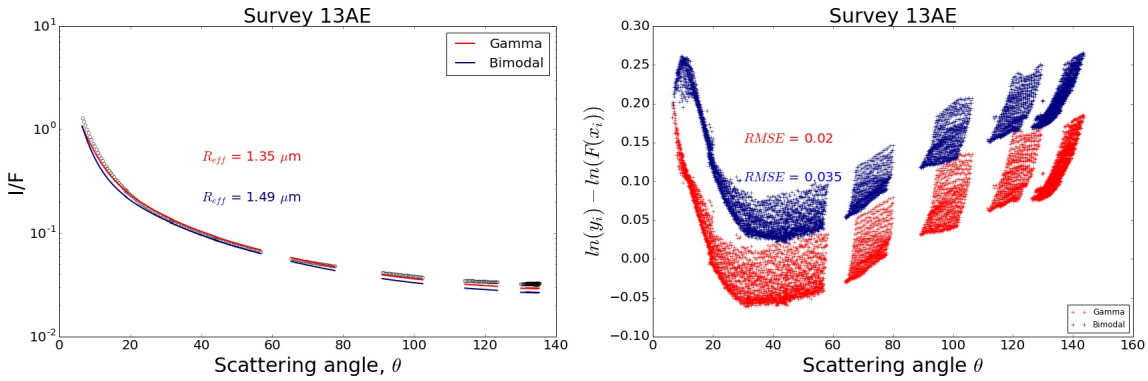

(a) (b)

Figure 3.6: Survey 13AE filter R8 (a) I/F results and (b) natural log deviation

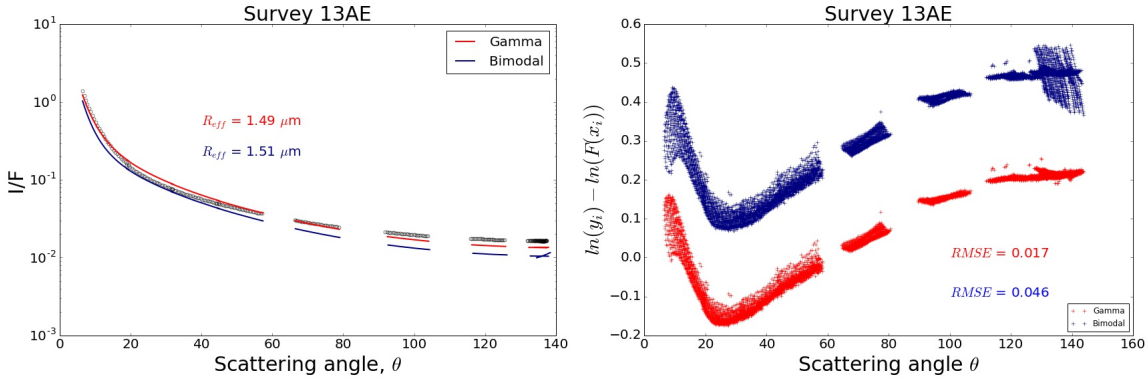

(a) (b)

Figure 3.7: Survey 13AE filter RC (a) I/F results and (b) natural log deviation

For the R8 and LC filters, model fits to scattering angles greater than 90° are worse than for forward peak fits. For RC filter results and relative error shown in figure 3.7a and 3.7b, respectively, higher scattering angles are modeled well using the gamma distribution. Though the smallest scattering angle remains unconstrained, the gamma distribution performs better both in multiple scattering and forward scattering. The bimodal size distribution causes a steeper slope in the resulting I/F in figure 3.7a compared to the results for the gamma distribution. This is due to weighting the particle size distribution towards

larger particles.

For all filters, the bimodal size distribution does not perform as well as the gamma distribution. The bimodal distribution fits for all surveys tends towards a monomodal shape regardless of the initial value for the secondary mode. The choice of an initial value of 3μm is purely to reduce fitting time while retaining the possibility of a higher returned value.

Tables 3.2 and 3.3 give parameter results and RMS values for the returned fits. The bimodal size distribution is weighted towards higher particle sizes, which causes the offset in modeled I/F compared to the observations. We present RMS values of no more than 10% for each filter and distribution choice. This is excellent agreement between both models and the observations.

Survey	Filter	Sol	R_{eff} [μm]	v_{eff}	τ	RMSE	χ^2_v
13AE	LC	32	1.33	0.18	0.80	0.097	642.53
13AE	R8	32	1.35	0.21	0.88	0.020	62.85
13AE	RC	32	1.49	0.31	0.66	0.017	213.47

Table 3.2: Returned parameter results for all 13AE surveys using gamma distribution

Survey	Filter	Sol	R_{eff} [μm]	v_{eff}	τ	RMSE	R_{2eff}	χ^2_v
13AE	LC	32	1.61	0.33	0.92	0.099	1.97	928.05
13AE	R8	32	1.49	0.30	0.87	0.035	2.53	221.94
13AE	RC	32	1.51	0.30	0.64	0.046	2.85	1131.04

Table 3.3: Returned parameter results for all 13AE surveys using bimodal distribution

Figure 3.8 shows the resulting bimodal distributions from the returned fit parameters.

For the bimodal distribution in figure 3.8, the result is a singular modal shape for best fit values. Distributions in figure 3.8 are displayed on a lognormal scale to show differences between the results, but ultimately these differences are minimal because the returned results for all filters are similar. The outlier values are mainly those for the LC filter.

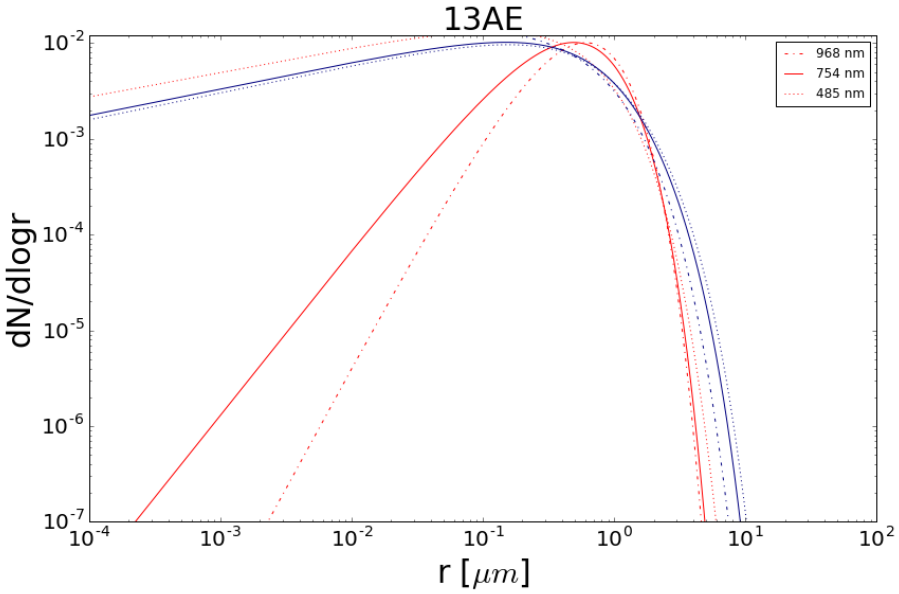

Figure 3.8: Particle size distributions for returned parameters for survey 13AE. The distributions included are gamma (red) and bimodal (navy); All distributions are normalized in this figure

There is consistency in the PSD for each filter, where smaller wavelengths return gamma distribution results that are weighted towards smaller particles. Theoretically the distribution is not wavelength-dependent. In reality, observations at different wavelengths are sensitive to different particle sizes. This wavelength dependency seen in figure 3.8 is small and is not apparent for the bimodal distributions.

3.4.2 Sol 70

Sol 70 observations include sky surveys in four filters: R2 (447 nm), L2 (447 nm), R8 (754 nm) and LC (969 nm). These four surveys comprising three unique wavelengths cover a large spectrum and allow for comparison between left and right eye results (L2 and R2). They differ from sol 32 in that only 4 images have been taken as a 'mini' azimuthal survey set. This leaves larger scattering angles unconstrained much more so than for sol 32, survey 13AE.

Figure 3.9 shows the returned results for the L2 filter next to the relative deviations. For both bimodal and gamma distributions in figure 3.9a, the curvature of the modeled I/F does not capture the extent of curvature for the observations. Both returned effective particle sizes are similar, and RMSE values are comparable. We expect similarities between each model result for this survey because higher scattering angles remain unconstrained. There is a modest improvement in fit for the forward scattering peak when using the gamma distribution.

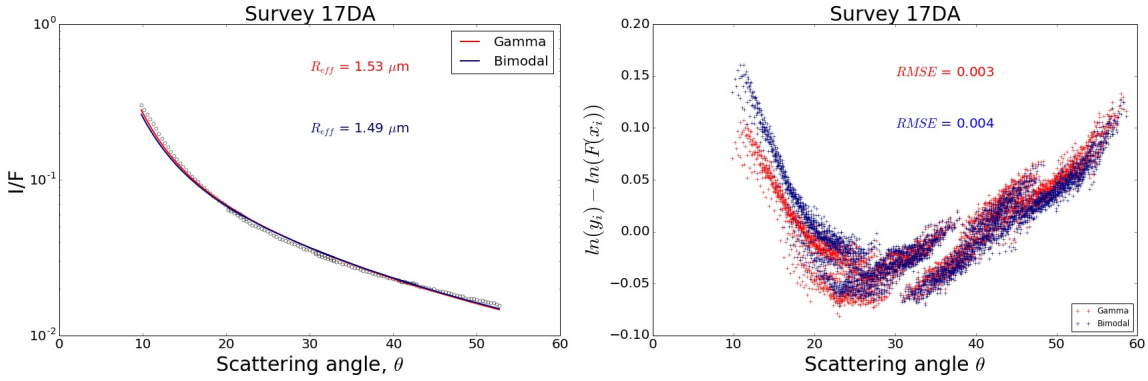

(a) (b)

Figure 3.9: Survey 17DA filter L2 (a) I/F results and (b) natural log deviation

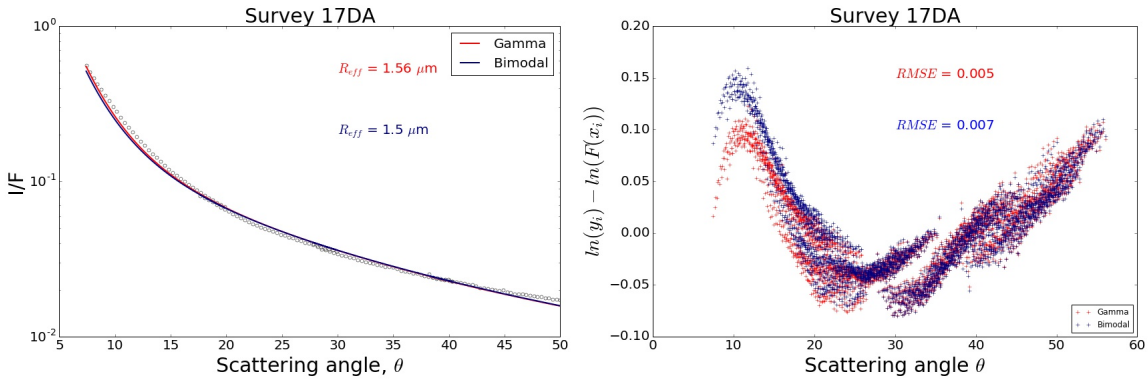

(a) (b)

Figure 3.10: Survey 17DA filter R2 (a) I/F results and (b) natural log deviation

In each corresponding residual plot, deviations are largest near forward and backward scattering peaks. Data near the forward and backscattering peaks is not available due to the type of survey used, and these areas remain unconstrained. Within $20° - 40°$, the model tends to over estimate the data, but these deviations are smaller than the values for the forward and backscattering residuals.

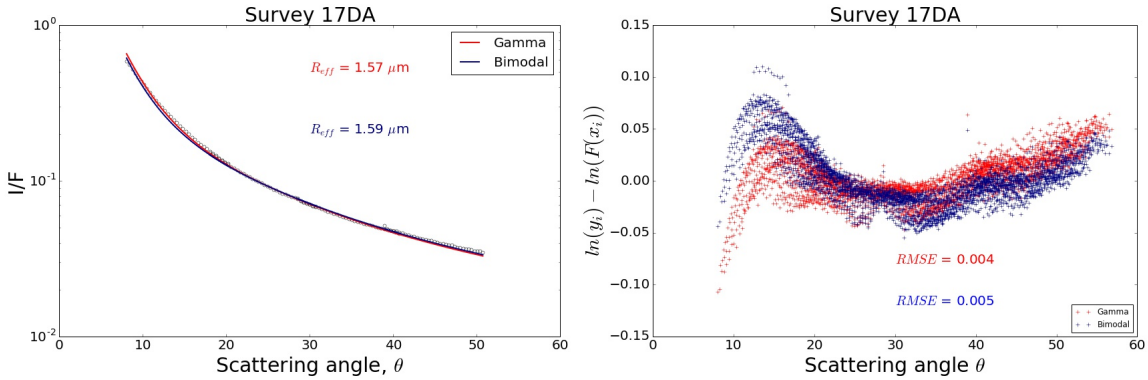

(a) (b)

Figure 3.11: Survey 17DA filter R8 (a) I/F results and (b) natural log deviation

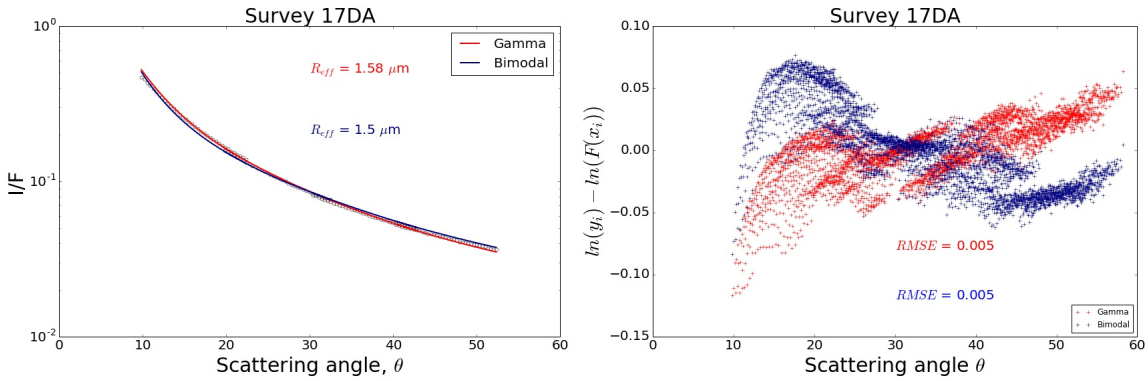

(a) (b)

Figure 3.12: Survey 17DA filter LC (a) I/F results and (b) natural log deviation

Results in figures 3.10 through 3.12 are comparable to those of figure 3.9 in that the forward scattering peak fits well and is modestly better represented using the gamma distribution. Curvature of the overall I/F shape is steeper for both distributions, and error in the region of $20°$ to $30°$ is almost as much as the unconstrained forward peak. This is not surprising, as the normalized phase function compensates for changes in the forward scattering peak.

Tables 3.4 and 3.5 provides RMS and reduced chi-square values for each survey. χ_v^2 values are reduced with the degrees of freedom. These values for sol 70 are lower than those for sol 32, survey 13AE because the calculation does not contain large deviations for scattering angles larger than $60°$. If the best fit value for any survey can be accepted to be ${\chi_v}^2$ = 1.0 subject to the selected weights, then the lowest values from each surveys represent the best model fits. In all cases the bimodal distribution tends to deviate more than that of the gamma distribution. This suggests that regardless of the fit the general distribution is both monomodal and tightly constrained in variance for these wavelengths.

When comparing table 3.4 and table 3.5, we can see similar RMS values for each survey and slightly lower χ_v^2 values for gamma distributions. At most, the bimodal distri-

Survey	Filter	Sol	R_{eff} [μm]	v_{eff}	τ	RMSE	χ^2_v
17DA	L2	70	1.53	0.26	0.29	0.003	16.27
17DA	LC	70	1.58	0.30	0.37	0.005	4.70
17DA	R2	70	1.56	0.26	0.29	0.005	16.41
17DA	R8	70	1.57	0.27	0.32	0.004	3.96

Table 3.4: Returned parameter results for all 17DA surveys

Survey	Filter	Sol	R_{eff} [μm]	v_{eff}	τ	RMSE	R_{2eff}	χ^2_v
17DA	L2	70	1.49	0.29	0.34	0.004	2.24	17.39
17DA	LC	70	1.50	0.30	0.45	0.005	2.61	9.79
17DA	R2	70	1.50	0.30	0.32	0.007	2.17	21.37
17DA	R8	70	1.59	0.33	0.34	0.005	2.07	6.70

Table 3.5: Returned parameter results for all 17DA surveys

bution, which still tends towards a mono-modal shape, fits the data almost as well as the gamma distribution.

Finally, resulting particle size distributions shown in figure 3.13 correspond well for larger particle sizes. Discrepancies in lower particle values arise from insensitivity of the survey to smaller particle sizes. This is due to the wavelength of observation, which tends to be sensitive to sizes near the nominal wavelength. For the gamma distribution, there is a slight wavelength dependence. This dependence is more pronounced for bimodal size distributions.

3.4.3 Sol 81

Only one filter is available for sol 81. I/F results for R8 shown in figure 3.14a, and lognormal error is shown in figure 3.14b. Though there is little constraint towards higher scattering angles, the forward scattering peak is best represented using the conventional gamma distribution.

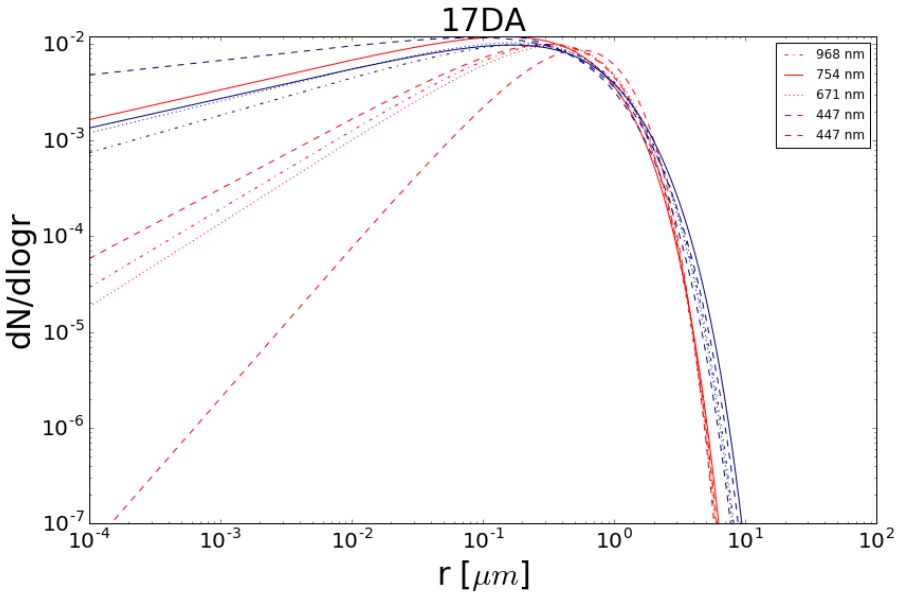

Figure 3.13: Particle size distributions for returned parameters for survey 17DA. The distributions included are gamma (red) and bimodal (navy); All distributions are normalized in this figure

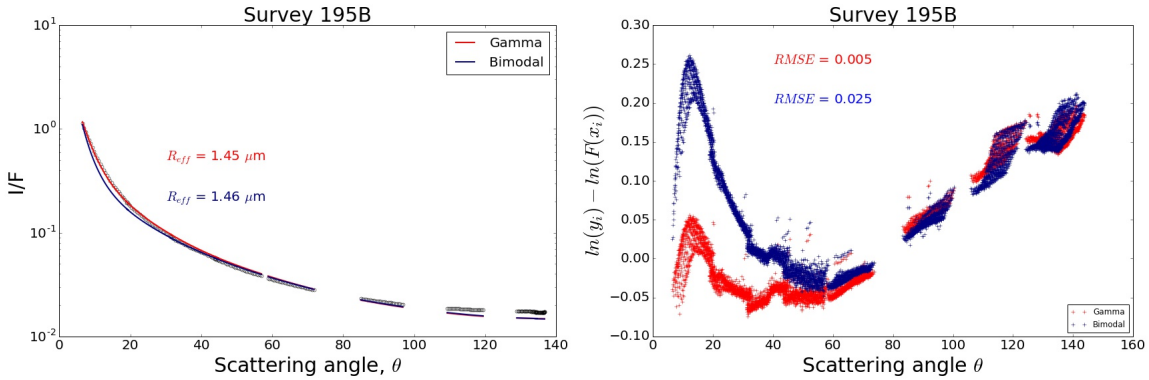

(a) (b)

Figure 3.14: Survey 195B filter R8 (a) I/F results and (b) natural log deviation

RMSE and χ^2_v results in tables 3.6 and 3.7 furthermore support the use of a gamma distribution and show an increase in error for the bimodal curve. Again, the results show a tendency towards a mono-modal shape. The distributions based on the returned parameter

Survey	Filter	Sol	R_{eff} [μm]	v_{eff}	τ	RMSE	χ^2_v
195B	R8	81	1.45	0.28	0.31	0.005	83.89

Table 3.6: Returned parameter results for all 195B surveys

values are shown in figure 3.15. We can see almost an exact match in the curves, with the bimodal distribution encompassing larger particle sizes. The returned effective particle size and variance does not change drastically from the initial 1.5 μm and 0.3 values used for fitting. This is similar to the two previously discussed sols. The fits to I/F in figure 3.14a match closely the sky survey observations.

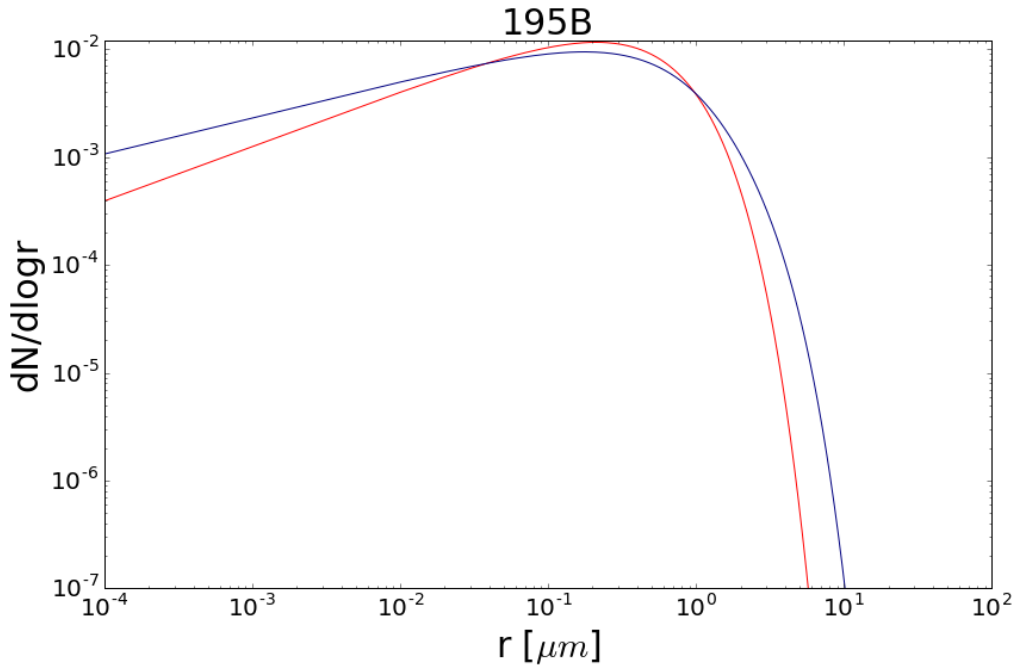

Figure 3.15: Particle size distributions for returned parameters for survey 195B. The distributions included are gamma (red) and bimodal (navy); All distributions are normalized in this figure

Survey	Filter	Sol	R_{eff} [μm]	v_{eff}	τ	RMS	R_{2eff}	χ^2_v
195B	R8	81	1.46	0.3	0.34	0.025	2.85	123.54

Table 3.7: Returned parameter results for all 195B surveys

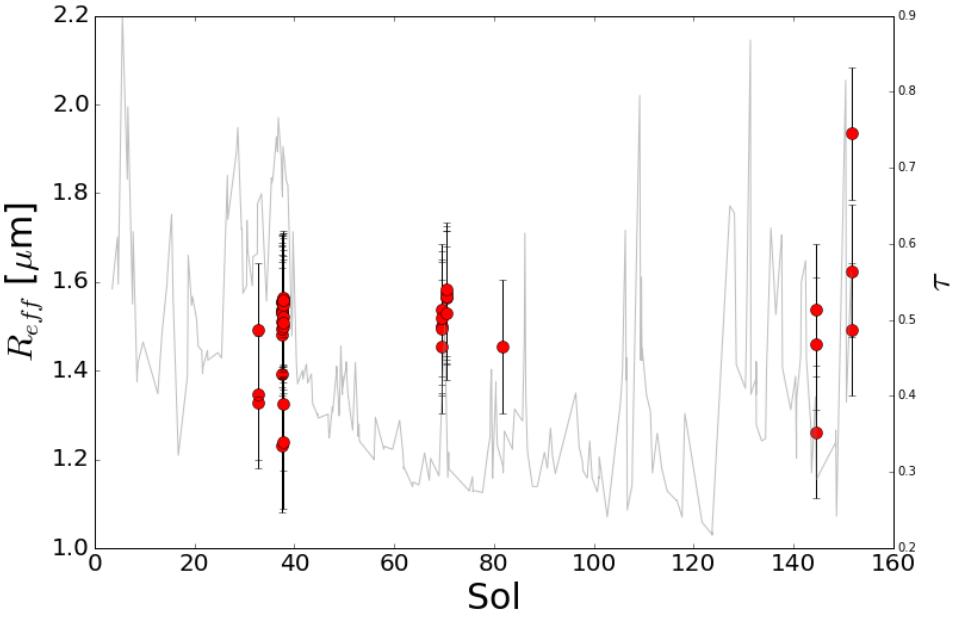

Figure 3.16: Returned effective particle sizes for gamma PSD

Distributions in figure 3.15 are similar between bimodal and gamma models. Differences in the forward scattering peak are caused by tendencies towards larger particles. Sensitivity to smaller particles is not available when using the R8 filter. Ultimately the resulting curves are quite similar in shape and value.

3.4.4 Particle properties

This section contains results only for the gamma PSD. Based on fits for sol 32, 70, and 81, the gamma distribution does well in reproducing the observed sky brightness. These

results include all surveys in all wavelengths.

Figure 3.16 shows effective particle sizes across the mission for only the gamma PSD plotted against the background 451 nm optical depth value. Returned particle sizes range from 1.0 μm to 2.0μm. The error bars represent 10$\%$ adopted error in particle size value and are discussed following these results. Throughout most of the mission, the particle size does not vary significantly from 1.5 μm.

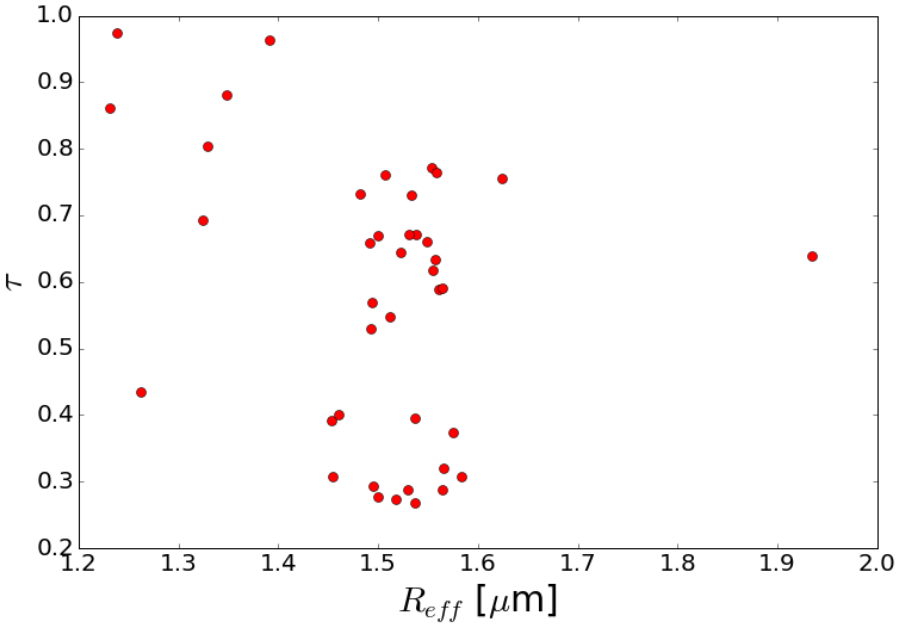

Figure 3.17: Scatter plot of particle size with returned optical depth for gamma PSD

There is no correlation in effective particle size with optical depth for the gamma distribution. Figure 3.18 shows effective particle variance similar to Figure 3.16. Returned particle variance ranges from 0.15 to 0.5 in figure 3.18. Most values for effective variance do not deviate from the initial value of 0.3, and overall the fits show little sensitivity to this parameter. The effects of variance are more readily observed within the range of $20° - 30°$

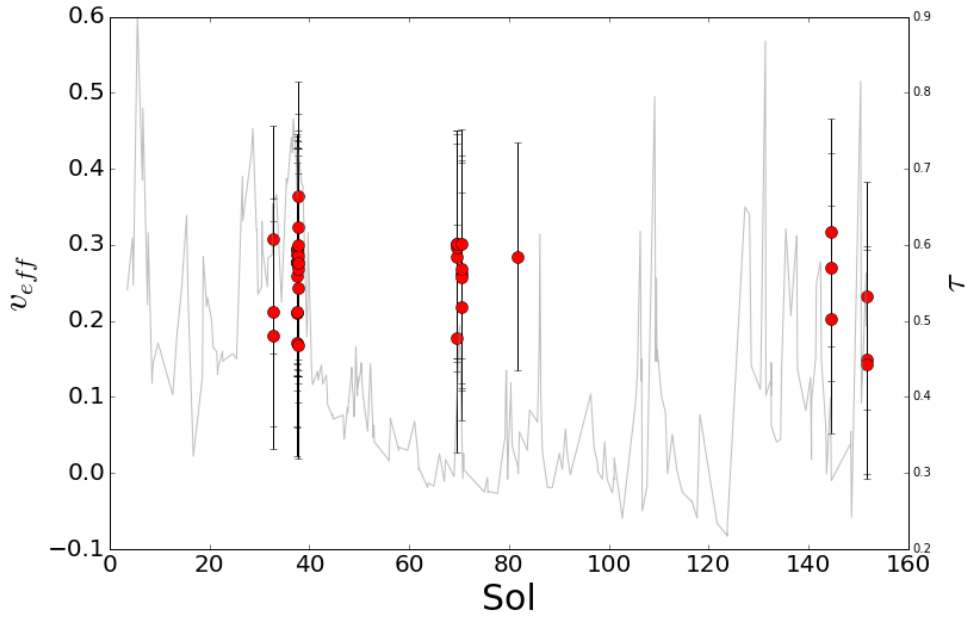

Figure 3.18: Returned effective particle variance for gamma PSD

scattering angle, but effects from particle size can offset these changes.

To date, Wolff et al. (2009) provides the best estimate to ω_0, which shows a generally flat value across visible wavelengths with a steep decline in the near UV. Using the parameterized model, the ω_0 is calculated using the final returned parameters from fitting. Figure 3.19 shows the resulting ω_0 values for all surveys fit using the gamma particle size distributions plotted against the values obtained from Johnson et al. (2003). Values returned when using a gamma distribution (Hansen & Travis 1974) show consistency with those from Johnson et al. (2003).

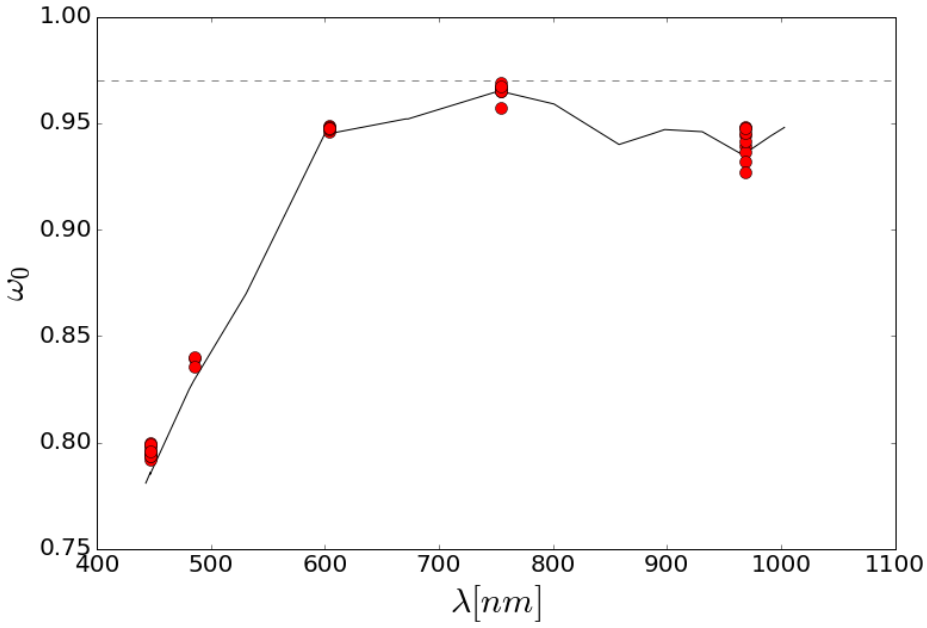

Figure 3.19: Single scattering albedo for all PSD as a function of wavelength, where the black line is the reference single scattering albedo determined in Johnson et al. (2003)

τ is expected to vary in time throughout each sol, and aside from natural diurnal variation, random dust loading events and atmospheric fluctuations can possibly cause changes between the time of the optical depth measurement and surveys. Optical depth is allowed to vary within the fitting algorithm. This provides some flexibility to account for errors in optical depth due to offset in timing of observations. Figure 3.20 shows the returned optical depth after fitting for all surveys plotted against the 451 nm optical depth. Generally the returned parameter falls within 30% of the initial value, marked on the figure.

3.4.5 Uncertainty

For any observation consisting of multiple images, random fluctuations in atmospheric conditions at the time of each image as well as between images contributes unknown uncertainty to each measurement. Instrument noise and systematic error in calibration can

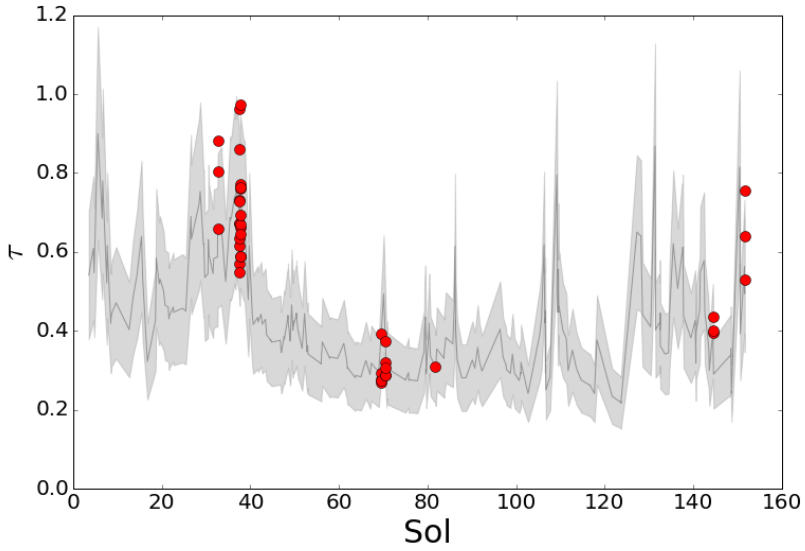

Figure 3.20: Returned fitting optical depth, where the grey shade represents a 30% change in optical depth from the initial 671 nm value

add to the uncertainty in I/F, resulting in a less accurate fit.

Deviates are calculated for each fit between the model and data (equation 2.17) and minimized within MPFIT. The sum of square residuals reduced with the degrees of freedom tells us the goodness of our fit and makes possible comparisons between different PSD types. We use the measure of χ^2_v and RMS to determine the best fit for each PSD.

Upon determining that there is little evidence for using a bimodal PSD over the gamma distribution, what we are mostly interested in is our confidence in returned parameter values for the gamma PSD. Careful accounting of error propagation through the model is not a trivial task, and cannot be assessed directly. MPFIT returns parameter error from the computed covariance matrix, but these results are subject to the weights used in the fitting process, which are in turn subject to variations in the atmosphere with time and space as well as to instrument calibration errors and noise.

The covariance matrix values returned through MPFIT for parameter error are on the

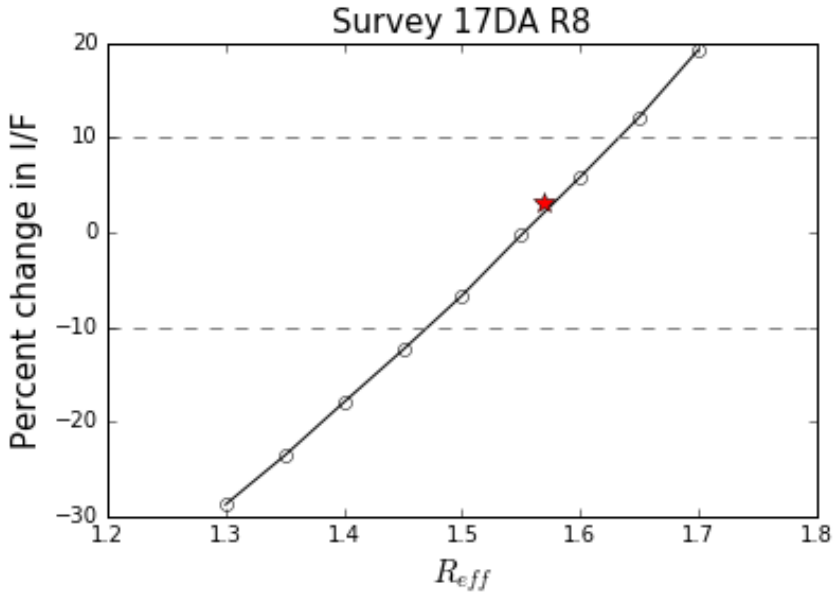

Figure 3.21: Percent change in the maximum value of I/F using best fit parameters for changing R_{eff}, where the star represents the best fit effective particle size returned from fitting

order of 0.0002. This is too small to be believed, so we attempt to quantify parameter uncertainty within the model using other techniques. Assessing uncertainty in parameters is a complex process, and is complicated even more by the lack of repetitive data.

In the process of determining parameter uncertainty, we test two methods for estimation. We first randomly varied the input parameters to simulate data sets. These simulated data sets were used to create a distribution of values for each measurement in our sky survey. We then calculated weights from this distribution and attempted to fit, with better precision, the model to our data. In addition to this, we also added random noise with an assumed standard deviation for each data point of $\sqrt{x_i}$ to the original data in order to see the returned 'best fit' parameters. In both cases, the fits were unconvincingly low, on the order of the original uncertainties.

The PSD in any moment in time should not be a function of wavelength. That being

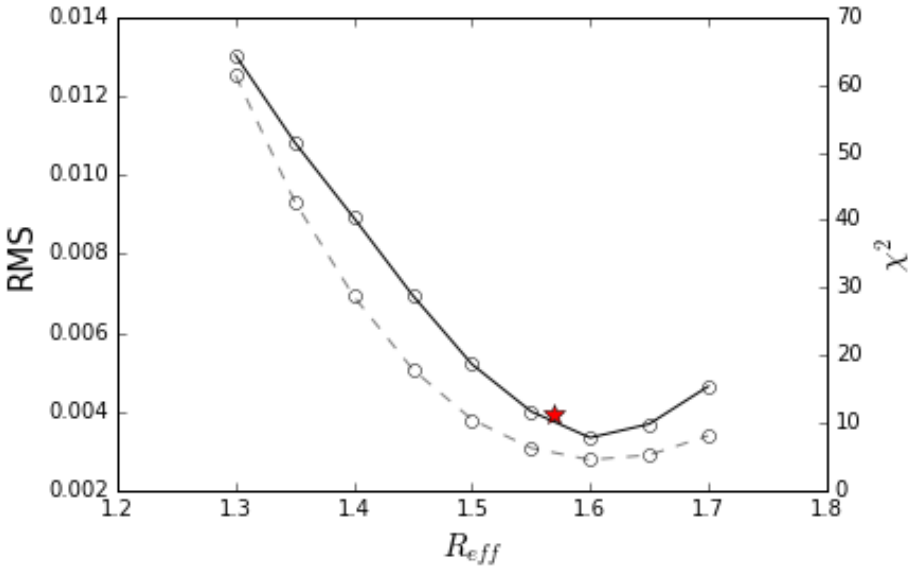

Figure 3.22: RMS (solid black line) and χ^2_v values (dashed grey line) returned from the 17DA R8 filter model fit

said, different filters are sensitive to different populations of dust so we expect some deviation between the filter values themselves. For the 13AE and 17DA surveys, we performed fits over multiple filters. The standard deviation between the best-fit R_{eff} results for 13AE and 17DA are 0.08 and 0.02, respectively.

In figure 3.21 we show the percent change in the maximum I/F calculated using the best fit parameters when R_{eff} is varied. For all other values held constant, we can see a linear change in the maximum value, which is sensitive to particle size. For a 10% change in the maximum value of I/F in any direction, we see a change on the order of 0.1 in the effective particle size. Figure 3.22 shows the returned RMS and χ^2_v plots for a variation in R_eff with the best fit value marked with a red star. The fit returns values very close to the minimum in both RMS and χ^2_v.

Finally, we wish to assess the nature of returned parameter size over the course of the mission. Figure 3.17 shows little correlation with optical depth, and figure 3.16 shows

little change from the initial input value of 1.5 μm. These results suggest there is no time dependency in effective particle size. The standard deviation over the course of the mission for all R_{eff} returned using the gamma PSD is 0.12, which is close to a 10% range. Ultimately we choose to adopt a 10% error for each parameter to be consistent with Tomasko et al. (1999). In this way, we can be fairly sure that the returned fit parameters presented in this work are within the range of 1.54 ± 0.15 μm.

3.5 Summary

We present results for particle distribution properties using modeled I/F fits to Phoenix SSI sky surveys. The results show an effective particle size of 1.54 ± 0.15 μm that does not vary over the course of the mission. Similarly, an effective variance of 0.26 ± 0.1 where variance also does not change significantly over the course of the mission. Our results are consistent with previous work, namely that of Pollack et al. (1995) for corrected Viking Lander images and Tomasko et al. (1999) using Pathfinder surveys.

This work tests the possibility of a bimodal size distribution, however best fit values tends towards a single mode distribution. If there is any bimodal distribution of particles, it is likely not sensible using ground observation techniques. Though particle size is fairly consistent, optical depth still varies in time. Visible wavelength observations are sensitive to scattering, however the optical depth represented in this work is a total column extinction. This work suggests that its value is dominated by absorption, which can have a large impact even for a slight change in imaginary index of refraction. Furthermore, absorption is dominated by smaller particles, to which sky surveys in this wavelength range are insensitive.

The single scattering albedo calculated from the volumetric phase function is consistent with values from Johnson et al. (2003). This is not surprising because the values used to construct the phase function are taken from this work. That being said, ω_0 is also con-

sistent with results for Wolff et al. (2009). This work used an assumed shape of equant cylinders rather than an empirical phase function model specifically to retrieve ω_0. The calculated values in our results are consistent across models.

Future work using this model is limited because of the small range of wavelengths for which assumed parameter values such as n_i and θ_{min} have been determined. Furthermore, most modeling efforts have shifted to assumed particle shapes as they provide more robust and encompassing phase function calculations. This topic is discussed further in the following section.

4. PARTICLE SHAPE AND DISTRIBUTION AT THE PHOENIX LANDER SITE USING AN ELLIPSOIDAL MODEL

Dust particles are often modeled as spherical for the convenience of using a phase function that is easy to construct. Mie theory has been solved over a wide range of size parameters and wavelengths, and its use saves computation time. Dust is not spherical, however, and has a complex shape with distinctly sharp edges (e.g. Kalashnikova & Sokolik 2004, Smith 2008, Clancy & Wolff 2003, Pollack et al. 1995).

A significant flattening of the phase function exists for nonspherical particles at angles greater than 50° that can cause error in retrievals of parameters or radiance models (Dubovik et al. 2006). This is particularly important in the case of satellite imagery, lidar measurements, and in general any view of the atmosphere past 90° scattering angle. This effect is more prevalent when scattering dominates in the visible wavelength regime. Furthermore, Martian climate models require dust vertical profiles and particle size distributions, which change spatially and temporally, and both the shape of the phase function at large scattering angles and energy deposition outside the visible wavelength range must be addressed (Montmessin et al. 2004).

Modelers account for nonsphericity of Martian dust through a range of different shapes. As noted by Wolff et al. (2009) and Clancy & Wolff (2003), a solution is to assume a shape for the dust that models light scattering reasonably well. Assuming the shape reduces the number of parameters necessary for modeling. In the case of irregular particles, spherical Mie theory cannot reproduce the scattering observed due to irregular particle shapes. Wolff et al. (2009) use randomly oriented cylinders with a constant aspect ratio, and spheroids generally produce consistent results for observed radiances when tested against inversion algorithms on Earth (Dubovik et al. 2006). Clancy & Wolff (2003) show that observations

are better modeled using disk shapes than spheres. Dabrowska et al. (2015) show that Mie theory is distinctly incorrect for modeling irregular particles in all scattering matrix elements.

In section 3, we used a parameterized phase function in order to account for particle non-sphericity but not without limitations. Past 150° scattering angle, the phase function is not well constrained, and the parameters that are needed to construct the phase function have only been retrieved for a small subset of visible and near IR wavelengths. The parameters themselves come with inherent model error, and this increases the complexity in the uncertainty analysis.

Meng et al. (2010) presents a method that retrieves optical information for randomly oriented ellipsoidal shapes through a series of rigorous models including DDA, T-matrix, and IGOM, which are complex computational tools that compute particle properties for individual shapes. An ellipsoidal shape can take many different forms depending on the choice of axis lengths. The phase function is constructed in this case using a database of ellipsoidal shapes described in Meng et al. (2010). For each shape, the database contains the optical cross-sections, efficiencies, and phase matrix elements. In this way, the self-consistent physical model constrains scattering properties.

We assume the shape to be ellipsoidal for several reasons. First and foremost, a database exists that provides particle properties (Meng et al. 2010). These properties include all six scattering matrix elements, scattering efficiencies, and scattering cross-sections for up to 100 size parameters. This not only is an upgrade to that of Wolff et al. (2009), who calculated scattering properties using a computationally expensive T-matrix algorithm, but also extends the wavelength range available compared to that of the empirical model in section 3. Second, the addition of a third axis gives an extra degree of freedom for size and orientation, which makes an ellipsoid a very flexible shape in terms of modeling. Research on dust aerosol properties shows that a suitable distribution of

ellipsoids can produce scattering similar to that of irregularly shaped dust for terrestrial atmospheres (Bi et al. 2009, Meng et al. 2010, Merikallio et al. 2015).

Application to Martian atmosphere has also been established. Merikallio et al. (2013) and Merikallio et al. (2015) investigated the applicability of ellipsoids by comparing simulations against laboratory data for palagonite. Their results show a good match to all scattering matrix elements. In addition asymmetry parameter and single scattering albedo were found to depend on assumed shape distribution. Pike et al. (2011) studied Atomic Force Microscope images to show that the shape of the dust was ellipsoidal. Their work only compares, however, theoretical scattering matrix elements and does not attempt to fit actual observations.

The goal of this section is to fit modeled I/F to Phoenix data by varying shape distribution parameters and to compare the quality of the fit to those for the parameterized phase function described in section 3. Section 2 discusses the radiative transfer model used for fitting and section 3 provides results of the fit and a discussion of the applicability of ellipsoids as compared to previous methods. Section 4 lists conclusions and discusses the next steps towards testing the particle shape.

4.1 Methods

The work in this section uses the same approach as the previous section by running a full radiative transfer model to iteratively fit radiometric images of the Martian sky to a modeled I/F. The data set is comprised of the same images sets described previously, but testing for ellipsoids is focused on shape of fit, and only the R8 filter (754nm) is considered here. The model is constructed by assuming a set of physical parameters to describe both the size and shape distributions.

An ellipsoid is defined by three axes, a, b, and c, rather than just two for the case for spheroids. This third axis, shown in figure 4.1 makes the shape more flexible when fitting

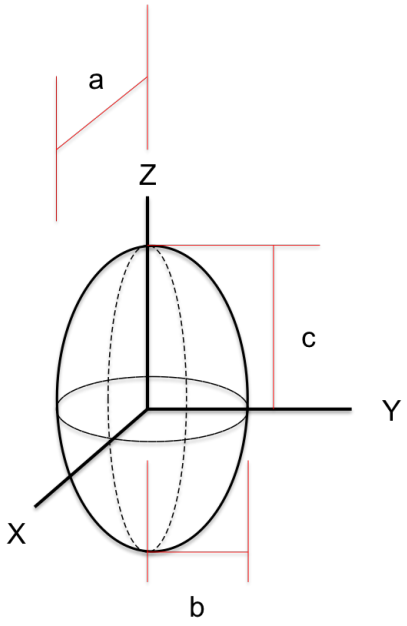

Figure 4.1: Example elllispoid shape with labeled axes

to observations. For three axes a, b, and c where c is the polar axis, c > b > a. Thus, a single particle is described by two aspect ratios ε_{ab} = b/a and ε_{ac} = c/a corresponding to the ratios of the axes y/x and z/x, respectively. Specifying a pair of aspect ratios within the database returns the cross sections, surface-area equivalent size parameters, and the orientation-averaged scattering elements P_{11} and P_{12}. The first element, P_{11}, describes single scattering and the second element, P_{12}, describes linear polarization. The database is arranged according to refractive indices. For n_r = 1.5, five distinct sets of imaginary indices are included, each with 46 shapes. Each shape contains the efficiencies, cross-sections, volumetric and surface-area equivalent size parameters, and scattering matrix elements. The imaginary index is constrained using values from Wolff et al. (2006). These values are the best retrievals known to date. Notably, the imaginary index is very flat across the visible spectrum. For all retrievals of particle size, variance, and shape in this section, the imaginary index is held constant at 0.001.

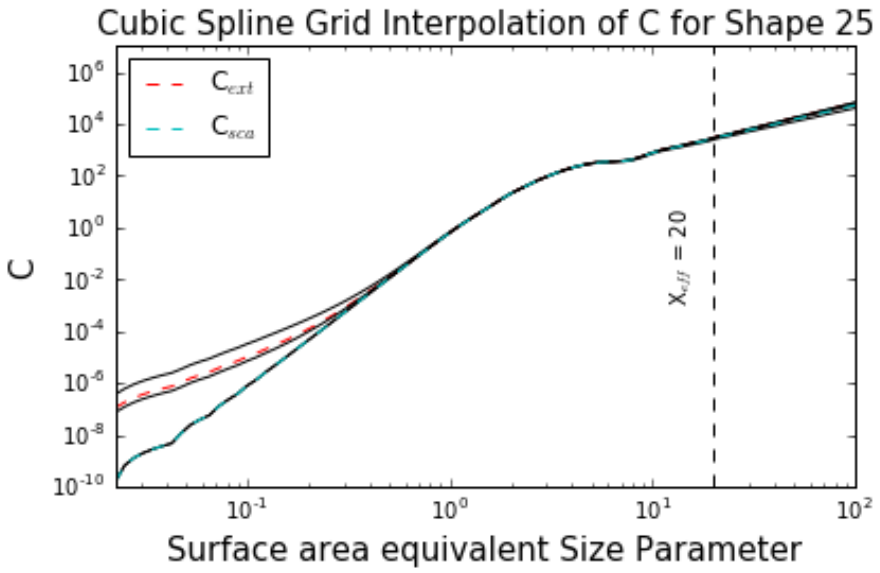

Figure 4.2: Scattering (cyan) and extinction (red) cross section for selected shape with interpolated values using intermediate imaginary index of refraction

Figure 4.2 shows an example scattering and extinction cross sections for a randomly selected shape within the database. The extinction and scattering cross sections shown in figure 4.2 are interpolated between two imaginary refractive indices. In this particular case, the scattering and extinction cross section are not the same for much smaller size parameters and size parameters extending past X_{eff} = 20. Smaller size parameters correspond to smaller particle sizes when wavelength is held constant, as is the case in this work. Extinction is dominated by scattering for most particle sizes, but absorption does contribute significantly at smaller size parameters.

Figure 4.3 shows the 46 shapes contained in the database with labeled prolate, oblate, and ellipsoidal values. The final weights are normalized to one during fitting. We choose a bivariate gaussian distribution (equation 4.1) to parameterize the shape distribution in order to minimize the number of free parameters within the fitting algorithm. Four parameters describe the bivariate distribution: μ_x, μ_y, σ_x, σ_y.

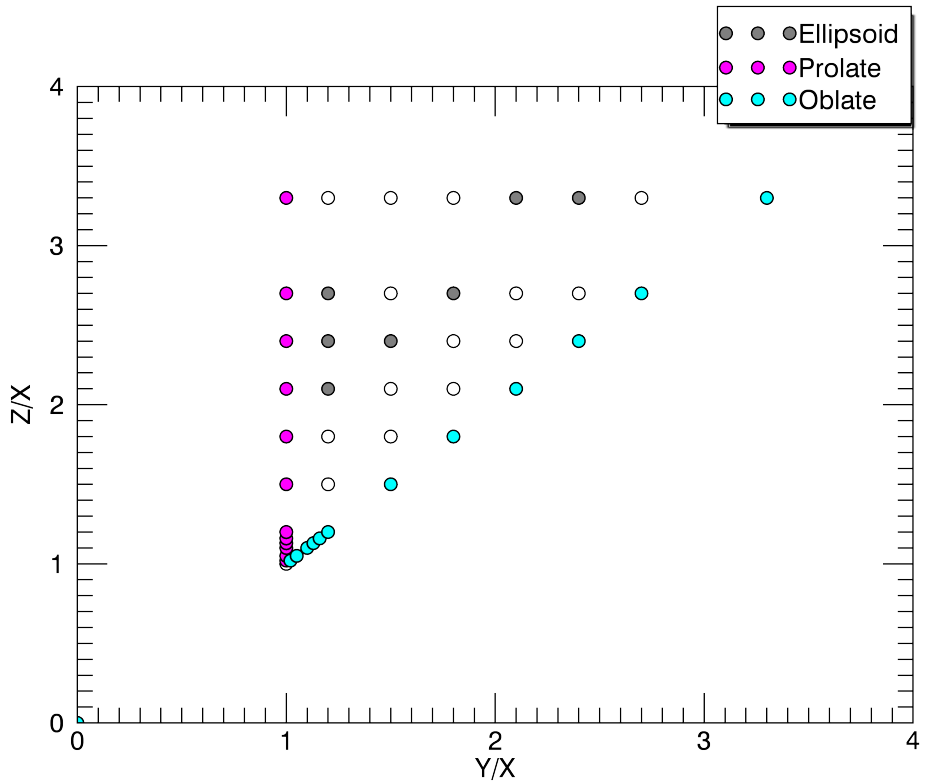

Figure 4.3: The circles, open and filled, represent the shapes contained in the database, where the blue and magenta filled circles are oblate and prolate spheroid shapes, respectively; the filled grey shapes represent a subset of distinctly ellipsoidal shapes

$$wt = \frac{1}{2\pi\sigma_x\sigma_y} e^{-\frac{1}{2}\left(\frac{(\varepsilon_{ab}-\mu_x)^2}{\sigma_x^2}+\frac{(\varepsilon_{ac}-\mu_y)^2}{\sigma_y^2}\right)} \tag{4.1}$$

The database contains optical cross section, geometric cross section, and phase function information for each shape. For a given particle size distribution, the volumetric phase function is calculated according to equation 2.13, and a weighted shape distribution is incorporated into the phase function calculation according to equation 2.15. Figure 4.4 shows the included phase functions for each shape and size parameter at five different imaginary indices. The structure of each phase function changes dramatically with shape. Similarly, using the volumetric extinction and scattering efficiencies, the single scattering

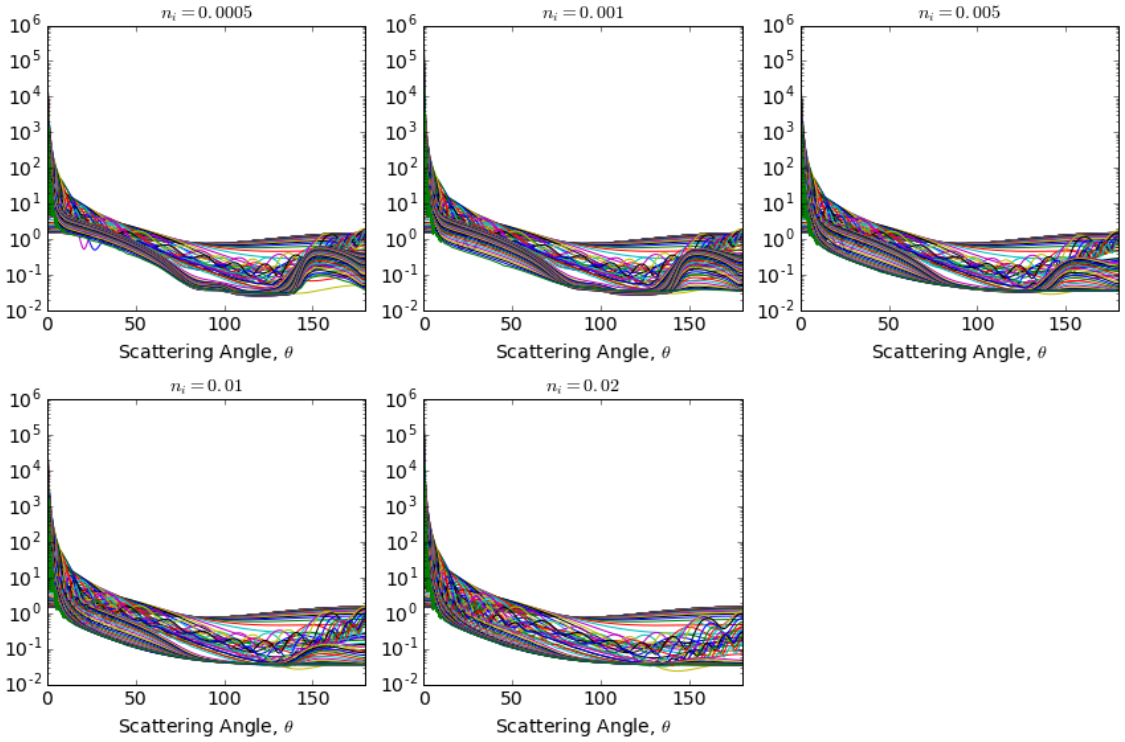

Figure 4.4: Phase functions for all shapes for selected imaginary indices of refraction.

albedo is calculated. The single scattering albedo does not vary considerably from 0.97 in the visible (Lemmon et al. 2004), and this value is used as a quality marker.

The fitting algorithm is the same as that in section 3. The fit first allows optical depth to vary followed by effective particle size, variance, and finally shape. For purely ellipsoidal shapes, these steps are repeated twice, after which all parameters are allowed to vary. Parameter uncertainty is returned in a covariance matrix through the fitting algorithm and the square sum residual is calculated for the final parameter results. The remaining input parameters, P$\lambda(\theta)$ and ω_0, are dependent on the shape of the dust within this layer, which is chosen to be a distribution of ellipsoidal shapes each with their own particle size distribution. Light is scattered according to the volumetric properties of this ellipsoidal layer.

Model	R_{eff} [μm]	v_{eff}	χ^2	ω_0	RMSE
Parameterized	1.35	0.21	62.85	0.97	0.02
Ellipsoidal	1.5	0.12	13.85	0.98	0.004

Table 4.1: Returned parameter results for 13AE using two different phase function models.

4.2 Results

We present our results in a similar fashion to that of the previous section by first showing examples of individual fits for sols 32, 81 and 70. We then assess the error in model parameters and present overall particle size and variance results. These sols are chosen to show results for high optical depth days (sol 32), low optical depth days (70 and 81) and long azimuthal scans (sol 32 and sol 81, 9-image) vs. mini azimuthal scans (sol 70, 4 images).

4.2.1 Sol 32

We begin by running the new model using ellipsoidal shapes with an assumed bivariate shape distribution. We allow the fitting algorithm to individually fit τ, R_{eff}, and v_{eff} before fitting all four shape parameters. The particle size distribution used is the gamma distribution (Hansen & Travis 1974). Figure 4.5a shows I/F model result compared to that of the corresponding parameterized phase function model from section 3 with the same particle size distribution. The χ^2_v values are compared using the log residuals from equation 2.17 in table 4.1. The improvement in the forward scattering peak and at higher scattering angles can be seen in the residuals of figure 4.5b.

The returned effective particle sizes in table 4.1 do not differ significantly, though figure 4.5a shows a closer fit to smaller scattering angles. Within a range of 10% uncertainty, the effective particle sizes are a close match. Effective variance differs significantly outside 10% of the parameterized model variance. As will be discussed in later sections, I/F

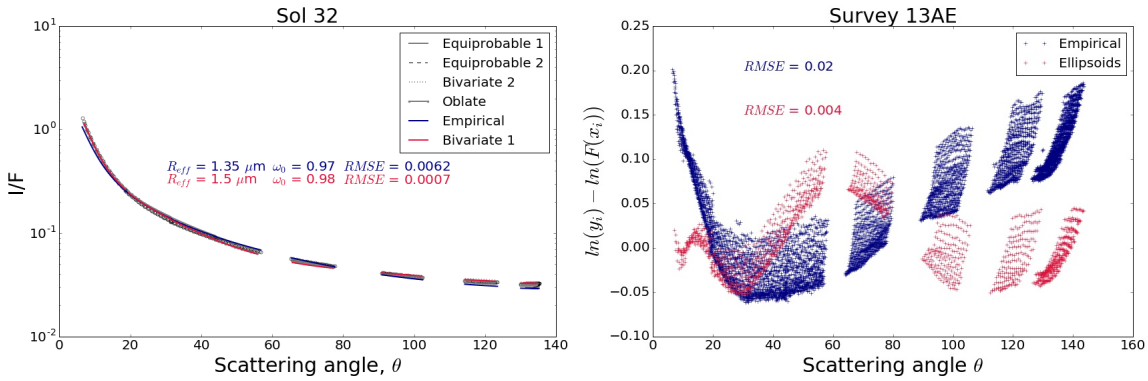

(a) (b)

Figure 4.5: Survey 13AE filter R8 (a) I/F results and (b) natural log deviation

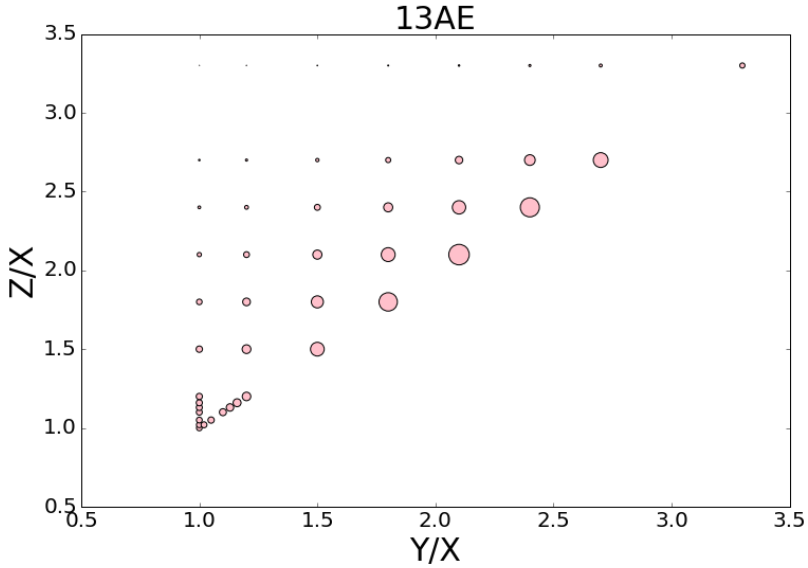

Figure 4.6: Relative weighting results for sol 32 survey 13AE returned shape distribution where size represents normalized weight value

is sensitive to the shape at the same scattering angles as variance, so the effective variance result is only constrained through minimizing the deviates within the fitting algorithm. Despite this flexibility, the ellipsoidal shape model still returns an improved χ^2_v value, where

deviates are calculated for both models according to equation 2.17. The parameterized shape distribution returned from fitting is shown figure 4.6, where the resulting distribution is heavily weighted towards more even aspect ratios. The returned shape distribution does not tend towards aspect ratios of 1.0, which is consistent with non-spherical shapes.

4.2.2 Sol 81

Survey 195B on sol 81 shown in figure 4.7a is compared to results returned using a parameterized phase function. Towards larger scattering angles and smaller scattering angles, the fit is improved marginally. This reduces the natural log deviations in this range (figure 4.7b). Between 20° and 60° scattering angle triaxial ellipsoids cannot reproduce the I/F curve as well as the parameterized model. Compared to the scan from sol 32, the fitting algorithm does not converge on the appropriate I/F curvature.

Model	R_{eff} [μm]	v_{eff}	χ^2_v	ω_0	RMSE
Parameterized	1.45	0.28	83.89	0.97	0.005
Ellipsoidal	1.96	0.44	94.59	0.97	0.006

Table 4.2: Returned parameter results for 195B using two different models for phase function.

The returned effective particle size provided in table 4.2 also deviates from the returned size using the parameterized model. A jump in value to 1.96 μm and a higher variance are returned, while χ^2_v and ω_0 retain similar values. The wiggle in midrange scattering angles is controlled within shape distribution by the σ_x and σ_y parameters. For sol 32, these values remained near 1.0 each, while for sol 81, the values decreased to near $\sim$0.5. In addition to this, mean values for the bivariate distribution, μ_x and μ_y, fall closer to spherical particles. The inclusion of more spherical shapes causes distinct decreases in the

modeled I/F.

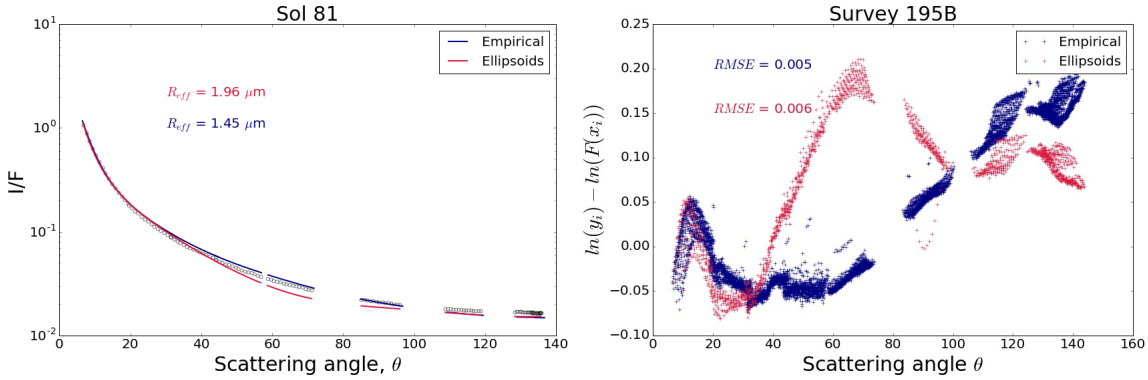

(a) (b)

Figure 4.7: Survey 195B filter R8 (a) I/F results and (b) natural log deviation

Figure 4.8 shows that the weighting results tend towards spherical particles. Aspect ratios closer to one represent near-spherical shapes. These spheres are weighted heavily within the distribution, which likely causes the deviations seen between $60°$ and $80°$. Careful selection of weights is therefore necessary in order to avoid these distinctly spherical shapes.

4.2.3 Sol 70

Shape sensitivity within the phase function and the returned I/F are unconstrained in figure 4.9a due to the smaller range of scattering angles available for fitting. This leaves angles greater than $40°$ subject to fitting error. This is evident in figure 4.9b, which shows larger residuals and a worse fit near $50°$.

The returned effective particle size and variance in table 4.3 do not deviate significantly from that of the parameterized phase function model, and only minor differences exist in the overall single scattering albedo, ω_0. We are more interested in the fit at smaller

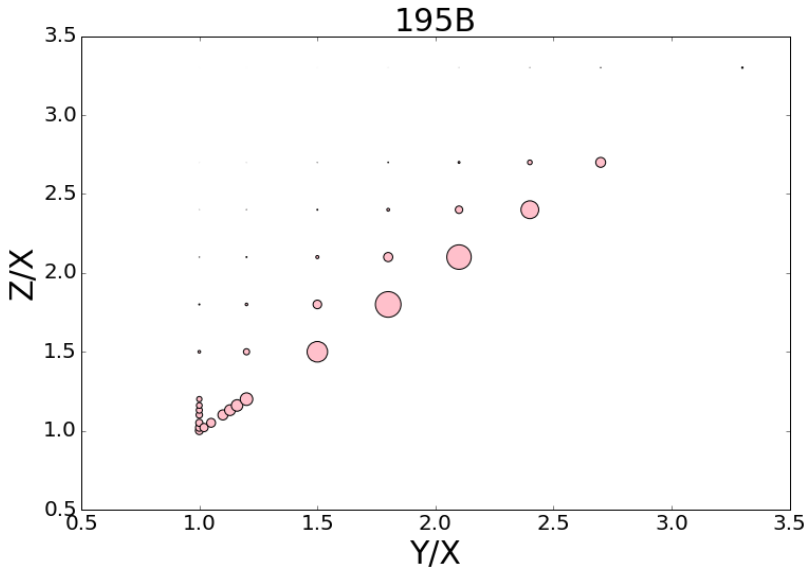

Figure 4.8: Relative weighting results for sol 81 survey 195B returned shape distribution where size represents normalized weight value

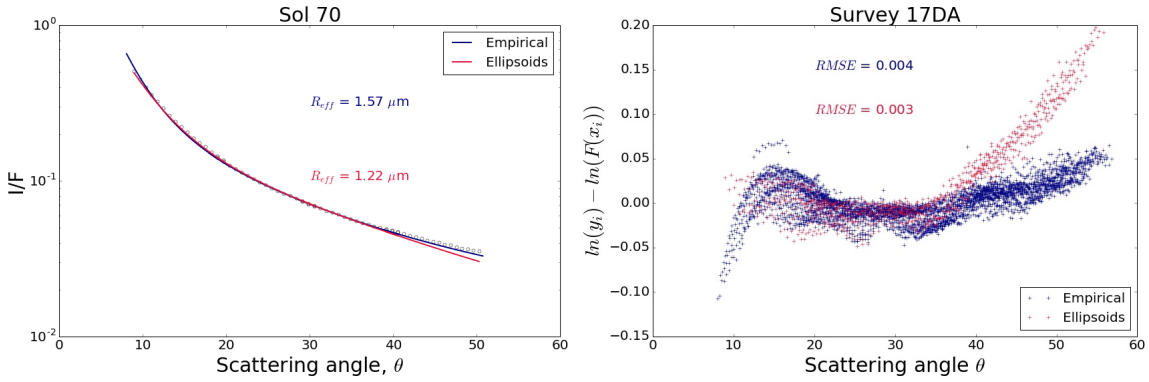

(a) (b)

Figure 4.9: Survey 17DA filter R8 (a) I/F results and (b) natural log deviation

scattering, where observations are more sensitive. The results are a tradeoff in accuracy towards larger scattering angles where observations are less sensitive.

The weights in figure 4.10 also show a distinct departure from the returned shape

Model	R_{eff} [μm]	v_{eff}	χ^2_v	ω_0	RMS
Parameterized	1.57	0.27	3.96	0.96	0.004
Ellipsoidal	1.22	0.34	32.7	0.98	0.003

Table 4.3: Returned parameter results for 17DA using two different models for phase function.

distribution, where aspect ratios tend towards 1.0. We cannot know what the observations would look like past 50° where the brightness is highly dependent on shape and so results weighted towards smaller aspect ratios are likely not realistic for this time and observation.

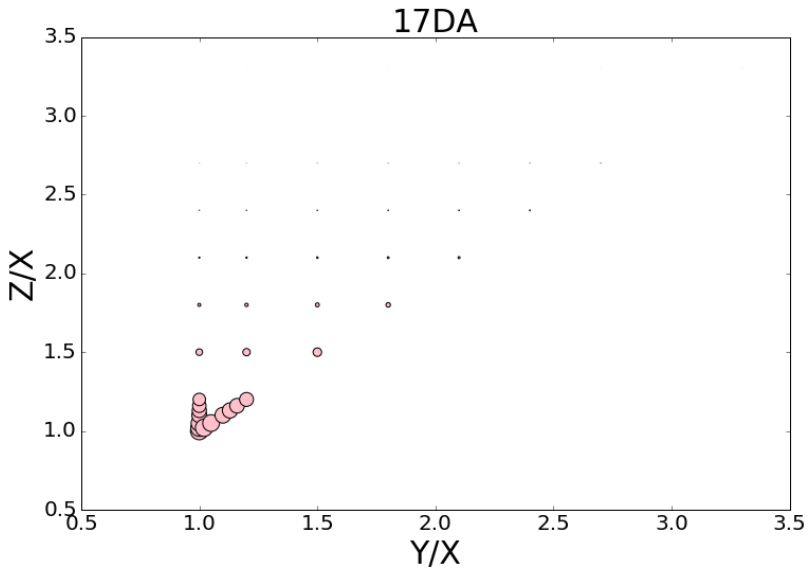

Figure 4.10: Results for sol 70 survey 17DA returned shape distribution.

4.2.4 Particle properties

Figures in this section show total mission results from returned fits allowing shape distribution parameters to vary. Values are plotted against those from the previous section

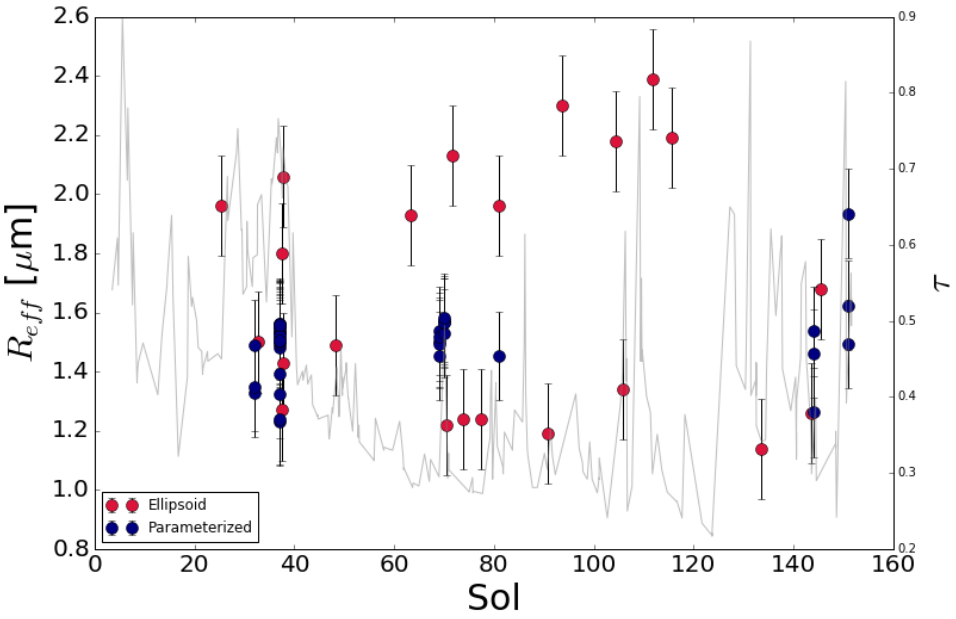

Figure 4.11: All particle sizes returned from fitting for the parameterized model (navy) and the ellipsoidal model (red)

and against optical depth over the entire mission where necessary. For most of the mission, there is little deviation from the 1.5μm initial fitting value, with all ellipsoid values falling within a 10% range of both the returned values for the parameterized phase function and the other ellipsoid model values.

Effective particle size for a gamma distribution in figure 4.11 are more variable than their counterpart parameterized results. The error bars used in this figure represent a 10% fractional error value of the mean of all results. For the most part, the error bars for the parameterized and ellipsoidal effective particle size results overlap. Where there are no parameterized results for comparison, ellipsoidal results tend to vary more. These results are fits to surveys recorded during times of higher ice variability. More surveys were processed for this work compared to those used in the previous section. Sols 30 through 40 and sols 140 - 150 show agreement within assumed 10% error between both models.

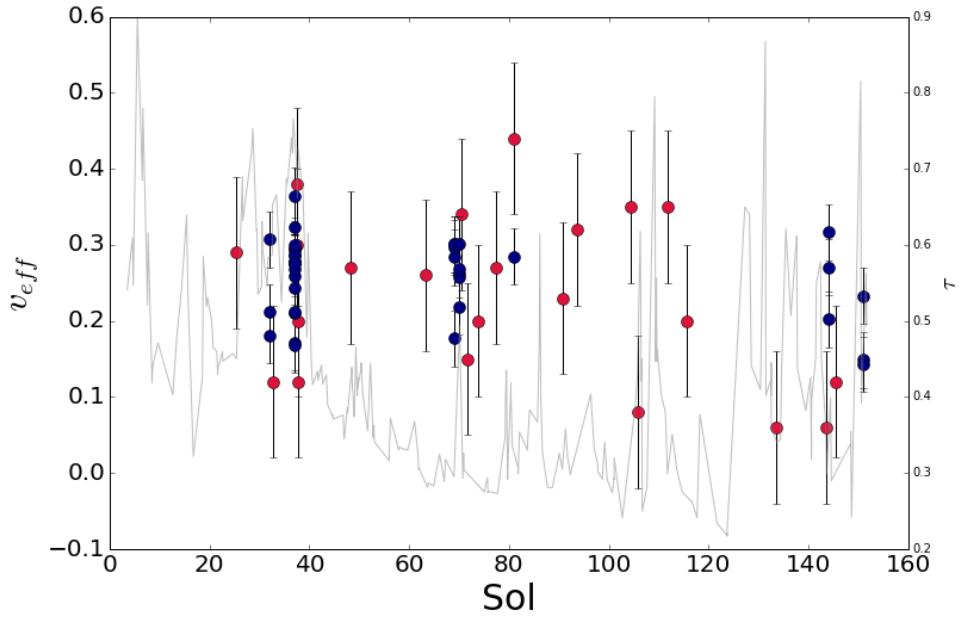

Figure 4.12: All particle variances returned from fitting for the parameterized model (navy) and the ellipsoidal model (red)

Large changes in returned effective particle size occur mid-mission for sols 80 through 120, where values increase to > 2 μm.

The variance shown in figure 4.12 also behaves in a similar way to the particle size, which is at first glance an improvement over the parameterized model. As the particle size increases for sols 80 - 120, the variance also increases. Under the assumption that this increase is real, we would then see a larger range of particles and a shift towards larger particles. The returned optical depth in figure 4.13 does not significantly deviate from a range of $\pm 30\%$ of the initial value.

We plot the resulting volumetrically calculated single scattering albedo in figure 4.14 to show the linear trend with returned effective particle size. The values are within a range of 0.96 to 0.98. The volumetric single scattering albedo is dependent within the model on the distribution of particles and therefore the effective particle size and variance for

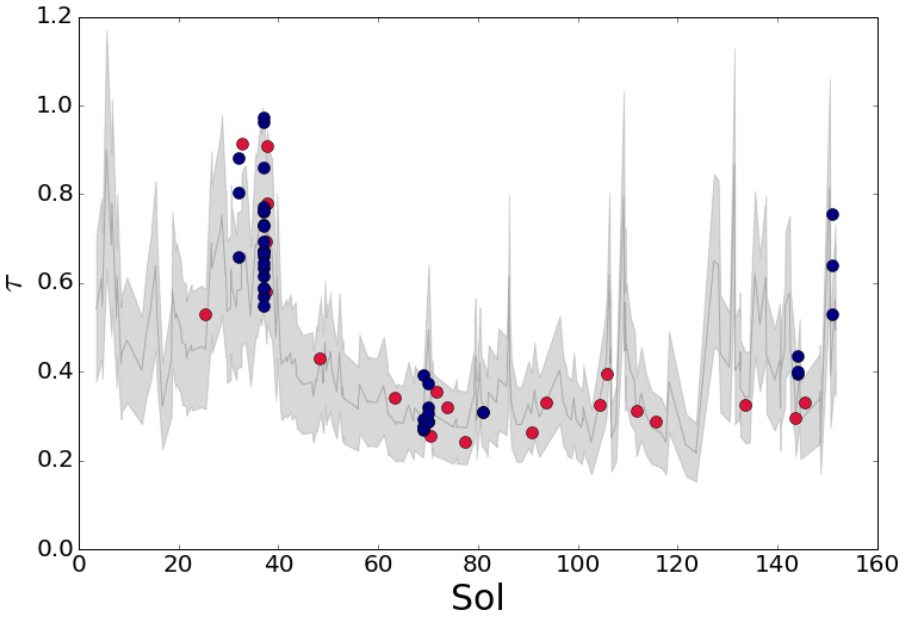

Figure 4.13: All optical depth returned from fitting for the parameterized model (navy) and the ellipsoidal model (red)

a gamma distribution. This is consistent with Wolff et al. (2009). The average of those results is represented by the dashed grey line.

The shape parameters returned from the model are binned in figures 4.15a for μ and 4.15b for σ. There is a very obvious pattern in the returned values for μ_x and μ_y, where μ_x tends towards higher values while μ_y tends towards 0. Values for σ_x and σ_y remain largely centered about 1.0.

4.2.5 Uncertainty

We compare a triaxial ellipsoid phase function to a parameterized phase function using an F-test comparison calculation (equation 2.21). As expected based on how the fits look, sol 32 shows an improvement over the parameterized model. For 195B and 17DA, the fits do not improve on the existing model. For surveys shown in table 4.4, fitting to those with

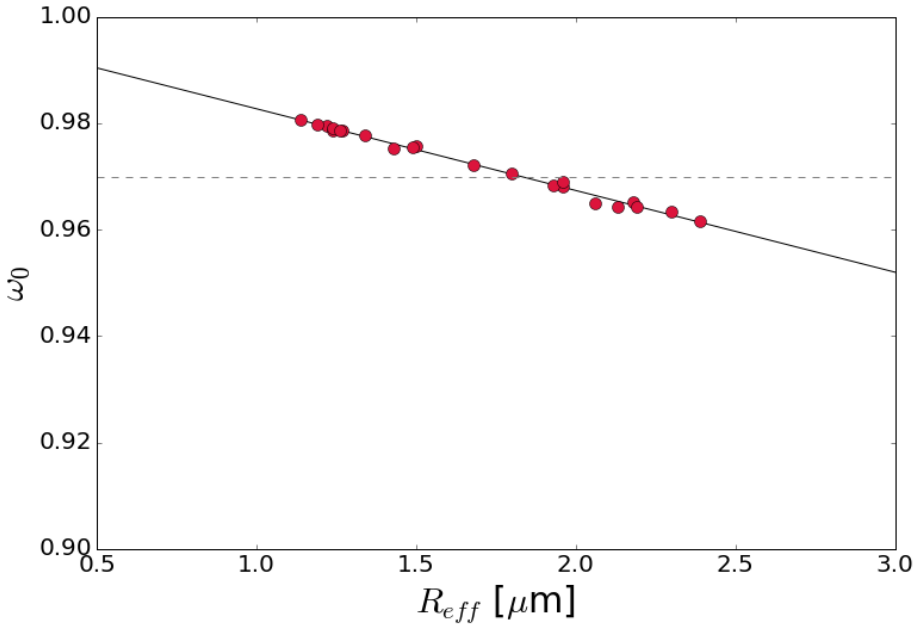

Figure 4.14: Singe scattering albedo returned from fitting.

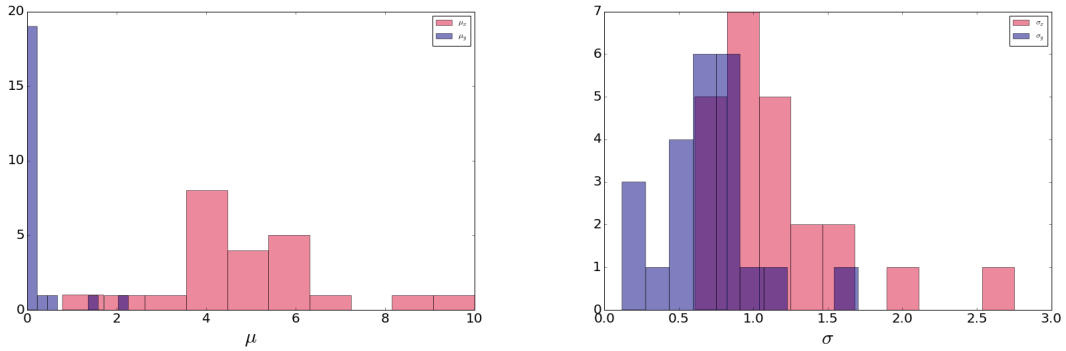

(a) (b)

Figure 4.15: Shape distribution parameters for (a) μ_x (red) and μ_y (navy) and (b) σ_x (red) and σ_y (navy)

limited scattering angle range is less effective when using the ellipsoidal model than for those with higher scattering angle range.

Survey	sol	τ	F	θ_{max} [deg]
13AE	32	0.91	5.61	143.41
195B	81	0.31	0.85	143.69
17DA	70	0.26	-0.14	55.8
17CC	69	0.0	-0.02	53.51
141E	37	0.69	0.001	50.52
1421	37	0.58	-0.04	50.3
1424	37	0.78	-0.11	58.41
1427	37	0.91	1.22	64.65

Table 4.4: F-test results performed for all matching surveys.

We perform the same tests as that of section 3 where the percent change in I/F is calculated for a change in R_{eff}. Figures 4.16 and 4.17. For all surveys tested, the maximum difference in R_{eff} for a 10% change in I/F is 0.15, on par with a 10% uncertainty in R_{eff}. For values returned in the previous section, we don't see a correlation with optical depth. If these values don't change with optical depth, then we can assume they don't really vary with time. We calculated the mean of 1.54 ± 0.15 μm with a standard error of 0.01. If we say that the returned particle size values using the ellipsoid model show similarity to those using the parameterized value, then we also expect (and see) no correlation with optical depth so that the mean value calculated from the entire population is 1.68 ± 0.41 μm with a standard error of 0.02.

We perform a t-test to check whether these means are significantly different. The p-value calculated for these two sample populations is 0.33 meaning we can't reject the hypothesis that these populations are the same. For this reason, we can say that even though there are higher values returned using the ellipsoidal phase function model, they are not outside the range of what is expected.

We also show in figures 4.16 and 4.17 the same RMS and χ^2_v variation with particle size for survey 13AE. The best fit value (red star) is at a minimum for RMS and χ^2_v. This

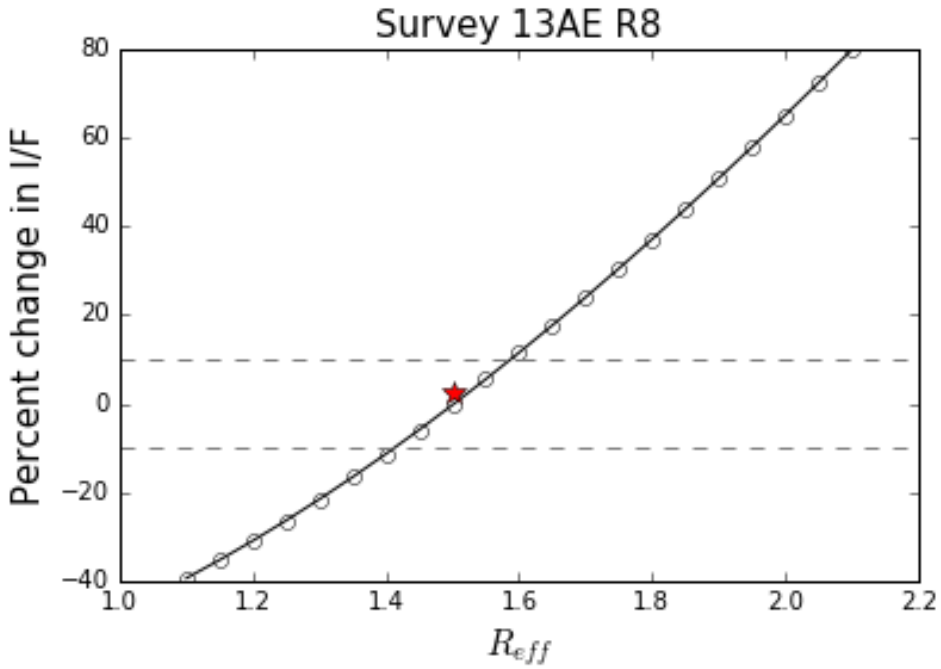

Figure 4.16: Percent change in modeled I/F for a change in particle size, where the star represents the best fit effective particle size

value is particularly close to the minimum, but in general values are within 10% of where the minimum occurs for all surveys.

4.3 Summary

We present results for effective particle size, variance, and shape distribution parameters using an ellipsoidal shape database to construct the single scattering phase function. We have compared these results to those using a parameterized phase function (Tomasko et al. 1999, Pollack et al. 1995).

The returned fits using the ellipsoidal model are good, especially when comparing higher scattering angles. There is an improvement in this range, and returned effective particle size is generally within the range of 1.68 $\pm$ 0.41 μm. This is not significantly different from the values obtained in the previous section.

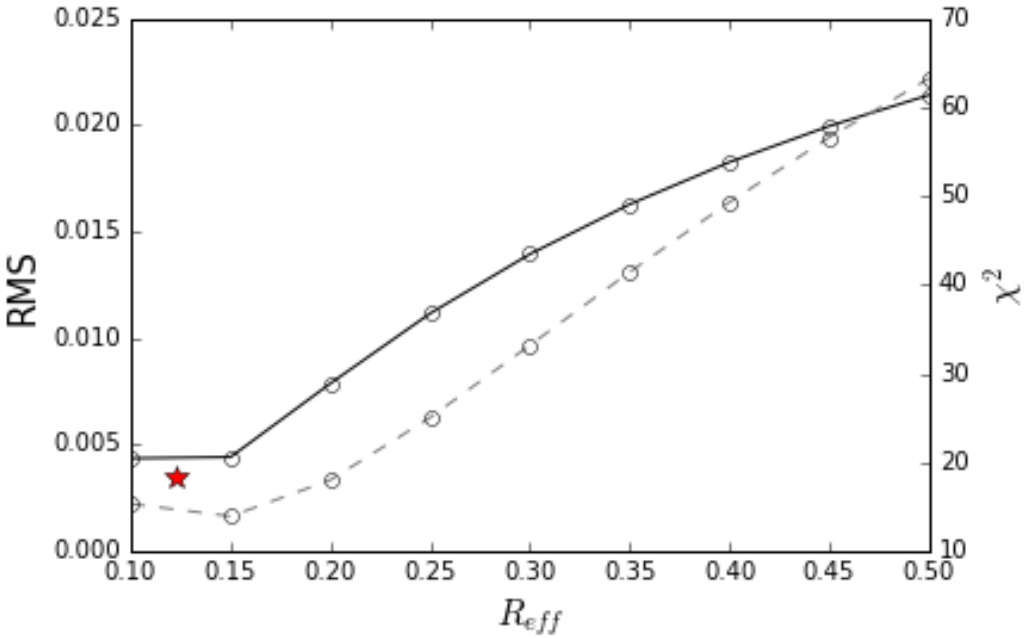

Figure 4.17: The returned RMSE relative to observations for a change in particle size, where the star represents the best fit effective particle size

To fit shape with precision, data must be obtained at higher scattering angles. For every comparison using the mini-azimuthal surveys with only 4 images ranging up to $\sim 60^{\circ}$, the parameterized performed better. That being said, the effective particle sizes returned from the fits are similar in value.

Fits are highly dependent on initial parameters, and so it pays to figure those out ahead of time by looking for a minimum. Optical depth and particle size are not correlated using either model, and the volumetric single scattering albedo varies linearly with effective particle size. The major benefit to using this assumed shape is that the database exists not only for the visible wavelength regime but also across a wide range of size parameters. Several parameters needed to calculate the parameterized phase function including θ_{min} and the imaginary index of refraction are not readily available for wavelengths outside the visible. Within the first 10° scattering angle, the shape model performs well.

5. PARTICLE SIZE USING PANORAMIC CAMERA SKY BRIGHTNESS SURVEYS

5.1 Introduction

The Mars Exploration Rovers, MERA (Spirit) and MERB (Opportunity) landed in Gusev crater (14.5 °S 175.5°E) and Meridiani Planum (1.92°S, 354.5°E), respectively, in January of 2004. The mission has spanned over 5000 sols, and the data collected from each rover represents the longest running source of ground-based observations available for Mars (Lemmon et al. 2015). Spirit has since completed its mission and is no longer opperational, but both Spirit and Opportunity were operational during the 2007 planet encircling dust storm. In the investigation for particle physical properties, such a dust loading event is an excellent opportunity to study particle size during high dust loading events such as this (Smith et al. 2006).

In section 4, we assumed a shape and tested its applicability in a phase function model to determine particle size. With the available sky survey datasets, this same model will be applied in conjunction with the parameterized model to determine whether or not there is a seasonal dependence in particle size. Instead of assuming shape as a parameter or employing the empirical phase function fitting approach of section 3, the methodology in this section makes no assumptions about the shape of the phase function.

The goal of this section is to determine with new methodology the seasonal change in phase function, which in turn leads to the change in particle size. That is to say, if the phase function changes with season, this could be a result of changing dust aerosol size distribution, and specifically effective particle size. We first discuss the new data set and corrections to image pointing. We then present phase function and particle size results for both phase function models and assess the seasonal dependence of particle size.

5.2 Data

The Panoramic Camera (Pancam) (Maki et al. 1999) onboard each rover is capable of multispectral observations, similar to those of Imager for Mars Pathfinder (Tomasko et al. 1999) and the SSI on the Phoenix lander. Pancam's filters comprise 12 bands from 0.4 to 1.0 um for stereoscopic imaging with 0.28 mrad IFOV. Of interest to this work are the L8, R8, L2, and R2 filters. The former are used for direct sun imaging at 440nm (L8) and 880nm (R8). The L2 and R2 (both 754 nm) filters are used to capture sky surveys similar to those described in section 3.

MER sky surveys are available through the PDS image atlas. Files include radiometrically calibrated radiance data (RAD or RAT files) and supporting ancillary information (EDN or ETH files). Surveys contain 4 to 9 images sequentially taken at varying azimuth angles away from the sun. For a given observation, images vary between 64° x 64° thumbnails (RAT) to 128° x 128° (RAD). MERA (Spirit) and MERB (Opportunity) observations used in this study are limited to low-sun elevation surveys that allow for constraints on scattering properties (sequence P2618) and thumbnail images, which are more frequently available farther into the mission . Data are further filtered by wavelengths, where only R2 and L2 filters are used (754 nm) for consistency with previous sections.

Low-sky sun surveys using the L2 and R2 filters are available throughout the mission, but we further limit the data up sol 1250 (figure 5.1). After this sol, enough dust covered the optics to significantly affect imaging. Calibration after this date requires solving for the amount of dust on the optics, which is not linear and can increase with dust loading or decrease with heavy wind events. Data past this point are excluded from this work. Surveys up to sol 1250 capture the onset of the 2007 global dust storm, which still presents an interesting test for our model. As a final check, we also exclude images with gaps in angular coverage.

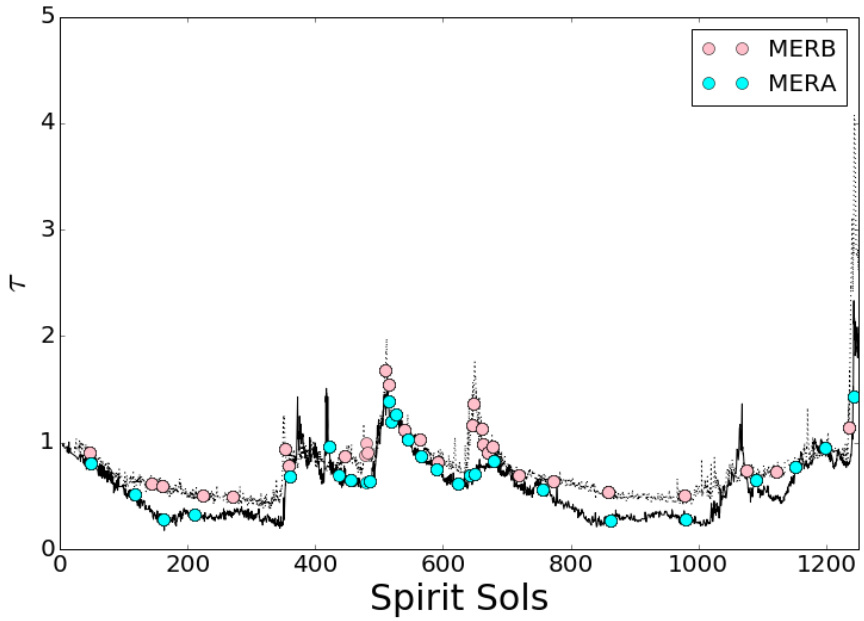

Figure 5.1: Available L2 and R2 surveys used in this work for MERA (cyan) and MERB (pink). The surveys are plotted against MERA (solid) and MERB (dotted) total column extinction

5.2.1 Radiometric calibration and processing

All images were calibrated pre-flight and in-flight according to Bell III et al. (2003) and Bell III et al. (2006) before download. We processed surveys further by determining site information and rover pointing. Unlike the Phoenix lander, both MER rovers were designed to traverse creating an additional frame to rotate each image. Observations on the rover are taken relative to the Pancam frame of reference, which is attached at the center of the instrument. This differs from the rover frame, which has its origin at the rover center (Li et al. 2004). In addition, a site frame is defined for each location where the rover has taken observations. Pointing within the Pancam frame has been recorded for each image relative to the rover frame, and a rotational quaternion has been calculated before telemetry via the onboard instrument clock (SCLK). The quaternion is used to quickly rotate from

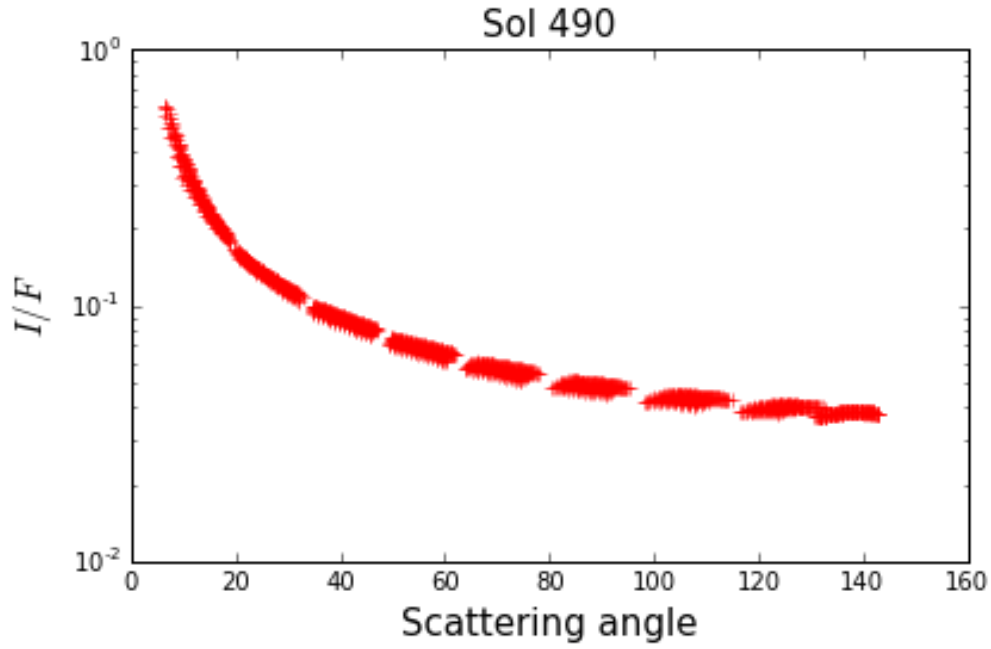

Figure 5.2: Reduced I/F using updated quaternion from MERB (Opportunity) sol 490 in $Wm^{-2}nm^{-1}sr^{-1}$

the camera frame to the site frame.

Images downloaded from the PDS are formatted using the PDS node labeling system. The labels for each image contain the images themselves and additional information such as a rotational quaternion, image transformation vectors, and time. Transformation from geometric space to image space is performed using the CAHVOR method described in Di & Li (2004) and Li et al. (2005). As a means of simplification, the CAHVOR image transformation is first rotated into a given site frame using a corrected quaternion vector, where the site is defined by a unique identification code that represents each new location to which the rover traverses. Following rotation and transformation, each image contained within the sky survey is located within image space.

Radiance values are converted to I/F in $Wm^{-2}nm^{-1}sr^{-1}$ using TOA irradiance at Mars distance, $I/F = radiance * R^2_{Mars}/1AU^2$/F'. Here, F' is the TOA flux multiplied

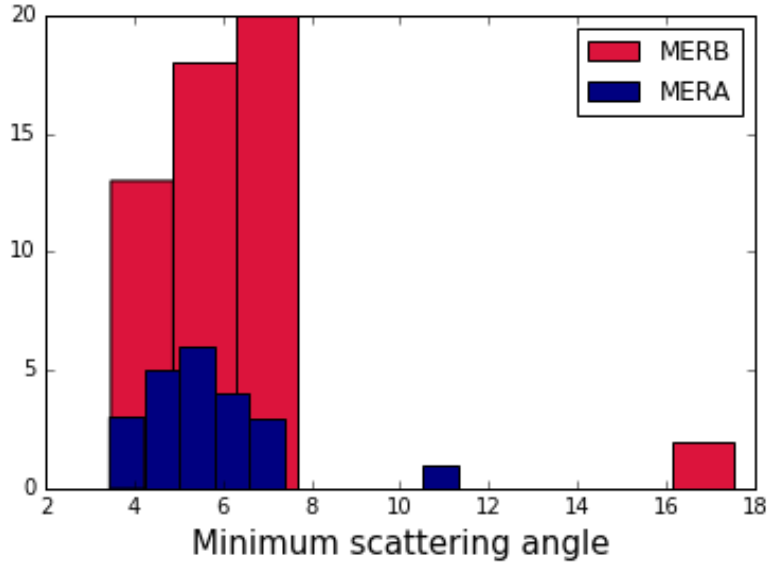

Figure 5.3: Histogram of minimum scattering angle imaged for MERA (Spirit) and MERB (Opportunity) surveys

by the filter response (Bell III et al. 2006). This filter response includes a scale factor, which is an estimate of the approximate reflectivity of the scene through each filter. The resulting I/F shown in figure 5.2, like that presented in sections 3 and 4, is sky brightness as a function of scattering angle from solar incidence. The breaks in the curve are a product of imaging, and the trend is a decrease in brightness away from the sun. For most MER images, brightness falls quickly within 20° relative to the sun, which is a region sensitive to particle size. A histogram of minimum scattering angle value is given in figure 5.3 to show how close the images get to the forward scattering angle. This is especially important to constrain particle size and forward scattering phase function peak.

5.2.2 Pointing corrections

Knowledge of time and tilt are used to control the search for the sun. If this fails, the entire hemisphere is searched (Li et al. 2004). A sun gaze mode is used to obtain a finer

estimate for HGA pointing where Pancam sits still and watches the sun move across the sky for a period of about 15 minutes. The resulting arc produces adequate refinements. These refinements are downlinked as a rotational quaternion.

The quaternion calculation onboard MER is incorrect due to an offset in the onboard SCLK, which processes rotations. The rotational quaternion for each site was calculated using a 'sun gazing' technique (Li et al. 2004) wherein Pancam would image the sun over 15 minutes to allow for location of the solar arc within the image plane. Due to an offset of the SCLK, the quaternion returned and uploaded into the EDR datasets contains errors, which produces an error in the image pointing through calculation of the rotational quaternion.

To correct for this error, a new quaternion is calculated using instead Pancam optical depth images post telemetry and RDR processing. For an optical depth observation, multiple solar images are taken at different positions following the sun. As the sun moves in the sky, its path relative to the rover is traced out. Given the position of Pancam relative to the rover and the sun relative to the site frame, the transformation from the rover to site frame is determined through least-squares fitting. This new quaternion is then used to process P2618 sequences. Figure 5.4 represents a typical result of the corrections, however some surveys do require larger corrections. We apply these corrections unanimously to all surveys used in this study.

5.3 Methodology

For this work, we determine the phase function from I/F fits to the data. Instead of returning particle size distribution information, the fitting algorithm returns tabulated phase function values directly without needing to know particle property information. The resulting phase function is then used diagnostically to look at seasonal change and subsequently fit to a phase function model to determine particle size.

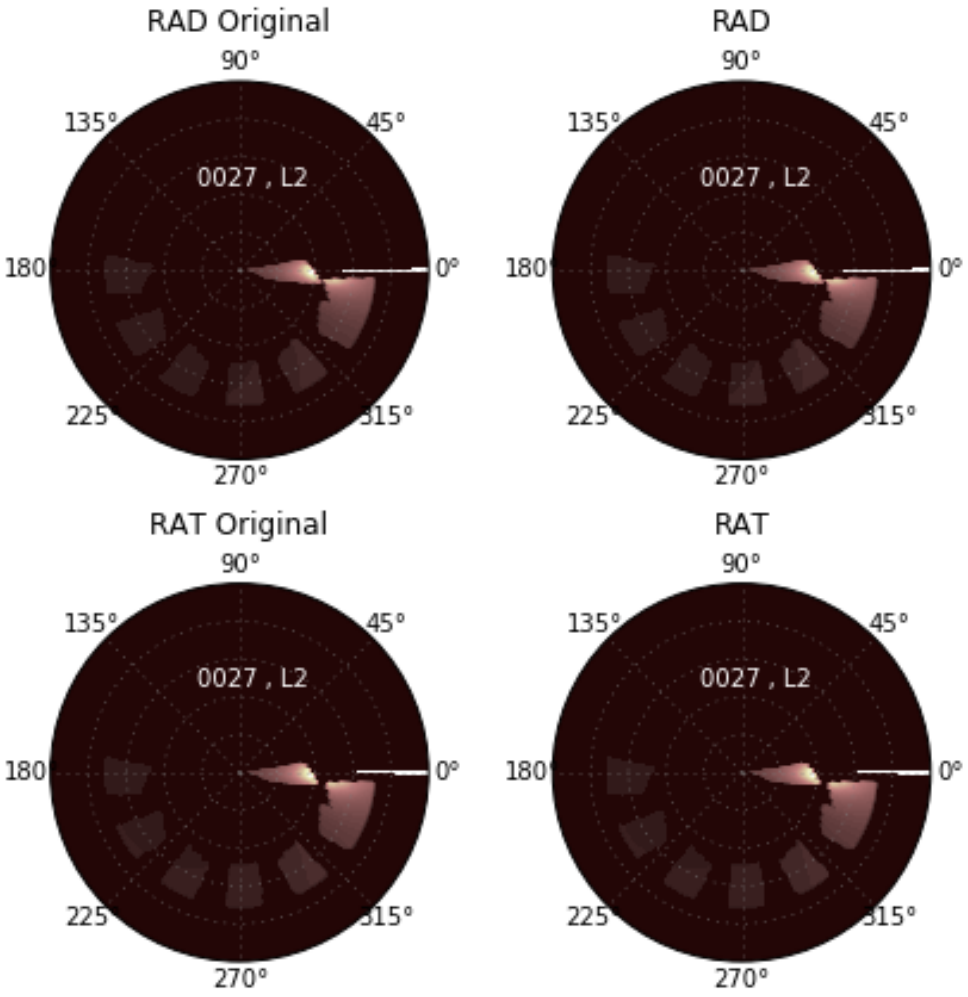

Figure 5.4: Processed sky survey using updated quaternion

5.3.1 Model fit

The fit is similar to that in previous sections where MPFIT (Markwardt 2009) minimizes the weighted deviates between the model and the data (equation 2.17). The fitting data are the I/F sky brightness values and the model is the semi-hemispherical sky radiance produced from DISORT. The inputs to DISORT include the Pancam 880nm optical depth, τ_{880}, single scattering albedo, ω_0, surface albedo, G_r, and solar incidence angle, μ_0.

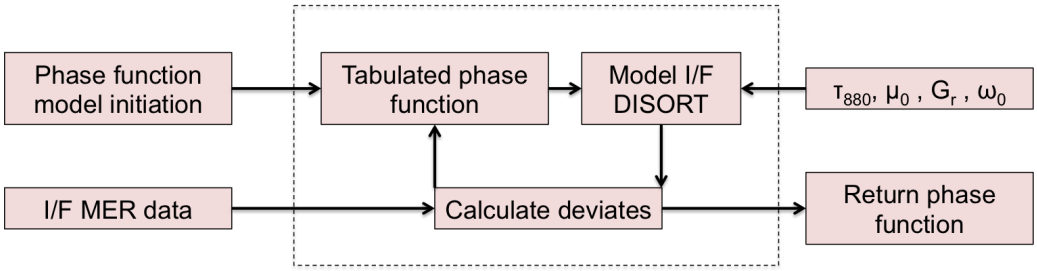

Figure 5.5: Architecture of fitting algorithm for tabulated phase function inversion, where the dashed square represents the iterative process within MPFIT before returning the desired parameters

The architecture of the fitting algorithm is shown in figure 5.5, where the dotted line represents the iterative nature of MPFIT. MER data is processed with the pointing correction and loaded into the program. A phase function based on either the parameterized model presented in section 3 or the ellipsoidal model presented in section 4. A tabulated phase function is calculated using a sample of scattering angles (i.e. $5°$, $10°$, $25°$, etc.).

The values at these angles are then used to reconstruct the phase function as input for DISORT. A semi-hemispherical radiance field is returned, and I/F is determined at the points of interest. MPFIT then iteratively varies the phase function inputs until convergence within the program is reached. The output is a new tabulated phase function without a priori knowledge of particle size distribution and shape. Further fitting for particle shape, size, and variance is then possible once a phase function is returned. This is outlined by figure 5.6, in which a phase function is again modeled using those described in previous sections.

In order to begin fitting, we provide the algorithm with an initial guess. We test both the parameterized phase function and ellipsoidal model to see if there is a difference in the returned result. Within the fitting algorithm, the data is masked according to angular constraints of the images. Most images capture scattering angles between $5° - 10°$ (figure

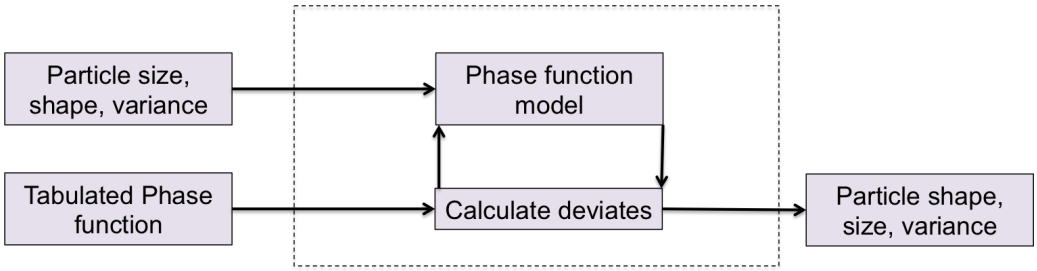

Figure 5.6: Subsequent fitting architecture to return particle shape, size, and variance, where he dashed square represents the iterative process within MPFIT before returning the desired parameters

5.3). Images do not cover low ($< 5°$) and high ($> 150°$) scattering angles to constrain the tabulated phase function during fitting. For this reason, when subsequently fitting for particle size, we use only returned modeled phase functions to tabulated phase functions where both the results using initial ellipsoidal and parameterized phase functions agree well. We take the lowest scattering value where both results agree and mask all phase function results greater than $120°$ where the tabulated results remain constrained. Fitting for particle size is done by averaging the results of both the ellipsoidal and parameterized phase function models to get a mean phase function for fittng. We present all results with color consistency for both initializations and returned particle size to look for systematic differences between the two models.

5.4 Results

We present results for diagnostic phase functions based on I/F fits as well as particle size fits based on those phase functions. MERA (Spirit) and MERB (Opportunity) results are shown in separate plots for clarity. We show individual fits for three sols to compare high and low optical depth (later and earlier sols) during the mission. These fits include sol 27 and 1215 for Opportunity and sol 49 for Spirit. For all sols we show results initialized with both the parameterized phase function and ellipsoidal phase function models.

5.4.1 Tabulated phase function: Opportunity

The most noticeable feature in figure 5.7a for sol 27 is the sharp decline past 160° scattering angle. This is expected because there are no data points past this angle to constrain the back end of the curve. Similarly, there is a difference in the magnitude of the forward scattering peak (small scattering angles). Again, no image covers this scattering range. The minimum scattering angle observed for sol 27 is 4.5°. For sol 27, we are confident that the range of $6^\circ - 120^\circ$ is constrained. The constrained area in fitting is marked by the filled grey area in figure 5.7a. Fitting at boundaries where one side of a data point is constrained and the other is not can produce poorly fit results. For the forward scattering angles, we select the minimum angle available plus 1° and round up. For all surveys that extend past 120° coverage we use a standard 120° where we are fairly sure that the two models agree. For surveys that do not extend past this value, we apply the same structure as the forward scattering peak.

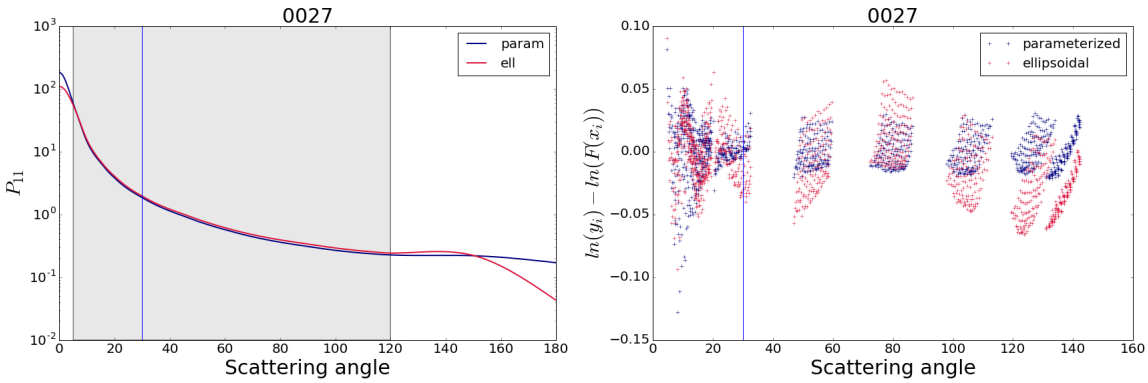

(a) (b)

Figure 5.7: Returned (a) tabulated phase function and (b) residual results from MPFIT inversion for MERB sol 27 using the parameterized phase function model (navy) and ellipsoidal model (red) to initialize the fitting procedure

The results returned for ellipsoidal and parameterized phase function models are highly similar with only minor differences between the two curves outside of scattering angles less than 6° and greater than 120°. The residual error, shown in figure 5.7b, is the natural log difference in modeled I/F from that of the reduced sky survey, and this shows good agreement in the fit for each phase function.

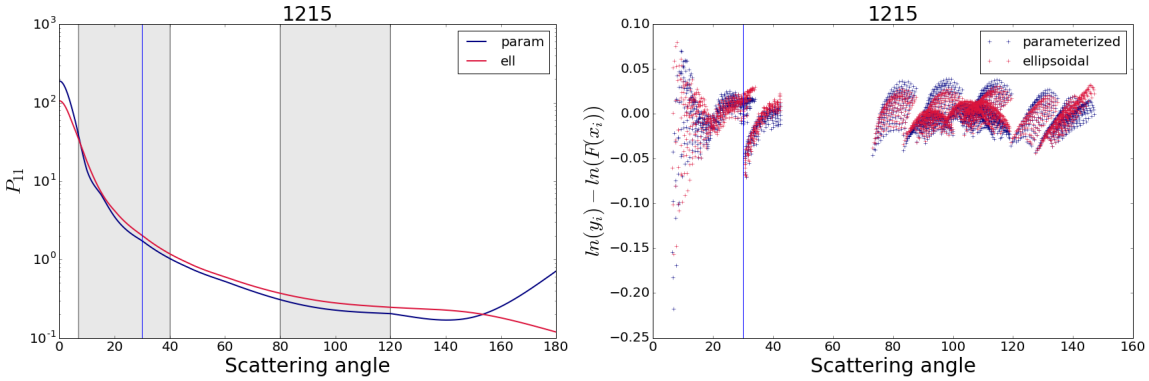

(a) (b)

Figure 5.8: Returned (a) tabulated phase function and (b) residual results from MPFIT inversion for MERB sol 1215 using the parameterized phase function model (navy) and ellipsoidal model (red) to initialize the fitting procedure

We also show in figure 5.8a results for MERB sol 1215, which is an observation taken during the onset of the 2007 global dust storm. The resulting tabulated phase functions are similar to those for sol 27 but have less pronounced dips at large scattering angles. The featureless curvature at middle scattering angles is consistent with irregular particle shapes, and the overall shape of the forward peak does not differ from that of sol 27.

For sol 1215, there is a lapse in coverage between scattering angles $\sim 50^\circ$ and 70°, which leaves this section unconstrained. The phase functions, however, still show remarkable agreement and reasonable shapes despite having no data otherwise. For further fitting

based on these results, we mask the data not only at higher and lower scattering angles (less than $8°$ and greater than $120°$) but also at mid-range angles ($40°$ - $80°$).

5.4.2 Seasonal changes in phase function: Opportunity

We assess the results for changes in logarithmic slope at $30°$,$dlnP/d\theta$, and phase function value at $120°$. In figure 5.9a, the slope become less negative through sols 400 - 600, during high optical depth season (shown by the black curve). The double peak in optical depth corresponds mildly to a double peak in $dlnP/d\theta$. The change in this slope with solar longitude, L_s, in figure 5.9b are lower during aphelion season and higher during perihelion. The sinusoidal curve is a fit to each data set. This curve is distinct and almost indistinguishable between ellipsoid and parameterized models.

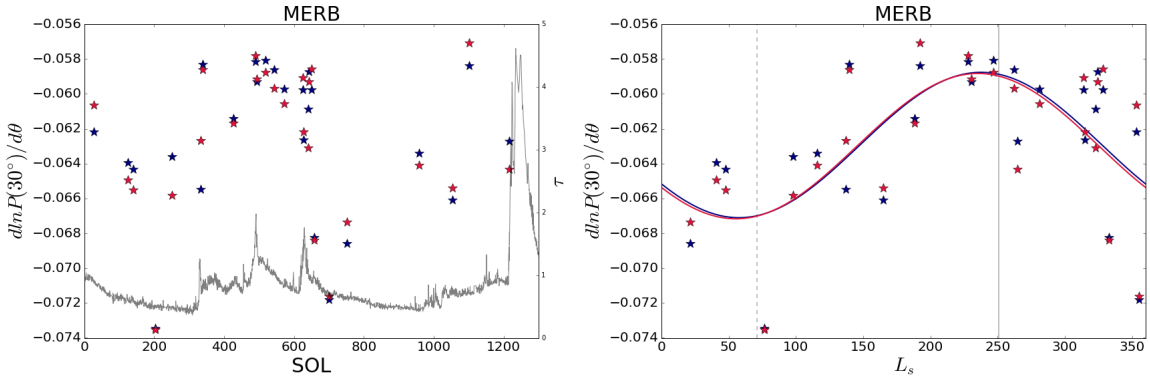

(a) (b)

Figure 5.9: Diagnostic forward scattering peak slope results vs. (a) sol and (b) L_s from MPFIT inversion for MERB using the parameterized phase function model (navy) and ellipsoidal model (red) to initialize the fitting procedure

Changes in particle size effect the forward scattering peak of the phase function. For larger particles, this peak is much more pronounced, which leads to a larger slope (more negative) with increasing scattering angle. This relationship is also true of optical depth

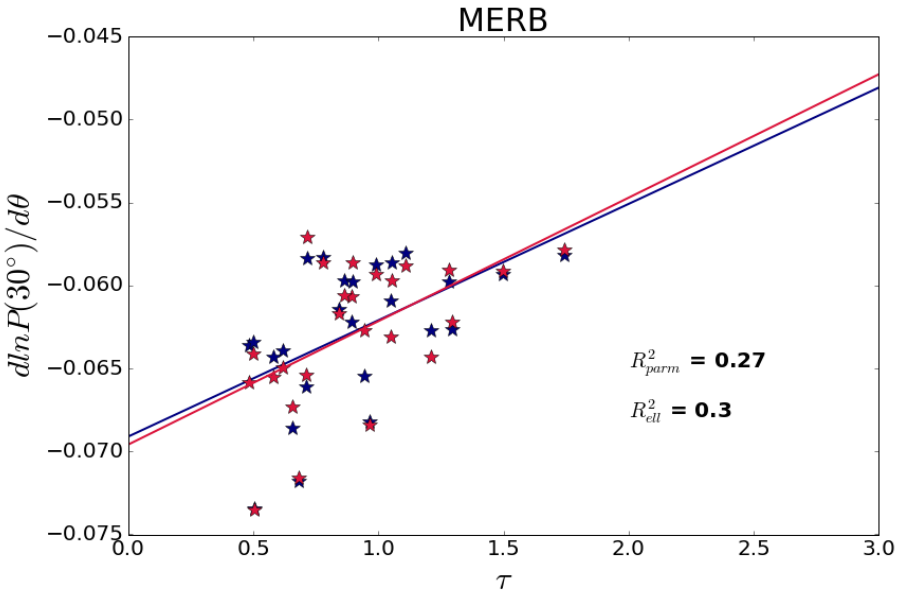

Figure 5.10: Forward scattering peak slope results from MPFIT inversion for MERB as a function of optical depth using the parameterized phase function model (navy) and ellipsoidal model (red) to initialize the fitting procedure. The R^2 value is provided in the plot for reference.

and particle size, which is why we see a positive correlation in figure 5.10.

We present slope results in conjunction figure 5.11a, which shows the value of the phase function at 120°. The backscatter value of the phase function responds accordingly with the slope where shallower slope values (less negative) correspond to higher backscatter values. The results in figure 5.11a show a decrease leading into sol 600 when the dusty season begins,corresponding with a decreased value in figure 5.9a for the same time period. In addition, the same double peak is present for sols 500 - 700, where dust activity is high. The backscatter value leading into the 2007 global dust storm (sol 1215) is not significantly different from the results in preceding sols.

Figure 5.11b shows the same trend for the results using an initial parameterized phase function and a much broader, less pronounced trend in the results using the initial ellipsoidal model. The curves in figure 5.11b do not match between the two models, but this

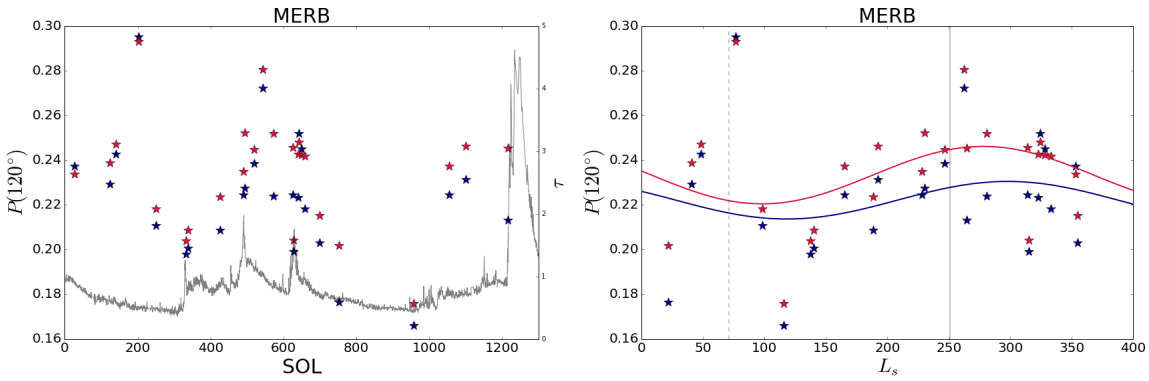

(a) (b)

Figure 5.11: Diagnostic back scatter results vs. (a) sol and (b) L_s from MPFIT inversion for MERB using the parameterized phase function model (navy) and ellipsoidal model (red) to initialize the fitting procedure

difference is likely from random variability and is not systematic. The backscatter value of any phase function is dependent on shape, and testing between an empirical model with an unconstrained backscatter shape and a physical model with a defined shape is likely the cause. Despite this, the two curves retain the same trend, with lower values near aphelion (gray dashed) and higher values near perihelion (grey solid) in figure 5.11b.

Unlike $dlnP/d\theta$, we see no correlation to optical depth. This is expected, as the higher scattering angles are largely affected by particle shape and composition and less by optical depth and particle size in figure 5.12. The calculated R^2 values are much lower than those calculated for the phase function slopes and the spread is value is high relative to the trend line.

5.4.3 Tabulated phase function: Spirit

Sol 49 for MERA in figure 5.13a shows similar results to MERB sol 27 but with an upward tilt past 140° scattering angle. This region is again unconstrained, and results past this point are masked for further fitting. We also see the disparity in the forward scattering

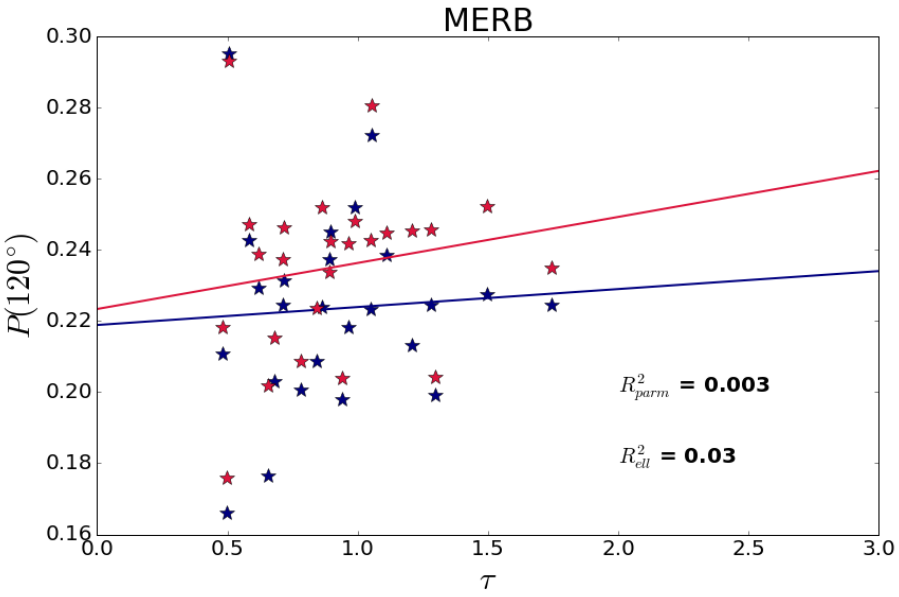

Figure 5.12: Backscatter results from MPFIT inversion for MERB as a function of optical depth using the parameterized phase function model (navy) and ellipsoidal model (red) to initialize the fitting procedure. Calculated R^2 values are given in plot.

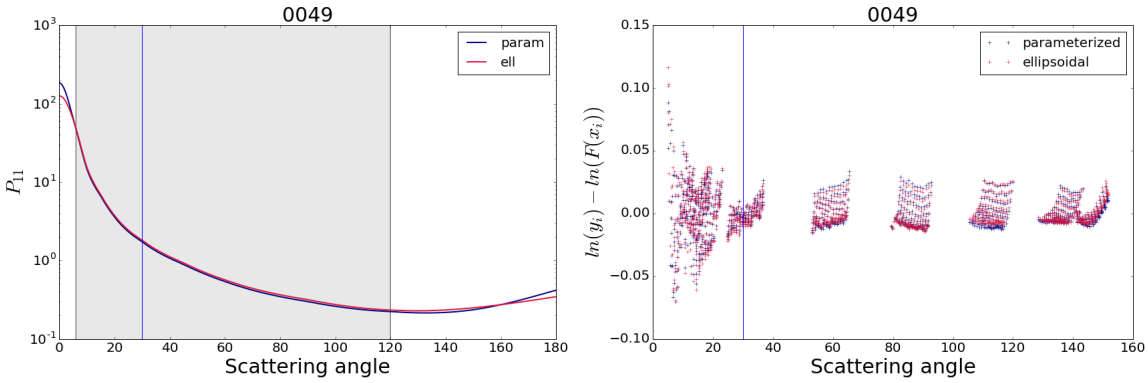

(a) (b)

Figure 5.13: Returned (a) tabulated phase function and (b) residual results from MPFIT inversion for MERB sol 49 using the parameterized phase function model (navy) and ellipsoidal model (red) to initialize the fitting procedure

peak between the two models, with the parameterized model having a more pronounced peak. This is due to the assumed surface area and volume equivalency difference between the parameterized and ellipsoidal phase function models.

5.4.4 Seasonal changes in phase function: Spirit

The resulting diagnostic $dnP/d\theta$ and $P(120^\circ)$ for Spirit are much more defined in figures 5.14a and 5.14a than the results for Opportunity rover. The double peak is visible for sols 500 - 700, and like Opportunity, it is delayed delayed from the dust activity near sol 400. The double peak corresponds well to a peak in optical depth near sol 500 and a smaller peak near sol 700 with a steady increase leading up to these periods. Unlike the Opportunity rover, there is an increase in slope value near the onset of the 2007 dust storm ($\sim$ sol 1200). Surveys taken at the onset of the global dust storm were not analyzed due to large gaps in scattering angle coverage, which ultimately led to unconstrained results. We present in these figures up to sol 1152 for Spirit. The differences between the ellipsoidal model and the parameterized model are not apparent during this time, and no systematic trends in this difference are noticeable.

The seasonal pattern shown in figure 5.14b matches a sinusoidal curve, where values remain more closely centered on this curve than they do for Opportunity in figure 5.9b. The results are similar to those for Opportunity in that there is little difference between the sinusoidal fit for ellipsoidal and parameterized models. Figure 5.15 shows that the slope of the forward scattering peak is proportional to optical depth, but is much more tightly constrained to its linear fit. The R^2 values closely match for each curve and the differences are likely not significant.

The phase function value at 120° scattering angle for Spirit rover shows a double peak in figure 5.16a for sols 500 - 700 for both parameterized model and ellipsoidal model results. There is no decrease in this value on sol 1152, corresponding to a rise in $dnP/d\theta$

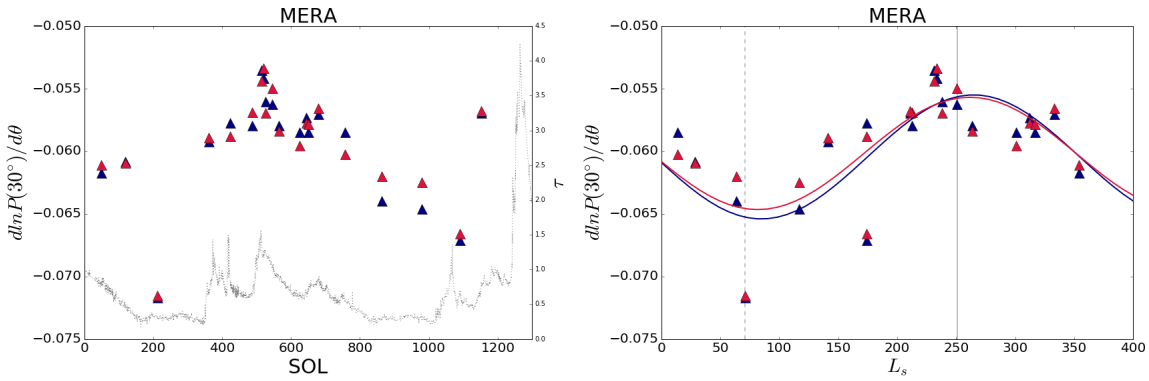

(a) (b)

Figure 5.14: Diagnostic forward scattering peak slope results vs. (a) sol and (b) L_s from MPFIT inversion for MERA using the parameterized phase function model (navy) and ellipsoidal model (red) to initialize the fitting procedure

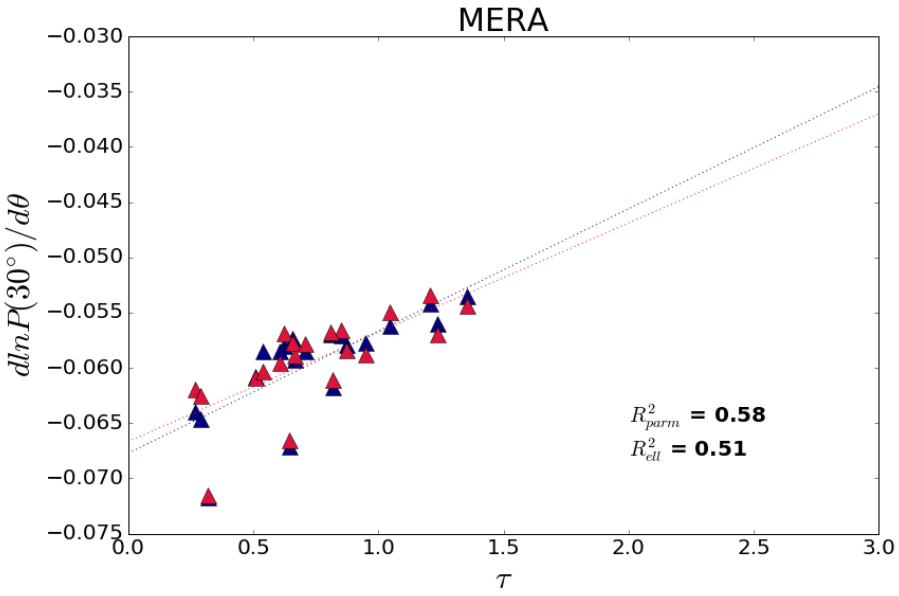

Figure 5.15: Forward scattering peak slope results from MPFIT inversion for MERA as a function of optical depth using the parameterized phase function model (navy) and ellipsoidal model (red) to initialize the fitting procedure.

in figure 5.14a. For these results, the ellipsoidal model tends to produce slightly higher values than the parameterized model. These differences are small, but are due to shape constraints using a physical model vs an empirical model.

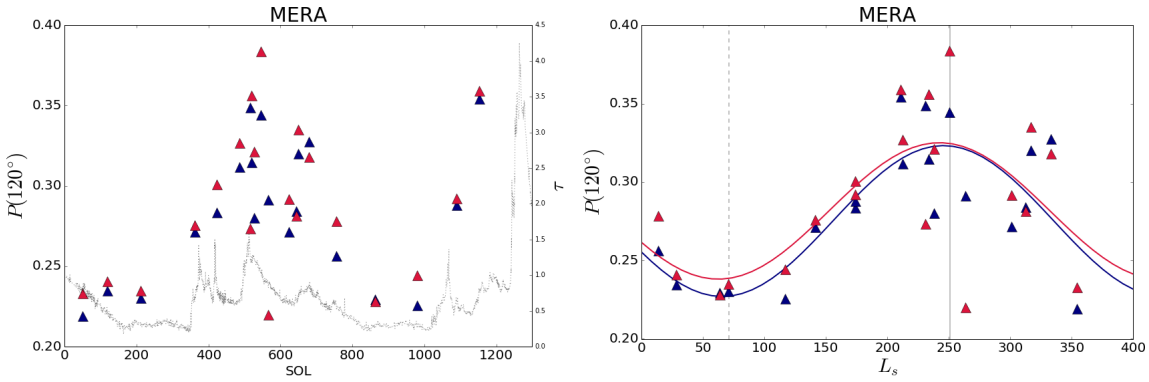

(a) (b)

Figure 5.16: Diagnostic back scatter results vs. (a) sol and (b) L_s from MPFIT inversion for MERA using the parameterized phase function model (navy) and ellipsoidal model (red) to initialize the fitting procedure

Seasonal trends in the middle panel of figure 5.16b follow the same pattern as Opportunity, where there is a dip near aphelion and a rise near perihelion. The sinusoidal fits are much more prominent than those for Opportunity. The curve fit to the ellipsoidal results is slightly higher than that of the parameterized curve, but this difference again is small.

In figure 5.17, there is a more linear trend with optical depth than for Opportunity. The results for Opportunity are noisier than for Spirit, where the spread in values for both $dlnP/d\theta$ and P_{120} is lower. The differences again are evident in the R^2 value, where ellipsoids have no significant trend and the value for the parameterized fit is better but not significant.

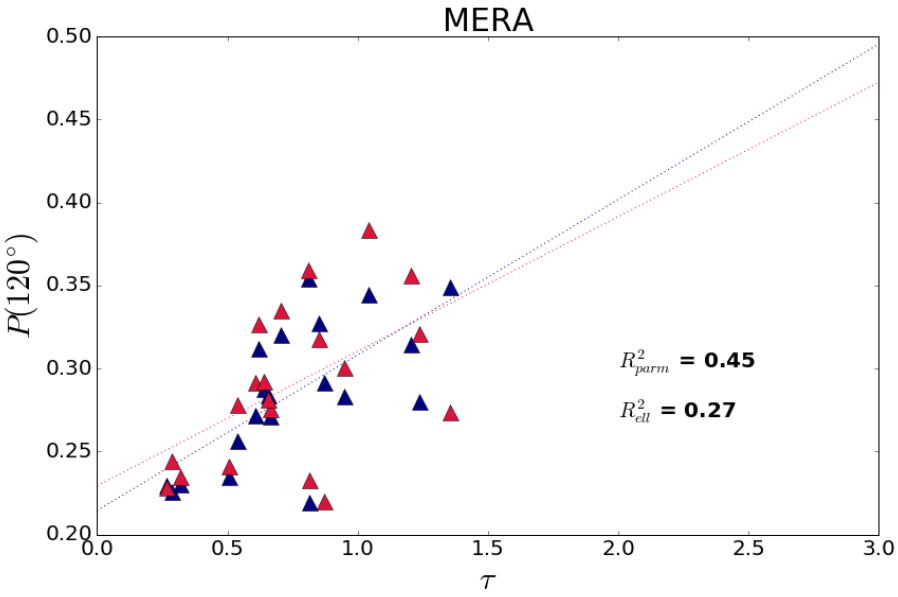

Figure 5.17: Backscatter results from MPFIT inversion for MERA as a function of optical depth using the parameterized phase function model (navy) and ellipsoidal model (red) to initialize the fitting procedure.

5.4.5 Fitting for particle information

Opportunity and Spirit show similar trends in season, with peaks in backscatter and shallower phase function slopes near perihelion. We are interested to see if particle size follows the same trends as the phase function. Using both the ellipsoidal phase function model and the parameterized phase function model, we fit the retrieved phase function using particle size and shape as free parameters. In the case of the parameterized model, we allowed the parameters outlined in section 3 to vary in order to accurately fit higher scattering angles. We present the same three sols as examples of typical results.

Sol 27 for Opportunity shows a well-constrained fit in figure 5.18a for both models between scattering angles of 10° and 60°. Past 120°, the fits get worse. This is expected due to our constraints. The forward scattering peak is expanded to show the differences in results. For sol 27, the parameterized model fits this forward scattering peak well, while

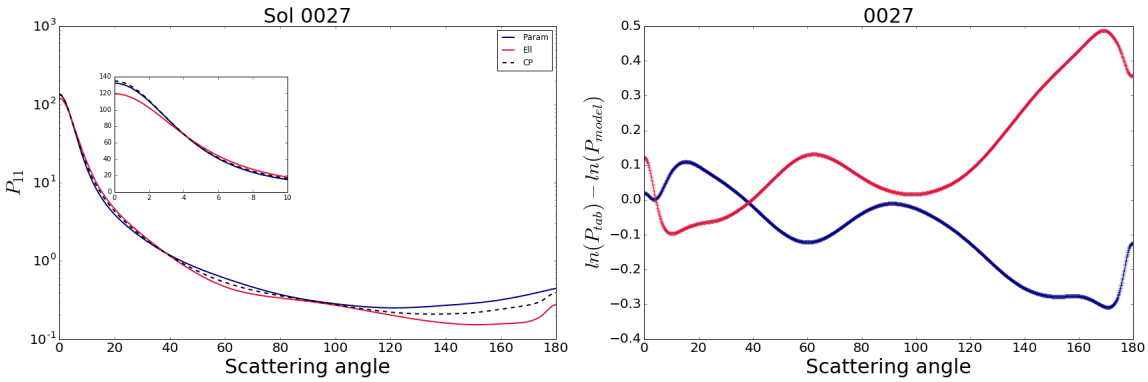

(a) (b)

Figure 5.18: Forward model (a) phase function results and (b) residual error for MERB sol 27 using the parameterized phase function model (navy) and ellipsoidal model (red) to initialize the fitting procedure

the ellipsoid model underestimates the peak. Within the constrained angles, the residuals in figure 5.18b are low.

Figure 5.19a and figure 5.20a show examples of consistency between models, but the fit in the forward scattering peak is consistently less than the tabulated phase function. This is also true for sol 49 for Spirit, where the forward scattering peak is consistent between models but both models underestimate the peak substantially. Variation occurs at higher scattering angles where shape is a more important factor.

Effective particle size using a gamma distribution is shown in figure 5.21a for Opportunity and figure 5.21b for Spirit. The particle sizes are not significantly different between models for either spirit or Opportunity. Even for sol 27, where the forward scattering peak for the parameterized model performed better, we don't see a significant difference in returned particle size. For Spirit, particle size is incredibly consistent throughout the entire mission. It is also interesting to note that there is no large increase in particle size at the onset of the global dust storm.

Seasonal trends for Spirit follow the diagnostics of the phase function, where there is

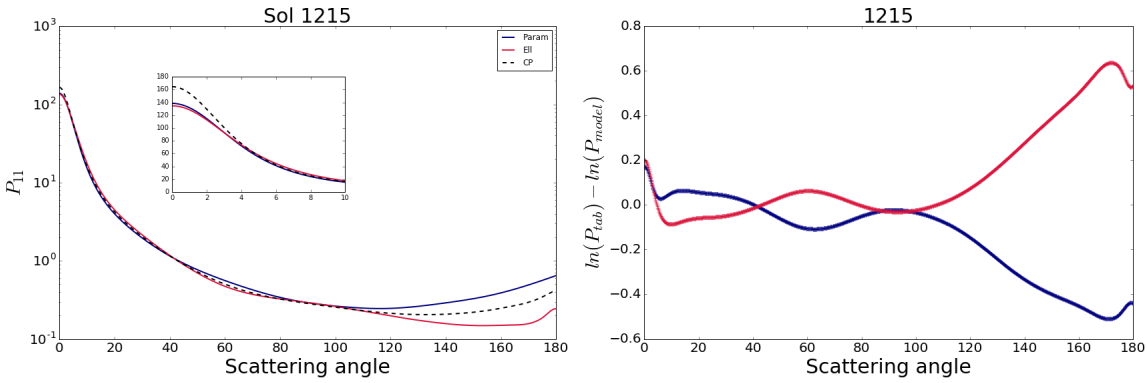

(a) (b)

Figure 5.19: Forward model (a) phase function results and (b) residual error for MERB sol 1215 using the parameterized phase function model (navy) and ellipsoidal model (red) to initialize the fitting procedure

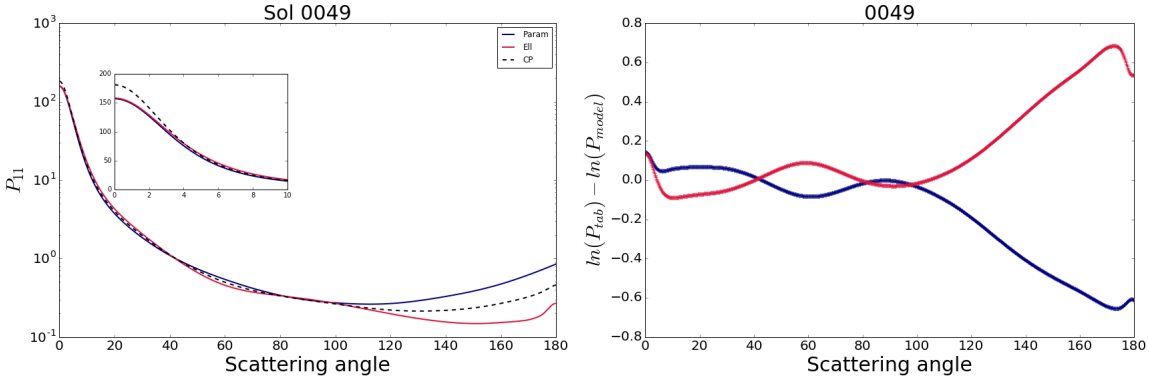

(a) (b)

Figure 5.20: Forward model (a) phase function results and (b) residual error for MERB sol 49 using the parameterized phase function model (navy) and ellipsoidal model (red) to initialize the fitting procedure

a moderate increase in particle size near perihelion compared to aphelion. This trend is not visible in the Opportunity results. Figure 5.22b shows a consistent particle size with little seasonality and only minor dips in particle size visible in the results for Opportunity. The variability in Opportunity particle sizes at aphelion, which is not present for Spirit

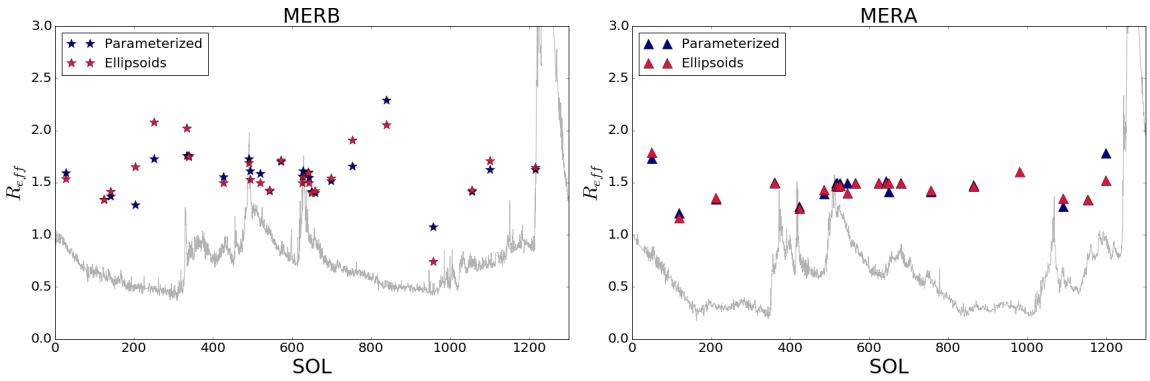

(a) (b)

Figure 5.21: Particle size results from MPFIT inversion for (a) MERB and (b) MERA using the parameterized phase function model (navy) and ellipsoidal model (red) to initialize the fitting procedure

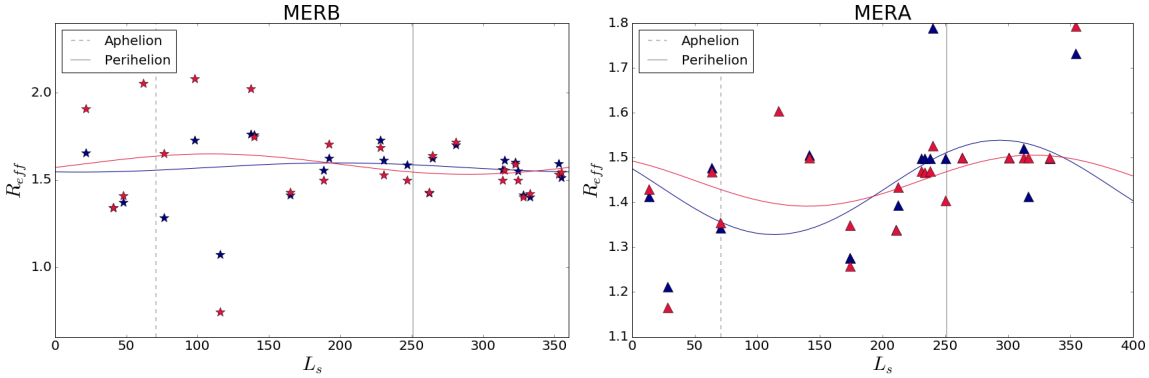

(a) (b)

Figure 5.22: Particle size results from MPFIT inversion for (a) MERB and (b) MERA as a function of solar longitude using the parameterized phase function model (navy) and ellipsoidal model (red) to initialize the fitting procedure

results in figure 5.22b, might suggest that the results are diagnostic of ice and haze aerosols present at Opportunity locations that were not present at the Spirit sites (Lemmon et al. 2015). It is apparent for both Spirit and Opportunity that there is little correlation with optical depth, with only a minor trend seen using the parameterized model for Spirit. This

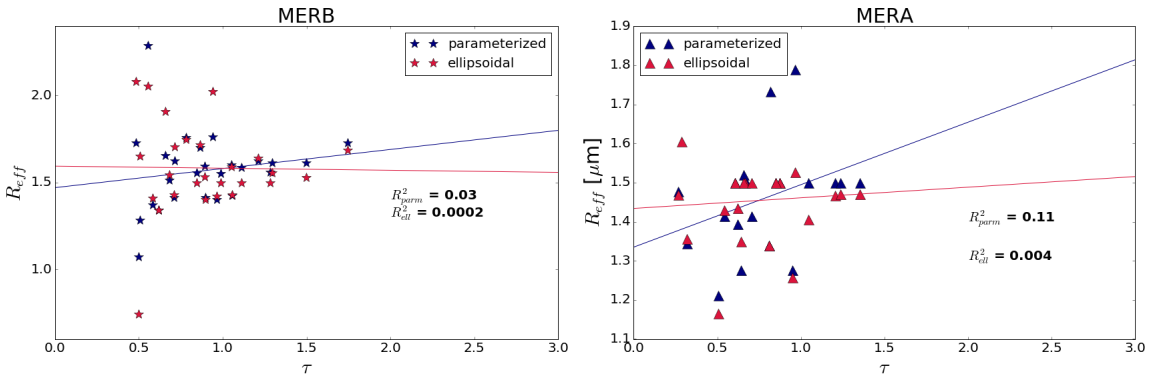

(a) (b)

Figure 5.23: Particle size results from MPFIT inversion for (a) MERB and (b) MERA as a function of optical depth using the parameterized phase function model (navy) and ellipsoidal model (red) to initialize the fitting procedure

trend, however, is not well correlated.

The Miniature Thermal Emission Spectrometer (Mini-TES) onboard each rover is a ground-based application of its larger parent instrument, the Thermal Emission Spectrometer (TES) onboard the Mars Global Surveyor (MGS) (Smith 2004, Smith et al. 2006). Generally Mini-TES observations are taken concurrently with that of Pancam optical depth so that a record of IR optical depth is available in conjunction with that of the 440 and 880 nm (L8 and R8) optical depth record (Lemmon et al. 2015).

The ratio of VIS/IR is diagnostic of particle size changes. Lemmon et al. (2015) shows in their figure 10 the ratio of IR/VIS as it pertains to particle size (derived in Wolff et al. (2006)). In the figure, the ratio of IR/VIS varies in diagnostic particle size from $\sim 1\mu$m to 2 μm for Spirit and Opportunity. Spirit particle sizes more generally center around 1.4 μm for much of the mission up to the onset of the 2007 global dust storm. Spikes in the ratio occur at the onset of the first dusty season near L_s = 135°, suggesting particle sizes greater than 2μm. This spike is seen for sol 350 in our results, where Opportunity (figure 5.21a) shows an increase to near 2μm using both models. This rise in particle size is not

observed in the Spirit results (figure 5.21b).

The lowest ratios and therefore the lowest derived particle sizes from Lemmon et al. (2015) occur during aphelion seasons. This compares to our results within the first 200 sols, when there is a discernible decrease in particle size. Opportunity particle sizes in our results for sol 900 - 1100 show smaller values near 1μm with steady increases at the onset of the global dust storm. This variation is not apparent for Spirit data over the same season, where particle sizes remain between 1.5 and 2 μm.

5.5 Discussion and summary

We have presented a method for retrieving the phase function at the time of observation directly from sky surveys without the need to assume particle size distributions or shape. By just looking at the phase function, we can discern seasonal trends up to the 2007 global dust storm. Despite an unconstrained phase function past 120°, the forward scattering peak is well defined. The slope of this peak becomes more negative during aphelion seasons than during perihelion seasons. Similarly, phase function values at 120° rise during dustier seasons. There is a noticeable change in the shape of the phase function with season for both Opportunity and Spirit. We subsequently fit two different phase function models to the the retrieved, tabulated phase functions to test particle size sensitivity. The results show little variation in particle size with season for both Spirit and Opportunity, which is consistent with previous results (Tomasko et al. 1999, Pollack et al. 1995). Mean particle sizes returned for each rover are 1.45 ± 0.12 μm (Spirit) and 1.58 ± 0.26 μm (Opportunity) when using the ellipsoidal model. When using the parameterized model, values are 1.46 $\pm$ 0.14 μm (Spirit) and 1.57 ± 0.21 μm (Opportunity).

6. QUICK-LOOK OPTICAL DEPTH FOR MSL OPERATIONAL USE

To date, the Mars Science Laboratory (MSL) Curiosity Rover has collected over 2000 sols of atmospheric and geologic data during its traverse through Gale crater. The rover contains a full suite of instruments dedicated to environmental readings including atmospheric pressure, temperature, and wind speed. These measurements comprise an extensive ground-based dataset with application to radiative transfer.

Unlike MER and Phoenix, MSL provides ground-based coverage of irradiance in the ultraviolet (UV) wavelength range using photodiode sensors. Measurements from these sensors can be used to retrieve atmospheric radiative information in an otherwise unobserved wavelength range at the surface. UV radiation measurements are important to retrieve accurate information pertaining to aerosols, dust load, cloud dynamics, and ozone (Zorzano et al. 2009). Absorption of UV impacts both total solar energy input and photochemical balance (Wolff et al. 2010).

Martian retrievals of optical depth have been limited in frequency and wavelength, and because optical depth is a wavelength-dependent and time-dependent parameter, models remain unconstrained in both scientific analysis and in an operational sense. Current optical depth is retrieved by direct solar imaging of the sun using Mastcam 440 nm and 880 nm filters at a frequency of twice per week (Vasavada et al. 2017). This optical depth only covers the visible and near infrared wavelengths. Ground-based UV measurements are not available through this method.

The Mars Exploration Rover missions and the Phoenix lander employed solar panels, so it was prudent within the mission framework to take optical depth measurements at least once per sol. MSL is powered by an RTG and does not require sol-to-sol observations. This does not imply that optical depth isn't necessary for operations or scientific analy-

sis. A high-frequency value can aide in the planning of other observation (McConnochie et al. 2018) through predictions of optical depth as well as provide extensive coverage for scientific work including overflights and GCM modeling.

Previous work has already identified the novelty of deriving UV optical depth and provides extensive analysis. Vicente-Retortillo et al. (2017) used shadow observations to solve for UV optical depth and report effective particle size ranging from 0.6 to 2 μm within Gale crater. Smith et al. (2016) performed full radiative transfer retrievals of UV optical depth on all six filters by pinning the value to Mastcam values and solving for the spatial response of each filter. They found that Mastcam optical depths could be reproduced well using a full radiative transfer retrieval. These results, however, only extend through 1.5 martian years.

The methodology used in Smith et al. (2016) is computationally expensive, and therefore cannot be used in an operational sense. Similarly, Vicente-Retortillo et al. (2017) runs an extensive model using only sols where the sensor falls into the mast shadow. While the work is comprehensive, it is computationally expensive and is limited to a single type of observation that does not capture sol-to-sol variation. The goal of the current work is to expand the record of optical depth reported by Smith et al. (2016) using a faster, simpler method that can be used on operational time scales. In addition the method presented increases frequency of optical depth observations, which improves upon that of Vicente-Retortillo et al. (2017).

This section focuses on retrieving optical depth using a simplified method as opposed to a full radiative transfer model. This is beneficial for operation use and will extend the optical depth record past 1.5 years. The following section describes the data structure and challenges of using the REMS UV data set. The third section presents optical depth results and a look at seasonal changes in diurnal variation. We summarize our results in the last section.

6.1 Data

REMS UV photodiode sensors are located on top of the rover deck (Zorzano et al. 2009). Their position relative to the Martian surface is dictated by the rover frame. Five of the six photodiodes contain filters for selective wavelength ranges while the sixth filter (UVABC) is designed to retrieve broadband UV. Each sensor has a field of view (FOV) of $\pm 30^{\circ}$ relative to the normal vector of the rover deck. The photodiodes measure current, which is then converted into irradiance. The final product represents the sum of intensity over the spatial solid angle of the sensor. REMS data is available through NASA PDS archive (http://pds-geosciences.wustl.edu/) in the form of Reduced Data Records (RDRs) (Gómez-Elvira et al. 2009). REMS observations are taken at minimum every hour for a duration of 5 minutes. Extended observations of an hour or more are often included in the cadence to monitor environmental conditions at interesting times or during other rover observations.

Two different RDR products, RNV and RTL, contain values in W/m^2 and current (mA), respectively, for all six sensors as well as the spacecraft clock time (SCLK), local mean solar time (LMST), and local true solar time (LTST). LMST is defined as a sol divided by 24 hours, whereas LTST represents the true time through which Mars has rotated for each sol. Thus, LMST noon changes relative to true noon (12:00 hour) for a given season. Figure 6.1 shows sol 63 data for both RTL and RNV and shows continuous and 5-minute blocks of observations, where the dip in irradiance from 12:00 LMST and 15:00 LMST is due to the sun positioning behind the rover mast.

Data is arranged by time according to the spacecraft clock (SCLK) value, which counts seconds past a defined reference time and is unique to a single mission. Observations are taken every second for at least 5 minutes during which time the signal is recorded along with SCLK value and rover position information. ADR files supplement RNV and RTL

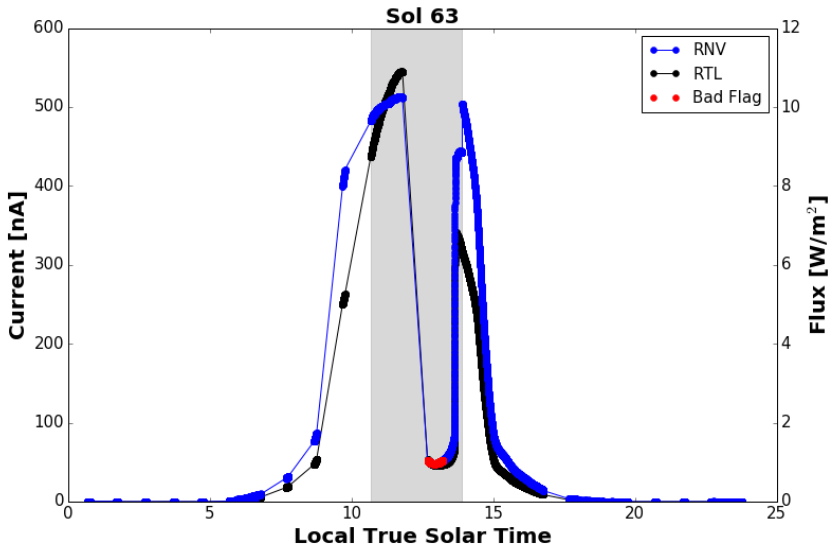

Figure 6.1: View of sol 63 RTL (black markers) and RNV (blue markers) product with 'bad flag' operator (red markers) for the UVA signal

and provide ancillary information including solar azimuth and elevation with respect to the rover frame at the time of observation.

6.1.1 Dust on sensors and shadow

To retrieve optical depth, irradiance must be modeled by first calculating radiance arriving at the sensor. Following that, the sensor spatial response and spectral response must be applied to this radiance field and integrated over solid angle. This, however, is difficult, as previously shown above, in that there is a third form of extinction. Dust can accumulate unevenly on the sensor surface with varying degrees of thickness. During high wind events dust can also be removed, which causes this accumulation to be nonlinear in time (Smith et al. 2016).

The sensors are also frequently within the shadow of the mast assembly, causing a dip in irradiance near local noon. Each SCLK and irradiance measurement is saved with an 8-

bit quality flag. The sixth bit represents the shadow quality of the measurement. Generally, a value of one represents no shadow and a value of zero represents partial or total shadow. For each sol, data outside the shadow are averaged in six-minute intervals between 04:00 LMST and 20:00 LMST. Shadow data are ignored using the bad flag qualifier, and UV data are limited to when the sun is in the FOV of the sensor but above the horizon. This not only increases computational efficiency, but removes some noise from the signal due to rover traverse.

6.2 Methodology

When the sun position is within the FOV of the sensor, direct extinction dominates the measured signal, and this allows us to simplify the light extinction model. Equation 6.1 shows a modified form of the Bourger-Lambert law used to describe direct irradiance extinction through a plane-parallel atmosphere. The signal received by the sensor is the product of three different attenuating processes: atmospheric attenuation, attenuation by dust covering the sensor, and adjustment for the spatial response of the sensor.

$$F = F_0 e^{\frac{-\tau_d}{\mu}} \mu^{\gamma} e^{\frac{-x\tau_m}{\mu_0}} \tag{6.1}$$

Attenuation through the atmosphere is exponential and is dependent on the optical depth of the layer. It takes the form e^{τ_{uv}/μ_0}, where μ_0 is the solar zenith angle relative to the local level plane of Mars. In this case, the layer is the depth of the martian atmosphere, and our optical depth, τ_{uv}, is the total extinction from scattering and absorption. This optical depth is related spectrally to the total column extinction taken using the Mastcam 880nm filter by a correction factor, x.

The correction factor assumes that the spectral dependence of optical depth varies linearly. This accounts for both wavelength dependence and multiple scattering that might be present despite dominance of direct extinction. The expected correction factor is 0.8 and is

estimated according to $\sqrt{(1-wg)}\sqrt{(1-w)}$, or the correction factor for total irradiance in a two stream approximation. It is determined using wavelength dependent values from Wolff et al. (2010). In this case, τ_{uv} = $x\tau$. Further attenuation from dust on the sensor requires an additional exponential extinction term, $e^{\tau_d/\mu}$, where μ is instead the solar zenith angle relative to the rover deck and τ_d represents the dust extinction factor.

$$\frac{\tau_d}{\mu} + \frac{x\tau}{\mu_0} = lnF_0 - lnF + \gamma ln\mu \tag{6.2}$$

Finally, the spatial response of each sensor must be accounted for in the signal and is assumed to be cosine in shape. Spatial response is dependent on the position of the sun relative to the rover and is adjusted using a gain parameter, γ. The effect is represented as μ^γ in equation 6.1. For RNV data products, this is applied in the calibration using a cosine function, Acos$^\gamma$(Bθ), where γ and A values are shown in table 6.1 and B = 1.73 for all photodiodes. Despite being included in calibration, adding this term in the analysis helps account for spurious effects of stray light and specular reflection from the rover mast. For most ground-based observations, calibrating for spatial response is sufficient to determine column extinction due to atmospheric attenuation.

Filter	$\lambda_{range}[nm]$	F$_{max}$ [W/m^2]	a	gain
UVA	315-370	25	2.91	7.29
UVB	270-320	6.4	6.69	5.53
UVC	215-277	1.57	6.72	28.98
UVABC	210-360	44.7	4.47	1.93
UVD	230-298	5	6.43	26.14
UVE	311-343	7.65	5.44	5.96

Table 6.1: UV filter wavelength ranges and calibration correction factors (Gómez-Elvira et al. 2009).

The linear form of equation 6.1 is shown in 6.2. Fitting occurs using MPFIT as described in section 2. The minimized error is the difference between the mean dust factor and the calculated dust factor at each time (equation 6.3) for each sol under the assumption that dust covering the sensor each sol experiences negligible change. All sols are fit simultaneously so that three parameters are returned for each UV filter.

$$\epsilon_i = \frac{\tau_{dij} - \overline{\tau_{di}}}{\sigma_i} \tag{6.3}$$

6.3 Results

For the purposes of this work, we present results using the UVA filter only. We show results for UVA RTL throughout the remainder of this section, where derived optical depth refers to the calculated τ at 880nm show in figure 6.2 and returned optical depth refers to the τ_{uv} = xτ optical depth with applied correction factor in table 6.2. Parameter results for RTL and RNV data fits are provided in table 6.2 for UVA RTL. The RTL filter returns a nonzero value for γ, which corresponds to the spatial response gain (μ^{γ}).

Filter	lnF_0	γ	x
UVA RTL	7.57	2.93	0.69

Table 6.2: Returned parameters from fitting for UVA RTL.

6.3.1 Derived optical depth

The derived optical depth was found by running the forward model using the returned parameters to calculate τ. The results for UVA RTL shown in figure 6.2 match that of Mastcam τ remarkably well. The seasonal trend is clearly visible. The first 100 sols of

the mission show low optical depth followed by a rise in dust activity. This activity results in a rise in Mastcam optical depth to values around 1.2. The dust activity subsides by sol 500. REMS captured this rise and decay, while also showing spikes in optical depth that were not captured by Mastcam tau, as is the case near sol 600 and later in the mission near sol 1900.

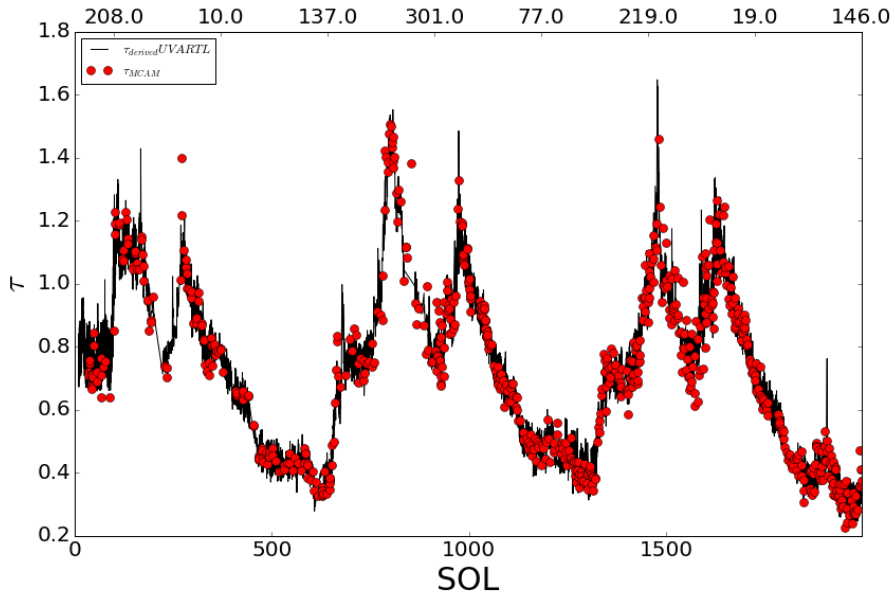

Figure 6.2: Derived 880nm optical depth for REMS RTL (black) plotted with Mastcam 880nm τ (red). Solar longitude values are printed on the top axis.

Points where the results do not capture high optical depth are likely due to data filtering. If the solar zenith angle does not fall within the specified range, if the shadow quality flag is present, or if no measurements were taken that sol, the observations for that sol are disregarded in the fitting process. This is exemplified by the absence of data near sol 200, which corresponds to a lack of results in derived RTL optical depth. Despite this filtering process and periodic lack of observations, coverage is good for derived REMS optical

depth, showing that this simplified model can reproduce remarkably the Mastcam 880nm optical depth.

6.3.2 Dust attenuation factor

Figure 6.3 shows the dust attenuation factor, τ_d, which represents the extinction from dust covering the sensors. τ_d is calculated following final parameter return. During fitting, τ_d is set to zero on sol 33 with the assumption that no significant amount of dust cover is present on the sensors. This allows the modeled value to drop below zero. τ_d represents an effective settled dust optical depth, so an increase in this value corresponds to more attenuation from dust cover. Low dust activity, represented by low optical depth seasons, is inversely proportional to high dust attenuation factor values. For instance, sol 500 to 600 shows $\tau_{880} < 0.6$, compared to that of $\tau_{880} > 0.6$ for seasons directly before and after. The corresponding dust attenuation factors show a local maximum, ranging from 0.2 - 0.4.

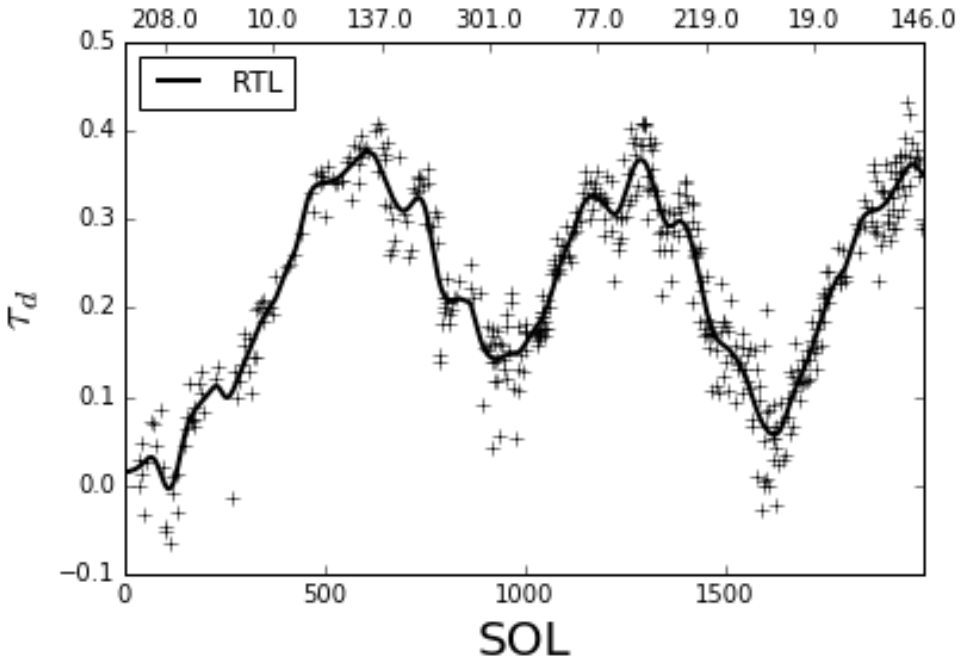

Figure 6.3: Dust correction factor (plus symbol) with smoothed line (solid) for UVA RTL filter. Solar longitude is printed on the top axis.

Frequent wind events are expected to clear the dust from the sensors (Smith et al. 2016). During the southern hemisphere winter season, near sols 500-600 for example, the atmosphere is relatively calm, and mechanisms for dust lifting, including dust devils and regional storms, are less frequent. We expect that during these seasons, dust accumulation generally trends upward or remains constant. Local events are capable of clearing the sensors, but the overall trend in figure 6.3 during low optical depth seasons is increasing.

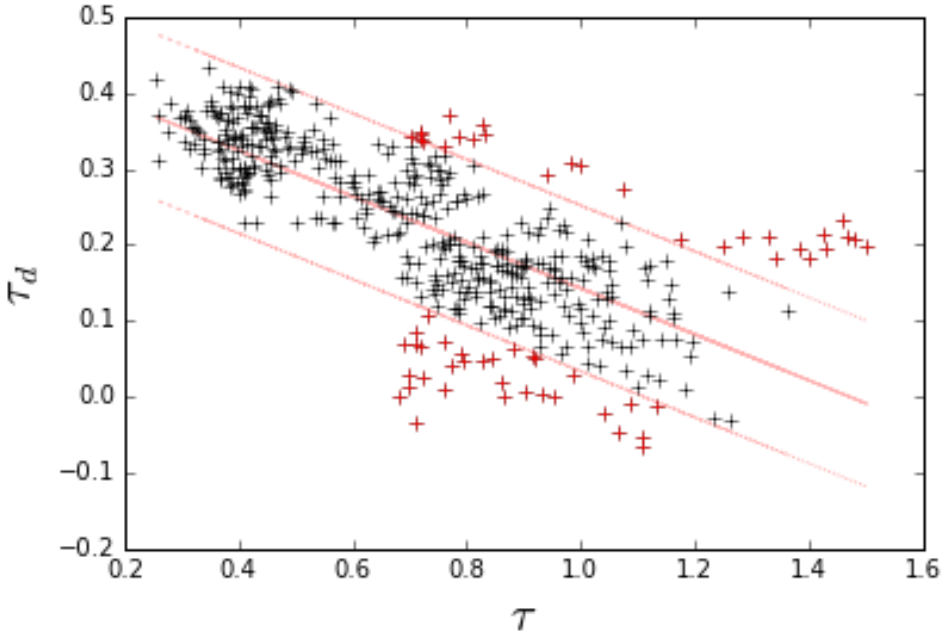

Figure 6.4: Dust correction factor as a function of optical depth with linear trend (red solid) and 1σ deviation from linear trend (red dashed).

The dust factor is inversely proportional to the returned optical depth. Optical depth varies with season, and for high optical depth, atmospheric activity like local wind-driven events create dust lifting. These same wind events are expected to be responsible for clearing the sensors. The spread in results is tightly constrained in figure 6.4 for low optical depth. As optical depth increases, the spread in values deviates more from its linear trend.

6.3.3 Diurnal variation

Diurnal variation is expected in the optical depth due to both the change in airmass ($1/\cos\theta$) and real atmospheric variations. The Martian atmosphere responds quickly to solar radiation or lack thereof, as it is an efficient radiator to space at night and heats quickly at sunrise during the day. This gives way to thermal tides and changes in dust

lifting. During the dusty season near perihelion, this activity increases as the southern hemisphere is illuminated for longer. Higher dust activity changes the optical depth and produces a diurnal variation.

REMS coverage is more frequent, and optical depth has been derived for an interval of time surrounding local noon. Though data are filtered to only account for direct extinction, there are still a good number of data points that fall within this range. Figure 6.5 gives the optical depth of each sol relative to the mean optical depth for that sol, $\tau_i - \overline{\tau}$. A typical sol generally begins with high optical depth followed by a decrease in optical depth as airmass decreases and a rise in optical depth as the sun sets. A higher mean optical depth and smaller deviation from this mean suggest higher dust loading.

Deviations from the mean in the RTL plot seem to follow a seasonal pattern, with higher positive values between 9:00 and 10:00 LTST between sols 0-200, 700-1000, and 1400-1600. These deviations correspond to dustier seasons. Besides this trend, however, there is no solid evidence of any seasonal trend in diurnal variation. Gaps in the results make it difficult to assess the same LTST during aphelion seasons due to the changes in length of day.

Activity in the morning or at noon can increase dust loading into the atmosphere, which causes asymmetry in the afternoon and morning τ profiles. When an inversion develops at night, dust activity ceases, and clearing can take place. The REMS data show no evidence of asymmetry between morning and afternoon values in figure 6.5, with patterns seemingly more dependent on local changes in atmosphere than on seasonal trends.

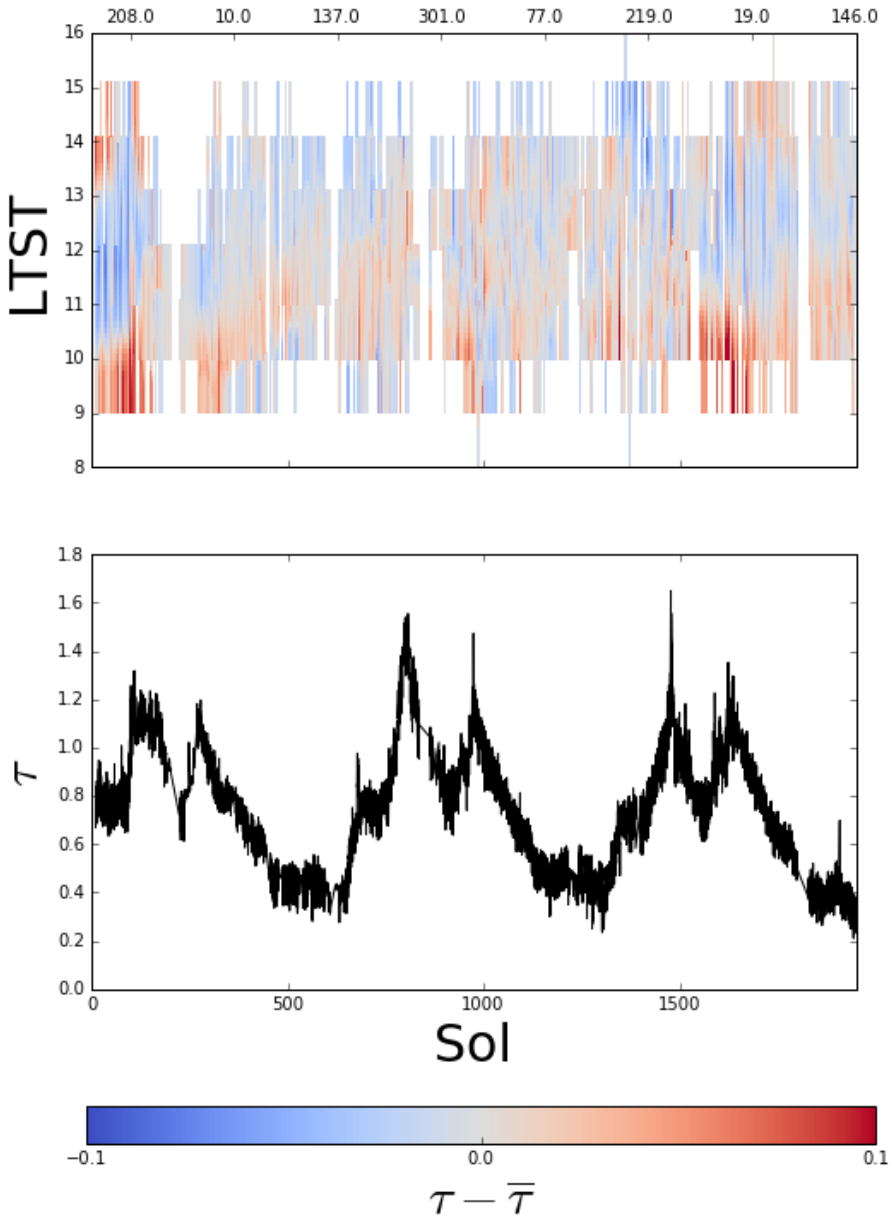

Figure 6.5: Diurnal variation relative to the mean optical depth derived using REMS UV sensor data.

Smith et al. (2016) reports changes in fractional residuals when comparing modeled flux to observed UV flux. The fit to the full radiative transfer model was performed assuming that there is no diurnal variation in optical depth. Smith et al. (2016) note that,

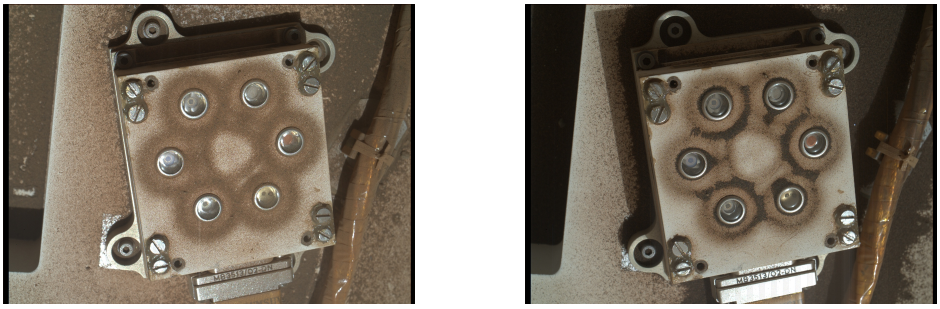

(a) (b)

Figure 6.6: MAHLI images of the REMS UV sensors for (a) sol 1314 and (b) sol 1614 showing dust covering for decreased and increased optical depth, respectively. Image credit: NASA/JPL-Caltech/MSSS

even though increased and decreased optical depth over a single sol could change the flux significantly, this effect is more correlated with solar zenith angle, a trend caused by overestimating or underestimating particle size. The results presented here are consistent with Smith et al. (2016) work in that there is no discernible seasonal trend in the diurnal variation of optical depth.

The Mars Hand and Lens Imager (MAHLI) takes images of the REMS UV sensors operationally every 60 sols. The images can be used to assess the dust cover on the top of each sensor. These images are available on the PDS node and through a secondary site `http://www.midnightplanets.com/web/MSL/`. Two such images are shown in figure 6.6 for low (a) and high (b) optical depth. The image in figure 6.6a was taken on sol 1314 and shows a dusty layer surrounding each sensor. Figure 6.6b shows an image taken during peak optical depth on sol 1614, 300 sols later. The sensors are remarkably more clear with little dust cover, suggesting that dust was removed from the sensors between the two sols. This removal is likely from local wind events.

The two MAHLI images in no way prove that a local wind event is the dominant removal mechanism. In fact, the 60-sol frequency of the images is not enough to capture

local events. The MAHLI images do show, however, that clearing took place in a non-sequential manor. Earlier sols show higher dust coverings while later sols seem relatively clear. The images do show a correlation of dust removal with season. Further analysis on these images is beyond the scope of this dissertation.

6.4 Summary

The simplified model with REMS performs well when deriving optical depth. This allows us to fill in gaps in the Mastcam 880nm optical depth and assess future optical depth for better operational planning. As is the case in Smith et al. (2016), MastCam 880nm optical depth is necessary to constrain the returned results upon fitting. Unfortunately this does not provide a standalone method for UV optical depth retrieval and removes information on wavelength dependence. It does, however, fill in the gaps where Mastcam did not take observations. This increased frequency for REMS observations captures high optical depth events that Mastcam optical depth frequencies cannot not due to operational constraints. These events are consistent with that of Smith et al. (2016).

Seasonal trends in diurnal activity are not evident in the current results, partly due to the lack of coverage at all LTST throughout the mission and the constraint of having the sun in the FOV. However, values capture local changes in atmospheric activity and can still be used as estimates in modeling. For small scale variations or events, such as dust devils, REMS UV results compliment other measurements on finer timescales than those of Mastcam. These results mostly show the utility of using a simplified model to predict optical depth, even if it is tied to the Mastcam observations, as this is operationally useful for planning. The current algorithm can be easily implemented through IDL scripting language and results are easy to update on a sol-to-sol basis.

7. CONCLUSIONS AND SUMMARY

This work models sky brightness as a function of scattering angle and assesses the uncertainty within each model to ultimately derive particle size. At the Phoenix landing site, size distribution is tested using a parameterized phase function (Pollack et al. 1995, Pollack & Cuzzi 1980). Returned particle size parameters show little deviation from the initial value of 1.5 μm $\pm$ 0.15, with a 10$\%$ adopted uncertainty. Similarly, effective variance values stay within a range of 0.2-0.4. Modeled sky brightness shows little sensitivity to the variance, but high sensitivity to assumed optical depth and effective particle size. The choice of distribution is shown to not matter in the case of gamma, or bimodal, with the latter tending towards a mono-modal shape. The choice of bimodal distributions tend to produce worse fits in both a χ^2 sense and overall shape.

Phoenix sky survey observations are fit also to a model that is constructed from a randomly oriented mixture of ellipsoids whose properties are contained within a readily accessible database. Particle size results are not different between the values obtained from using a parameterized model, with a mean of 1.68 $\pm$ 0.41 μm. There is no significant difference between the mean particle sizes from either model. While fits using ellipsoids are better for surveys containing higher scattering angles, those with limited scattering angle range do not perform better than their parameterized counterpart and add unknown parameters to the fitting algorithm in the form of a bivariate shape distribution.

Instead of fitting I/F using a phase function model, phase functions are inverted directly from MER sky surveys and results are assessed through the shape of the phase function. This inversion is initiated by using both the ellipsoidal and parameterized phase function models, but returned phase function is not constrained to follow either shape. Overall, the results return a shallow, high backscattering phase function near perihelion, while aphe-

lion seasons are marked by steep slopes and low backscatter. Regardless of these trends, returned particle sizes fit to the retrieved phase functions themselves show little variation, with an overall particle size of 1.45 $\pm$ 0.12 μm (Spirit) and 1.58 $\pm$ 0.26 μm (Opportunity) when using the ellipsoidal model. When using the parameterized model, values are 1.46 $\pm$ 0.14 μm (Spirit) and 1.57 $\pm$ 0.21 μm (Opportunity).

Finally, in addition to particle investigations, a brief section on ultraviolet optical depth is presented using data from the Rover Environmental Monitoring Station (REMS) onboard the Mars Science Laboratory (MSL) Curiosity rover in Gale Crater. We present results for retrieving optical depth through a simplified, modified Beer's law in an effort to increase optical depth retrieval frequency between the standard Mast Camera (Mastcam) tau observations. The retrieved UV optical depths show an ability to reproduce those of Mastcam and can ultimately be used as a measure of optical depth on operational timescales.

The results presented here add to the overall knowledge of Martian dust aerosols and will help to inform modelers regarding the physical properties of the dust as well as optical depth in Gale crater. This body of work spans multiple locations and timeframes on the surface of Mars, and by doing so, shows consistency in atmospheric measurements over time and space. Further more, we present a phase function model based on physical shape that can reproduce the observed brightness with the same accuracy as that of an empirical model used in previous studies. This model and the values presented here will inform future investigations on Mars.

REFERENCES

Bangalath, H. K. & Stenchikov, G. (2015), 'Role of dust direct radiative effect on the tropical rain belt over Middle East and North Africa: A high-resolution AGCM study', *Journal of Geophysical Research: Atmospheres* **120**, 4564–4584.

Bell III, J., Joseph, J., Sohl-Dickstein, J., Arneson, H., Johnson, M., Lemmon, M. & Savransky, D. (2006), 'In-flight calibration and performance of the Mars Exploration Rover Panoramic Camera (Pancam) instruments', *Journal of Geophysical Research* **111**(E02S03).

Bell III, J., Squyres, S., Herkenhoff, K., Maki, J., Arneson, H., Brown, D., Collins, S., Dingizian, A., Elliot, S., Hagerott, E., Hayes, A., Johnson, M., Johnson, J. R., Joseph, J., Kinch, K., Lemmon, M., Morris, R., Scherr, L., Schwochert, M., Shepard, M., Smith, G., Sohl-Dickstein, J., Sullivan, R., Sullivan, W. & Wadsworth, M. (2003), 'Mars Exploration Rover Athena Panoramic Camera (Pancam) investigation', *Journal of Geophysical Research* **108**(E12), 8063.

Bi, L., Yang, P., Kattawar, G. W. & Kahn, R. (2009), 'Single-scattering properties of triaxial ellipsoidal particles for a size parameter range from the Rayleigh to geometric-optics regimes', *Applied Optics* **48**(1), 114 – 126.

Clancy, R., Lee, S., Gladstone, G., McMillan, W. & Rousch, T. (1995), 'A new model for mars atmospheric dust based upon analysis of ultraviolet through infrared observations from mariner 9, viking, and phobos', *Journal of Geophysical Research* **100**, 5251–5263.

Clancy, T. R. & Lee, S. W. (1991), 'A New Look at Dust and Clouds in the Mars Atmosphere: Analysis of Emission-Phase-Function Sequences from Global Viking IRTM Observations', *Icarus* **93**, 135–158.

Clancy, T. R. & Wolff, M. J. (2003), 'Mars aerosol studies with the MGS TES emission

phase function observations: Optical depths, particle sizes, and ice cloud types versus latitude and solar longitude', *Journal of Geophysical Research* **108**(E9), 5098.

Dabrowska, D., Muñoz, O., Mereno, F., Ramos, J. & Martínez-Frías, J. (2015), 'Scattering matrices of martian dust analogs at 488 nm and 647 nm', *Icarus* **250**, 83–94.

Daerden, F. ad Whiteway, J., Neary, L., Komguem, L., Lemmon, M., Heavens, N., Cantor, B., Hébrard, E. & Smith, M. (2015), 'A solar escalator on Mars: Self-lifting of dust layers by radiative heating', *Geophysical Research Letters* **42**, 7319–7326.

Das, S., Taori, A. & Jayaraman, A. (2011), 'On the role of dust storms in triggering atmospheric gravity waves observed in the middle atmosphere', *Annales Geophysicae* **29**, 1647–1654.

Di, K. & Li, R. (2004), 'CAHVOR camera model and its photogrammetric conversion for planetary applications', *Journal of Geophysical Research* **109**(E04004).

D.S., C., Pollack, J. & Haberle, R. (1988), Diurnal variations in optical depth at mars: Observations and interpretations, Technical Memorandum 100057, National Aeronautics and Space Administration.

Dubovik, O., Sinyuk, A., Lapyonok, T., Holben, B. N., Mishchenko, M., Yang, P., Eck, T. F., Volten, H., Muñoz, O., Veihelmann, B., Zande, W. J. v. d., Leon, J.-F., Sorokin, M. & Slutsker, I. (2006), 'Application of spheroid models to account for aerosol particle nonsphericity in remote sensing of desert dust', *Journal of Geophysical Research* **111**(D11208).

Fedorova, A., Montmessin, F., Rodin, A., Korablev, O., Määttänen, A., Maltagliati, L. & Bertaux, J.-L. (2014), 'Evidence for a bimodal size distribution for the suspended aerosol particles on Mars', *Icarus* **231**, 239–260.

Gierasch, P. J. & Goody, R. M. (1971), 'The effect of dust on the temperature of the Martian Atmosphere', *Journal of Atmospheric Sciences* **29**, 400 – 402.

Gómez-Elvira, J., Torre, M. d. l. & REMS Team (2009), 'REMS Calibration Plan',

NASA/JPL/CAB **Issue 02**.

Hansen, J. E. & Travis, L. D. (1974), 'Light scattering in planetary atmospheres', *Space Science Review* **16**, 527–610.

Hapke, B. (1981), 'Bidirectional reflectance spectroscopy', *Journal of Geophysical Research* **86**(B4), 3039–3054.

Johnson, J. R., Grundy, W. M. & Lemmon, M. T. (2003), 'Dust deposition at the Mars Pathfinder landing site: observations and modling of visible/near-infrared spectra', *Icarus* **163**, 330–346.

Kalashnikova, O. & Sokolik, I. (2004), 'Modeling the radiative properties of nonspherical soil-derived mineral aerosols', *Journal of Quantitative Spectroscopy and Radiative Transfer* **87**, 137–166.

Lemmon, M. (2010), Martian Cirrus-like Hazes at the Phoenix Landing Site, number LPI Contribution No. 1533, 41st Lunar and Planetary Science XLI, Woodlands, Texas.

Lemmon, M. T., Wolff, M. J., Bell III, J. F., Smith, M. D., Cantor, B. A. & Smith, P. H. (2015), 'Dust aerosol, coulds, and the atmospheric optical depth record over 5 Mars years of the Mars Exploration Rover mission', *Icarus* **251**, 96–111.

Lemmon, M., Wolff, M., Smith, M., Clancy, R., Banfield, D., Landis, G. A., Ghosh, A., Smith, P., Spanovich, N., Whitney, B., Whelley, P., Greeley, R., Thompson, S., Bell III, J. & Squyres, S. (2004), 'Amtospheric Imaging Results from the Mars Exploration Rovers', *Science* **306**, 1753–1756.

Li, R., Di, K., Matthies, L. H., Arvidson, R. E., Folkner, W. M. & Archinal, B. A. (2004), 'Rover Localization and Landing-Site Mapping Technology for the 2003 Mars Exploration Rover Mission', *Photogrammetric Engineering and Remote Sensing* **70**(1), 77–90.

Li, R., Squyres, S. W., Arvidson, R. E., Archinal, B. A., Bell, J., Cheng, Y., Crumpler, L., Des Marais, D. J., Di, K., Ely, T. A., Golombek, M., Graat, E., Grant, J., Guinn,

J., Johnson, A., Greeley, R., Kirk, R. L., Maimone, M., Mattheis, L. H., Malin, M., Parker, T., Sims, M., Soderblom, L. A., Thompson, S., Wang, J., Whelley, P. & Zu, F. (2005), 'Initial Results of Rover Localization and Topographic Mapping for the 2003 Mars Exploration Rover Mission', *Photogrammetric Engineering and Remote Sensing* **71**(10), 1129–1142.

Mahowald, N., Albani, S., Kok, J., Engelstaeder, S., Scanza, R., Ward, D. S. & Flanner, M. G. (2014), 'The size distribution of desert dust aerosols and its impact on the earth system', *Aeolian Research* **15**, 53–71.

Maki, J., Lorre, J., Smith, P., Brandt, R. & Steinwand, D. (1999), 'The color of Mars: Spectrophotometric measurements at the Pathfinder landing site', *Journal of Geophysical Research* **104**(E4), 8781–8794.

Markwardt, C. B. (2009), Non-Linear Least Squares Fitting in IDL with MPFIT, *in* D. A. Bohlender, D. Druand & P. Dowler, eds, 'Astronomical Data Analysis Software and Systems XVIII', Vol. 411 of *Astronomical Society of the Pacific Conference Series*, Astronomical Data Analysis Software and Systems XVIII, Quebec, Canada, p. 251.

McConnochie, T. H., Smith, M. D., Wolff, M. J., Bender, S., Lemmon, M., Wiens, R. C., Maurice, S., Gasnault, O., Lasue, J., Meslin, P.-Y., Harri, A.-M., Genzer, M., Kemppinen, O., Martínez, G. M., DeFlores, L., Blaney, D., Johnson, J. R. & Bell III, J. (2018), 'Retrieval of water vapor column abundance and aerosol properties from chemcam passive sky spectroscopy', *Icarus* **307**, 294–326.

Meng, Z., Yang, P., Kattawar, G. W., Bi, L., Liou, K. & Laszlo, I. (2010), 'Single-scattering properties of tri-axial ellipsoidal mineral dust aerosols: A database for application to radiative transfer calcuations', *Journal of Aerosol Science* **41**, 501–512.

Merikallio, S., Muñoz, O., Sundstrom, A.-M., Virtanen, T., Horttanainen, M., Leeuw, G. d. & Nousiainen, T. (2015), 'Optical modeling of volcanic ash particles using ellipsoids', *Journal of Geophysical Research: Atmospheres* **120**.

Merikallio, S., Nousiainen, T., Kahnert, M. & Harri, A.-M. (2013), 'Light scattering by the Martian dust analog, palagonite, modeled with ellipsoids', *Optics Express* **21**(15).

Montmessin, F., Forget, F., Rannou, P., Cabane, M. & Haberle, R. (2004), 'Origin and role of water ice clouds in the martian water cycle as inferred from a general circulation model', *Journal of Geophysical Research* **109**(E10004).

Petty, G. W. & Huang, W. (2011), 'The Modified Gamma Size Distribution Applied to Inhomogeneous and Nonspherical Particles: Key Relationships and Conversions', *Journal of Atmospheric Sciences* **68**, 1460–1473.

Pike, W., Staufer, U., Hecht, M., Goetz, W., Parrat, D., Sykulska-Lawrence, H., Vijendran, S. & Madsen, M. (2011), 'Quantification of the dry history of the Martian soil inferred from in situ microscopy', *Geophysical Research Letters* **38**(L24201).

Pollack, J. B. & Cuzzi, J. N. (1980), 'Scattering by nonspherical particles of size comparable to a wavelength: A new semi-emperical theory and its application to tropospheric aerosols', *Journal of Atmospheric Sciences* **37**, 868–881.

Pollack, J., Ockert-Bell, M. E. & Shepard, M. K. (1995), 'Viking lander image analysis of martian atmospheric dust', *Journal of Geophysical Research* **100**(E3), 5235–5250.

Showalter, M., Pollack, J., Ockert, M., Doyle, L. & Dalton, J. (1992), 'A photometric study of Saturn's F-ring', *Icarus* **100**, 394–411.

Smith, M. D. (2004), 'Interannual variability in TES atmospheric observations of Mars during 1999–2003', *Icarus* **167**, 148–165.

Smith, M. D. (2008), 'Spacecraft observations of the Martian atmosphere', *Annual Review Earth Planet Science* **36**, 191–219.

Smith, M. D., Wolff, M. J., Spanovich, N., Ghosh, A., Banfield, D., Christensen, P. R., Landis, G. A. & Squyres, S. W. (2006), 'One Martian year of atmospheric observations using MER Mini-TES', *Journal of Geophysical Research* **111**(E12S13).

Smith, M. D., Zorzano, M.-P., Lemmon, M., Martín-Torres, J. & Mendaza de Cal, T.

(2016), 'Aerosol optical depth as observed by the Mars Science Laboratory REMS UV photodiodes', *Icarus* **280**, 234–248.

Smith, P. H. & Lemmon, M. (1999), 'Opacity of the Martian atmosphere measured by the Imager for Mars Pathfinder', *Journal of Geophysical Research* **104**(E4), 8975–8985.

Soderblom, J., Wolff, M. & Bell III, J. (2008), Temporal variations in the size distribution of martian atmospheric dust from mars exploration rover navcam observations, Lunar and Planetary Science XXXIX.

Sokolik, I., Winker, D., Bergametti, G., Gillette, D., Carmichael, G., Kaufman, Y., Gomes, L., Schuetz, L. & Penner, J. (2001), 'Introduction to special section: Outstanding problems in quantifying the radiative impacts of mineral dust', *Journal of Geophysical Research* **106**(D16), 18,015–18,027.

Stamnes, K., Tsay, S.-C. & Laszlo, I. (2000), DISORT, a General-Purpose Fortran Program for Discrete-Ordinate-Method Radiative Transfer in Scattering and Emitting Layered Media: Documentation of Methodology.

Stamnes, K., Tsay, S.-C., Wiscombe, W. & Jayaweera, K. (1988), 'Numerically stable algorithm for discrete-ordinate-method radiative transfer in multiple scattering and emitting layered media', *Applied Optics* **27**(12), 2502–2509.

Taylor, P. A., Li, P.-Y., Michelangeli, D. V., Pathak, J. & Weng, W. (2007), 'Modelling dust distributions in the atmospheric boundary layer on Mars', *Boundary-Layer Meteorol* **125**, 305–328.

Tegan, I. & Miller, R. (1998), 'Climate effect of soil dust aerosols', *Journal of Aerosol Science* **29**(1), S1013–S1014.

Tomasko, M., Doose, L., Lemmon, M., Smith, P. & Wegryn, E. (1999), 'Properties of dust in the Martian atmosphere from the Imager on Mars Pathfinder', *Journal of Geophysical Research* **104**(E4), 8987–9007.

Toon, O. B., Pollack, J. B. & Sagan, C. (1977), 'Physical Properties of Particles Compos-

ing the Martian Dust Storm of 1971-1972', *Icarus* **30**, 663–696.

Vasavada, A., Piqueux, S., Lewis, K., Lemmon, M. & Smith, M. (2017), 'Thermophysical properties along Curiosity's traverse in Gale Crater, Mars, derived from the REMS Ground Temperature Sensor', *Icarus* **284**, 372–386.

Vicente-Retortillo, A., Martínez, G. M., Renno, N. O., Lemmon, M. T. & Torre-Juárez, M. (2017), 'Determination of dust aerosol particle size at Gale Crater using REMS UVS and Mastcam measurements', *Geophysical Research Letters* **44**.

Wang, H. & Fisher, J. A. (2009), 'North polar frontal clouds and dust stroms on Mars during spring and summer', *Icarus* **204**, 103 – 113.

Wiscombe, W. (1977), 'The Delta-M Method: Rapid Yet Accurate Radiative Flux Calculations for Strongly Asymmetric Phase Functions', *Journal of Atmospheric Sciences* **34**, 1408–1422.

Wolff, M. J. & Clancy, T. (2003), 'Constraints on the size of Martian aerosols from Thermal Emission Spectrometer observations', *Journal of Geophysical Research* **108**(E9), 5097.

Wolff, M. J., Clancy, T. R., Goguen, J. D., Malin, M. C. & Cantor, B. A. (2010), 'Ultraviolet dust aerosol properties as observed by MARCI', *Icarus* **208**, 143–155.

Wolff, M. J., Smith, M. D., Clancy, T. R., Spanovich, N., Whitney, B., Lemmon, M., Bandfield, J., Banfield, D., Ghosh, A., Landis, G., Christensen, P., Bell III, J. & Squyres, S. (2006), 'Constraints on dust aerosols from the Mars Exploration Rovers using MGS overflights and Mini-TES', *Journal of Geophysical Research* **111**(E12S17).

Wolff, M., Smith, M., Clancy, R., Arvidson, R., Kahre, M., Seelos IV, F., Murchie, S. & Savijärvi, H. (2009), 'Wavelength dependence of dust aerosol single scattering albedo as observed by the Compact Reconnaissance Imaging Spectrometer', *Journal of Geophysical Research* **114**(E00D04).

Zorzano, M.-P., Vázquez, L. & Jimenez, S. (2009), 'Retrieval of ultraviolet spectral irra-

diance from filtered photodiode measurements', *Inverse Problems* **25**(115023 (9pp)).

APPENDIX

Survey	Sol + LMST	Solar Elevation	τ
17CC	69.65	55.5	0.34
13AE	32.76	69.1	0.63
12FE	25.42	46.7	0.46
141E	37.46	44.2	0.70
1421	37.55	44.9	0.67
1424	37.66	55.7	0.69
1427	37.77	69.6	0.72
153D	48.32	56.5	0.43
1710	63.41	48.5	0.30
17DA	70.43	46.7	0.35
1813	71.74	67.4	0.28
185D	73.74	67.5	0.26
18CB	77.44	47.0	0.28
195B	81.00	0.0	0.00
1A92	90.72	66.2	0.31
1AE1	93.76	71.7	0.31
1C10	104.42	50.8	0.31
1C37	105.78	74.9	0.42
1CE2	111.80	78.5	0.30
1D5F	115.70	67.7	0.25
1F1D	133.67	64.9	0.34
1FF0	143.68	69.4	0.30
2019	145.56	57.5	0.30

Table A1: Selected surveys from Phoenix landing site observations used in the study for ellipsoidal phase function

Survey	Filter	λ [nm]	τ	n_i	G	θ_{min}	GR	Sol	LMST
13AE	LC	968.5	0.62	0.00432	75.7	164.0	0.244	32	0.758507
13AE	R8	754.2	0.60	0.00175	83.0	146.1	0.247	32	0.758507
13AE	RC	485.3	0.61	0.00768	104.4	139.0	0.054	32	0.758507
17CC	L2	446.6	0.28	0.00989	114.1	138.1	0.041	69	0.649120
17CC	LC	968.5	0.28	0.00432	75.7	164.0	0.244	69	0.649120
17CC	R2	446.7	0.28	0.00988	114.0	138.1	0.041	69	0.649120
17CC	R8	754.2	0.29	0.00175	83.0	146.1	0.247	69	0.649120
17CC	RA	603.8	0.29	0.00226	89.2	141.2	0.175	69	0.649120
17DA	L2	446.6	0.32	0.00989	114.1	138.1	0.041	70	0.433044
17DA	LC	968.5	0.34	0.00432	75.7	164.0	0.244	70	0.433044
17DA	R2	446.7	0.32	0.00988	114.0	138.1	0.041	70	0.433044
17DA	R8	754.2	0.35	0.00175	83.0	146.1	0.247	70	0.433044
17DA	RA	603.8	0.34	0.00226	89.2	141.2	0.175	70	0.433044
141E	L2	446.6	0.67	0.00989	114.1	138.1	0.041	37	0.455613
141E	LC	968.5	0.69	0.00432	75.7	164.0	0.244	37	0.455613
141E	R2	446.7	0.67	0.00988	114.0	138.1	0.041	37	0.455613
141E	R8	754.2	0.70	0.00175	83.0	146.1	0.247	37	0.455613
141E	RA	603.8	0.69	0.00226	89.2	141.2	0.175	37	0.455613
1421	L2	446.6	0.67	0.00989	114.1	138.1	0.041	37	0.550139
1421	LC	968.5	0.69	0.00432	75.7	164.0	0.244	37	0.550139
1421	R2	446.7	0.67	0.00988	114.0	138.1	0.041	37	0.550139
1421	R8	754.2	0.70	0.00175	83.0	146.1	0.247	37	0.550139
1421	RA	603.8	0.69	0.00226	89.2	141.2	0.175	37	0.550139
1424	L2	446.6	0.67	0.00989	114.1	138.1	0.041	37	0.660370
1424	LC	968.5	0.69	0.00432	75.7	164.0	0.244	37	0.660370
1424	R2	446.7	0.67	0.00988	114.0	138.1	0.041	37	0.660370
1424	R8	754.2	0.70	0.00175	83.0	146.1	0.247	37	0.660370
1424	RA	603.8	0.69	0.00226	89.2	141.2	0.175	37	0.660370
1427	L2	446.6	0.67	0.00989	114.1	138.1	0.041	37	0.767535
1427	LC	968.5	0.69	0.00432	75.7	164.0	0.244	37	0.767535
1427	R2	446.7	0.67	0.00988	114.0	138.1	0.041	37	0.767535
1427	R8	754.2	0.70	0.00175	83.0	146.1	0.247	37	0.767535
1427	RA	603.8	0.69	0.00226	89.2	141.2	0.175	37	0.767535
2007	LC	968.5	0.34	0.00432	75.7	164.0	0.244	144	0.587442
2007	R8	754.2	0.35	0.00175	83.0	146.1	0.247	144	0.587442
2007	RC	485.3	0.33	0.00768	104.4	139.0	0.054	144	0.587442
2095	LC	968.5	0.51	0.00432	75.7	164.0	0.244	151	0.617292
2095	R8	754.2	0.54	0.00175	83.0	146.1	0.247	151	0.617292
2095	RC	485.3	0.53	0.00768	104.4	139.0	0.054	151	0.617292
195B	R8	754.2	0.27	0.00175	83.0	146.1	0.247	81	0.602153

Table A2: Selected surveys from Phoenix landing site observations and assumed phase function parameters used in the study for parameterized phase function

ROV	SOL	FILT
Opportunity	0027	l2
Opportunity	0124	l2
Opportunity	0140	l2
Opportunity	0203	l2
Opportunity	0251	l2
Opportunity	0333	l2
Opportunity	0338	l2
Opportunity	0426	l2
Opportunity	0490	l2
Opportunity	0494	l2
Opportunity	0519	l2
Opportunity	0543	l2
Opportunity	0572	l2
Opportunity	0625	l2
Opportunity	0627	l2
Opportunity	0640	l2
Opportunity	0643	l2
Opportunity	0650	l2
Opportunity	0658	l2
Opportunity	0699	l2
Opportunity	0752	l2
Opportunity	0839	l2
Opportunity	0957	l2
Opportunity	1054	l2
Opportunity	1101	l2
Opportunity	1215	l2

Table A3: Selected surveys from MERB low-sun sky survey observations

ROV	SOL	FILT
Spirit	0049	l2
Spirit	0118	l2
Spirit	0211	l2
Spirit	0361	l2
Spirit	0422	l2
Spirit	0456	l2
Spirit	0486	l2
Spirit	0515	l2
Spirit	0519	l2
Spirit	0526	l2
Spirit	0545	l2
Spirit	0565	l2
Spirit	0624	l2
Spirit	0643	l2
Spirit	0650	l2
Spirit	0679	l2
Spirit	0756	l2
Spirit	0863	l2
Spirit	0980	l2
Spirit	1090	l2
Spirit	1152	l2
Spirit	1198	l2
Spirit	1243	l2

Table A4: Selected surveys from MERA low-sun sky survey observations

Survey	Filter	Sol	R_{eff}	v_{eff}	τ	RMS	χ^2_v
13AE	LC	32	1.33	0.18	0.80	0.097	642.53
13AE	R8	32	1.35	0.21	0.88	0.020	62.85
13AE	RC	32	1.49	0.31	0.66	0.017	213.47
17CC	L2	69	1.50	0.30	0.28	0.036	265.59
17CC	LC	69	1.45	0.18	0.39	0.065	205.69
17CC	R2	69	1.54	0.28	0.27	0.016	53.79
17CC	R8	69	1.49	0.30	0.29	0.008	8.91
17CC	RA	69	1.52	0.30	0.27	0.011	21.25
17DA	L2	70	1.53	0.26	0.29	0.003	16.27
17DA	LC	70	1.58	0.30	0.37	0.005	4.70
17DA	R2	70	1.56	0.26	0.29	0.005	16.41
17DA	R8	70	1.57	0.27	0.32	0.004	3.96
17DA	RA	70	1.58	0.22	0.31	0.004	8.17
141E	L2	37	1.55	0.29	0.62	0.015	29.22
141E	LC	37	1.23	0.21	0.86	0.037	13.45
141E	R2	37	1.56	0.28	0.63	0.009	31.08
141E	R8	37	1.48	0.29	0.73	0.004	3.87
141E	RA	37	1.54	0.28	0.67	0.006	9.11
1421	L2	37	1.49	0.28	0.57	0.021	39.59
1421	LC	37	1.39	0.17	0.96	0.019	5.41
1421	R2	37	1.51	0.29	0.55	0.017	30.38
1421	R8	37	1.53	0.26	0.73	0.006	3.36
1421	RA	37	1.53	0.21	0.67	0.009	9.21
1424	L2	37	1.56	0.28	0.59	0.011	26.56
1424	LC	37	1.24	0.17	0.97	0.024	11.04
1424	R2	37	1.56	0.28	0.59	0.008	28.31
1424	R8	37	1.55	0.24	0.77	0.006	4.17
1424	RA	37	1.55	0.29	0.66	0.007	17.78
1427	L2	37	1.50	0.30	0.67	0.015	4827.68
1427	LC	37	1.32	0.36	0.69	0.029	243.85
1427	R2	37	1.52	0.27	0.64	0.013	187.72
1427	R8	37	1.51	0.32	0.76	0.005	14.83
1427	RA	37	1.56	0.28	0.76	0.008	38.20
2007	LC	144	1.26	0.32	0.43	0.015	111.84
2007	R8	144	1.54	0.20	0.40	0.004	74.89
2007	RC	144	1.46	0.27	0.40	0.007	138.61
2095	LC	151	1.62	0.15	0.76	0.005	113.10
2095	R8	151	1.93	0.14	0.64	0.004	105.57
2095	RC	151	1.49	0.23	0.53	0.004	120.75
195B	R8	81	1.45	0.28	0.31	0.005	83.89

Table A5: Returned parameter results for all surveys using gamma distribution from Hansen & Travis (1974)

Survey	Filter	Sol	R_{eff}	v_{eff}	τ	RMS	χ^2_v
13AE	LC	32	1.61	0.33	0.92	0.099	928.05
13AE	R8	32	1.49	0.30	0.87	0.035	221.94
13AE	RC	32	1.51	0.30	0.64	0.046	1131.04
17CC	L2	69	1.50	0.33	0.30	0.074	800.22
17CC	LC	69	1.41	0.34	0.45	0.081	338.14
17CC	R2	69	1.54	0.31	0.30	0.049	314.60
17CC	R8	69	1.54	0.30	0.31	0.035	170.97
17CC	RA	69	1.55	0.30	0.33	0.030	91.97
17DA	L2	70	1.49	0.29	0.34	0.004	17.39
17DA	LC	70	1.50	0.30	0.45	0.005	9.79
17DA	R2	70	1.50	0.30	0.32	0.007	21.37
17DA	R8	70	1.59	0.33	0.34	0.005	6.70
17DA	RA	70	1.50	0.32	0.33	0.009	17.45
141E	L2	37	1.54	0.33	0.76	0.032	81.86
141E	LC	37	1.28	0.39	0.95	0.031	NaN
141E	R2	37	1.59	0.28	0.83	0.026	72.26
141E	R8	37	1.40	0.33	0.92	0.018	29.72
141E	RA	37	1.54	0.30	0.85	0.028	49.35
1421	L2	37	1.56	0.31	0.64	0.026	55.10
1421	LC	37	1.47	0.17	0.96	0.019	5.24
1421	R2	37	1.52	0.31	0.69	0.023	48.41
1421	R8	37	1.69	0.29	0.77	0.009	6.48
1421	RA	37	1.58	0.29	0.70	0.015	18.07
1424	L2	37	1.45	0.37	0.90	0.020	54.15
1424	LC	37	1.44	0.17	1.05	0.028	23.83
1424	R2	37	1.53	0.31	0.86	0.015	36.59
1424	R8	37	1.69	0.28	0.81	0.015	NaN
1424	RA	37	1.46	0.35	0.82	0.019	30.71
1427	L2	37	1.55	0.30	0.67	0.025	289.70
1427	LC	37	1.78	0.48	0.72	0.040	355.74
1427	R2	37	1.55	0.31	0.71	0.009	105.87
1427	R8	37	1.75	0.34	0.82	0.013	34.08
1427	RA	37	1.54	0.36	0.81	0.008	24.12
2007	LC	144	1.61	0.20	0.44	0.010	99.76
2007	R8	144	1.61	0.19	0.40	0.003	76.00
2007	RC	144	1.53	0.27	0.43	0.009	139.85
2095	LC	151	1.56	0.05	0.71	0.005	103.84
2095	R8	151	1.57	0.26	0.62	0.005	95.40
2095	RC	151	1.57	0.28	0.72	0.003	144.01
195B	R8	81	1.46	0.30	0.34	0.025	123.54

Table A6: Returned parameter results for all surveys using bimodal distribution from Hansen & Travis (1974)

Survey	Filter	Sol	R_{eff}	v_{eff}	τ	μ_x	μ_y	σ_x	σ_y	RMSE	χ^2_v
17CC	R8	69	0.00	0.00	0.00	0.00	0.00	0.00	0.00	0.000	0.00
13AE	R8	32	1.50	0.12	0.91	5.63	1.39	1.19	0.55	0.004	0.12
12FE	R8	25	1.96	0.29	0.53	4.43	0.00	0.89	0.73	0.008	0.62
141E	R8	37	1.80	0.38	0.69	9.04	0.22	0.95	0.41	0.005	0.22
1421	R8	37	1.27	0.30	0.58	4.68	0.00	1.21	0.60	0.004	0.13
1424	R8	37	2.06	0.20	0.78	3.77	0.00	1.08	0.78	0.010	1.02
1427	R8	37	1.43	0.12	0.91	6.81	0.00	1.38	0.79	0.004	0.13
153D	R8	48	1.49	0.27	0.43	4.75	0.00	0.65	0.49	0.008	0.61
1710	R8	63	1.93	0.26	0.34	4.40	0.00	0.93	0.77	0.016	15.34
17DA	R8	70	1.22	0.34	0.26	5.11	0.00	1.93	0.56	0.003	0.10
1813	R8	71	2.13	0.15	0.36	4.28	0.02	0.67	0.63	0.031	34.79
185D	R8	73	1.24	0.20	0.32	4.32	0.00	1.61	0.12	0.008	9.02
18CB	R8	77	1.24	0.27	0.24	3.69	0.00	1.42	0.16	0.004	6.61
195B	R8	81	1.96	0.44	0.31	4.61	0.00	0.64	0.53	0.006	0.31
1A92	R8	90	1.19	0.23	0.26	3.49	0.00	1.49	0.22	0.009	7.41
1AE1	R8	93	2.30	0.32	0.33	3.83	0.00	0.82	0.83	0.015	125.85
1C10	R8	104	2.18	0.35	0.32	5.64	0.00	1.09	0.75	0.041	30.43
1C37	R8	105	1.34	0.08	0.40	1.93	0.00	0.61	1.70	0.000	0.07
1CE2	R8	111	2.39	0.35	0.31	4.34	0.00	1.19	0.88	0.013	35.99
1D5F	R8	115	2.19	0.20	0.29	5.53	0.48	0.88	0.61	0.025	33.14
1F1D	R8	133	1.14	0.06	0.33	10.00	0.01	2.75	1.15	0.005	12.27
1FF0	R8	143	1.26	0.06	0.30	5.68	0.07	0.85	0.60	0.000	0.08
2019	R8	145	1.68	0.12	0.33	5.56	0.23	0.90	0.66	0.004	0.15

Table A7: Returned parameter results for all surveys using gamma distribution from Hansen & Travis (1974) and an ellipsoidal phase function model

Sol	$dP_{11}(30°/d\theta$	$P_{11}(120°)$	$R_{eff}[\mu m]$
27.0	-0.062	0.24	1.59
124.0	-0.064	0.23	1.34
140.0	-0.064	0.24	1.37
203.0	-0.073	0.3	1.29
251.0	-0.064	0.21	1.73
333.0	-0.065	0.2	1.76
338.0	-0.058	0.2	1.76
426.0	-0.061	0.21	1.56
490.0	-0.058	0.22	1.73
494.0	-0.059	0.23	1.61
519.0	-0.058	0.24	1.59
543.0	-0.059	0.27	1.42
572.0	-0.06	0.22	1.7
625.0	-0.06	0.22	1.56
627.0	-0.063	0.2	1.61
640.0	-0.061	0.22	1.6
643.0	-0.059	0.25	1.55
650.0	-0.06	0.25	1.41
658.0	-0.068	0.22	1.41
699.0	-0.072	0.2	1.52
752.0	-0.069	0.18	1.66
957.0	-0.063	0.17	1.07
1054.0	-0.066	0.22	1.41
1101.0	-0.058	0.23	1.63
1215.0	-0.063	0.21	1.63

Table A8: Returned phase function diagnostics and particle size for parameterized phase function fit to MERB surveys

Sol	$dP_{11}(30°/d\theta$	$P_{11}(120°)$	$R_{eff}[\mu m]$
27.0	-0.061	0.23	1.54
124.0	-0.065	0.24	1.34
140.0	-0.066	0.25	1.41
203.0	-0.074	0.29	1.65
251.0	-0.066	0.22	2.08
333.0	-0.063	0.2	2.02
338.0	-0.059	0.21	1.75
426.0	-0.062	0.22	1.5
490.0	-0.058	0.23	1.69
494.0	-0.059	0.25	1.53
519.0	-0.059	0.25	1.5
543.0	-0.06	0.28	1.43
572.0	-0.061	0.25	1.72
625.0	-0.059	0.25	1.5
627.0	-0.062	0.2	1.56
640.0	-0.063	0.24	1.59
643.0	-0.059	0.25	1.5
650.0	-0.059	0.24	1.4
658.0	-0.068	0.24	1.42
699.0	-0.072	0.22	1.54
752.0	-0.067	0.2	1.91
957.0	-0.064	0.18	0.75
1054.0	-0.065	0.24	1.43
1101.0	-0.057	0.25	1.71
1215.0	-0.064	0.25	1.64

Table A9: Returned phase function diagnostics and particle size for ellipsoidal phase function fit to MERB surveys

Sol	$dP_{11}(30°/d\theta$	$P_{11}(120°)$	$R_{eff}[\mu m]$
49.0	-0.062	0.22	1.73
118.0	-0.061	0.23	1.21
211.0	-0.072	0.23	1.34
361.0	-0.059	0.27	1.51
422.0	-0.058	0.28	1.28
486.0	-0.058	0.31	1.39
515.0	-0.054	0.35	1.5
519.0	-0.054	0.31	1.5
526.0	-0.056	0.28	1.5
545.0	-0.056	0.34	1.5
565.0	-0.058	0.29	1.5
624.0	-0.058	0.27	1.5
643.0	-0.057	0.28	1.52
650.0	-0.058	0.32	1.41
679.0	-0.057	0.33	1.5
756.0	-0.058	0.26	1.41
863.0	-0.064	0.23	1.48
1090.0	-0.067	0.29	1.28
1152.0	-0.057	0.35	1.34

Table A10: Returned phase function diagnostics and particle size for parameterized phase function fit to MERA surveys

Sol	$dP_{11}(30°/d\theta$	$P_{11}(120°)$	$R_{eff}[\mu m]$
49.0	-0.061	0.23	1.79
118.0	-0.061	0.24	1.17
211.0	-0.072	0.24	1.36
361.0	-0.059	0.28	1.5
422.0	-0.059	0.3	1.26
486.0	-0.057	0.33	1.43
515.0	-0.054	0.27	1.47
519.0	-0.053	0.36	1.47
526.0	-0.057	0.32	1.47
545.0	-0.055	0.38	1.41
565.0	-0.058	0.22	1.5
624.0	-0.06	0.29	1.5
643.0	-0.058	0.28	1.5
650.0	-0.058	0.34	1.5
679.0	-0.057	0.32	1.5
756.0	-0.06	0.28	1.43
863.0	-0.062	0.23	1.47
1090.0	-0.067	0.29	1.35
1152.0	-0.057	0.36	1.34

Table A11: Returned phase function diagnostics and particle size for ellipsoidal phase function fit to MERA surveys